Politecnico di Torino

Master Degree course in Aerospace Engineering
A.Y. 2022/2023
Graduation session July 2023

Impact of mistuning in flutter stability analyses

Supervisors:

Prof. Christian Maria Firrone
Prof. Lorenzo Pinelli
Ing. Antonio Giuseppe D'Ettole

Candidate:

Andrea Moro, 291406

*A tutti i sognatori,
non mollate mai.*

Acknowledgements

Scherzi a parte, mi avete dato tanto, spero di poter fare lo stesso nel futuro e di avervi reso orgogliosi, grazie di cuore.

Uno speciale ringraziamento va a Zia Bora e a mia cugina Anna, che per me hanno fatto tanto in questi anni e mi hanno permesso di crescere, diventando la mia seconda famiglia. Davvero grazie infinite, siete state fantastiche!

E poi ci sei tu, Zio, che con la tua sola presenza rallegravi la giornata. Non dimenticherò mai le afose giornate d'estate in officina, la felicità di quando, a sorpresa, vedevo la macchina parcheggiata nella via di casa e l'euforia di andare in camper con te e Zia. Grazie, grazie e ancora grazie per questi ricordi indelebili. Sono certo che lassù stai facendo ridere tutti con il tuo infinito repertorio di barzellette!

In questi anni al Politecnico ho conosciuto tante persone, alcune passeggere, altre che invece mi rimarranno per sempre nel cuore. Grazie mille ragazzi, grazie Federico, Mirko, Luca, Giuseppe, Simone, Francesco, Viviana, Anthony, Matteo, Stefan, Marco e Alessandro per questi anni indimenticabili dove mi avete aiutato a superare gli ostacoli e darmi forza nei momenti più bui e a festeggiare e gioire insieme nei traguardi di questo percorso. Ne abbiamo passate tante, ma alla fine stiamo vedendo la luce in fondo al tunnel. In questi anni siete stati il mio punto di riferimento a Torino e spero possiate continuare ad esserlo nel futuro.

Un grazie di cuore va poi a Squadra Corse, un'esperienza bellissima, estremamente provante, ma che mi ha regalato tante soddisfazioni e che mi ha permesso di conscere persone fantastiche e di coltivare la mia passione. Un ringraziamento speciale va a Dario e Matteo, i miei fratelli in Squadra, gli aeroboys. Grazie perchè senza di voi chi mai li avrebbe fatti Patagaserru, Fisininnu, Parracasanna..Fraaanco e Parrignallala. Ho perso il conto delle volte in cui siamo rimasti sino a notte fonda a progettare e capire che cosa fare, arrovellandoci sui mille problemi, eppure per me è stato puro divertimento, specialmente con voi al mio fianco. E mi raccomando, guai a voi se vi dimenticate i numeri in sardo che poi dobbiamo giocare a morra! Specialmente le varianti, che ormai si sa, cambiano in base all'umidità. Dopotutto il sardo è una lingua, non è un dialetto! Grazie di cuore ragazzi, vi auguro il meglio.

Ultimi, ma non per importanza, ci sono loro, i famosi "amici di giù",

Kekko, Mattia, Christian, Jones e Andrea. Vi ringrazio per avermi regalato tanti momenti speciali e indimenticabili, per avermi aspettato la mattina sotto casa per andare al mare una miriade di volte, avermi sopportato quando parlavo di università per non parlare di Zio Mike e Zio Chuck!
In tutto questo, una cosa è certa, quando si arriva al bar: "Ascò, Mirto!...".

Ringrazio tutti voi, che mi avete accompagnato durante questo percorso che ormai, nel bene e nel male, è giunto al termine. Senza tutti voi non ci sarei riuscito e ognuno di voi avrà un posto speciale nel mio cuore. Da ora, si apre un nuovo capitolo della mia vita e spero che ognuno di voi continuerà ad esserci.

Abstract

Today, more than ever, the aerospace industry is moving towards reducing its environmental impact and improve the sustainability. For this reasons, a great emphasis is placed on producing lighter and more efficient engines and those objectives are reflected on it's components among which we can find the Low Pressure Turbines (LPT). In fact, the development path, moved towards lighter and higher aspect ratios leading to blades more susceptible to vibrations.
For this reasons the flutter, which is a vibration phenomenon, has increased its importance in aircraft jet engines since its first documented case reported in compressor blade in 1945.

One of the most important features of flutter relates to its nature: a self-excited and self sustained phenomenon leading, based on the condition, to limit-cycle oscillations which consequently lowers the blade life due to high cycle fatigue, or even worse, an abrupt failure in few cycles since, as mentioned before, is self sustained, hence it increases its amplitude constantly due to the energy fed into the blade from the surrounding air.

This thesis work, developed in collaboration with Avio Aero, has the aim to analyze the flutter stability of the bladed disk used in the European project ARiAS, by means of a 3D flutter solver and is the continuation of a previous thesis work by S. Raimondo [18].
In particular, the tests carried out in this work evaluates the mistuning effect, for a total of four configurations, two tuned and two mistuned respectively, with different 3D flutter solver methodologies, three rotational speeds and two mode shapes.

Contents

List of Figures

List of Tables

Chapter 1

Introduction

1.1   The aircraft gas turbine engine

The gas turbine for aircraft has its roots long time ago, around 1930, when the first patent regarding this engine was filed by Frank Whittle in 1930 after the RAF did not found interesting the idea. This did not stop his idea, which after seven years from the original patent, a working prototype runs in UK and Germany, but it was not used effectively in an aircraft until August 1939 by Germany, which used this engine in an experimental aricraft, the Heinkel He 178 [9].

However, the first mass production aircraft has been done, again, by the Germans during World War II in 1944 with the development of the Junkers Jumo 004 equipped in the Messerschmitt Me 262.

Since then, a long path has been done, made of failures and successes, until the modern jet engines, which have to face a new development phase to meet the new emission requirements in order to reach carbon neutrality by 2050.

Working Principle   The gas turbine engine working principle is based on Newton's third law of motion which states that '*for every force acting on a body there is an opposite and equal reaction*'.

From this base, we can understand that the aircraft gas turbine produces thrust ingesting air from its air intake at the front and accelerates it by performing a thermodynamic cycle, specifically the Joule-Brighton cycle.

Before analyzing the cycle itself, an explanation of its main components is obliged. As can be seen in figure 1.1, the main components which can be found inside a gas turbine engine are the following:

- **Air intake**: it serves to lower the speed of air which then goes to the compressor. By using this device, we can also start to perform a first compression not only inside the intake but also outside by means of a ram compression, which is isentropic, hence without losses;

- **Compressor**: composed by a different number of blade rows. Each row is composed by a disk with a number of blades attached to it (either connected, forming a bladed-disk, or manufactured in a single piece, creating the so called blisk) and its main objective is to compress the fluid and increase its temperature. All of that, trying to keep constant the flow axial velocity. The various rows are composed by an alternation of rotating and stationary disks. Different stages can compose the compressor and each stage contains various rows couples. To be noted that the compressor section increases along the engine axis;

- **Combustion chamber** (and combustors): fuel is injected at this stage, increasing the temperatures to more than 2000 K;

- **Turbine**: the turbine is a device used to extract energy from the hot and highly pressurized air. The energy is extracted via an alternation of static (vanes) and rotating disks, and is necessary to move the compressor (which is connected to the turbine through the engine shaft) and provide enough power for the utilities connected through the gearbox. Note that not all of the fluid energy is extracted, since there must be enough in order to accelerate the fluid in order to produce thrust;

- **Nozzle**: this device, placed at the end of the engine, accelerates the fluid, maximizing the engine thrust;
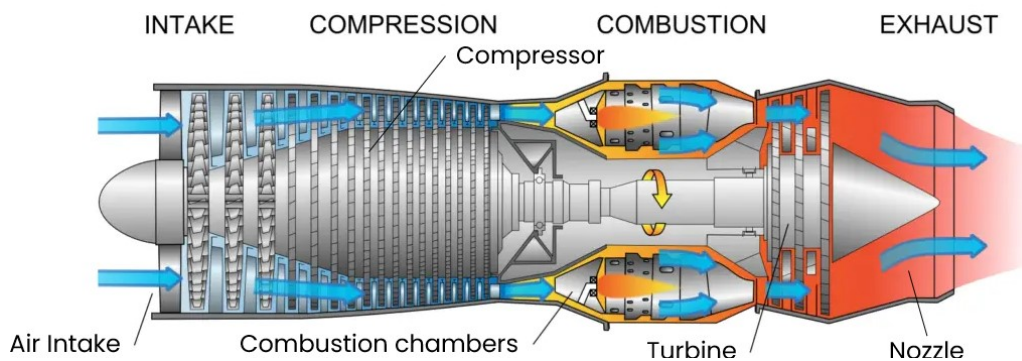
Figure 1.1: Example of the main components inside a gas turbine engine.[5]

Joule-Brighton cycle   As mentioned before, the Joule-Brighton cycle is the one used in the gas turbine engines. The engine, uses air as working fluid and to provide thrust it must increase the kinetic energy and to do that, as hinted in the description of the components above, it must first compress the air, so that the pressure is increased (as well as the temperature), then we increase the heat energy by burning the fuel in the combustion chamber, and finally, the build-up energy is converted in kinetic energy and the flux is ejected from the engine nozzle with high velocity [14]. The same passages can be found in the Joule-Brighton cycle, represented in figure 1.2 in its ideal form, hence without losses, in a typical T-S diagram[1]:

- 0= far field conditions;

- 0-1=Isentropic compression thank to the the engine inlet;

- 1-2=Isentropic compression (done inside the compressor);

- 2-3=Combustion;

- 3-4=Isentorpic expansion in the turbine;

- 4-5=Isentropic expansion in the nozzle;

and the engine efficiency can be calculated, for the ideal case, with the formula:

---

[1]T=temperature, S=entropy
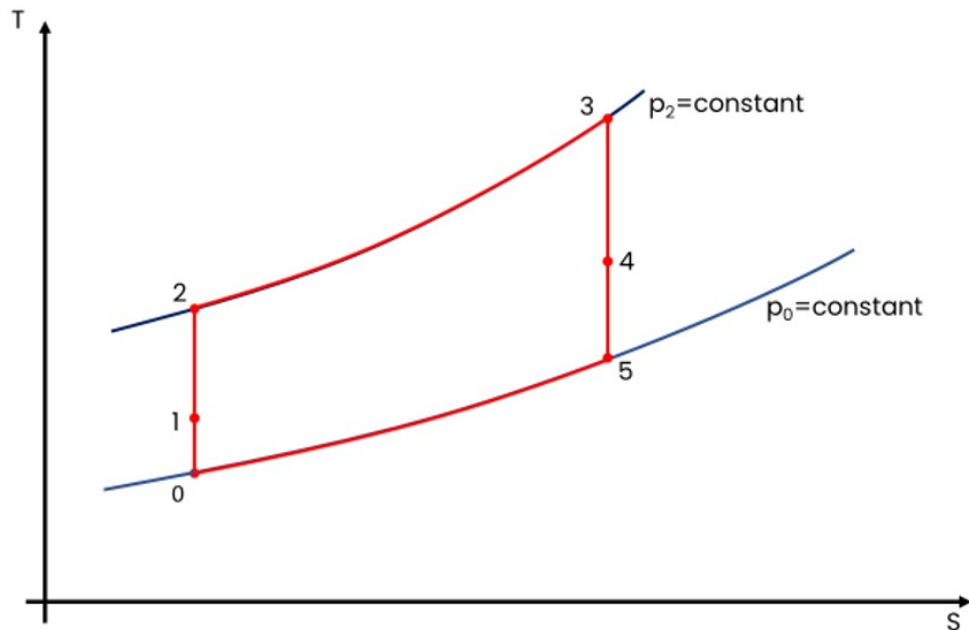
Figure 1.2: Schematic representation of the ideal Joule–Brayton cycle.

$$\eta_{ideal} = 1 - \frac{T_3}{T_2} = 1 - \frac{1}{\beta^{\frac{\gamma-1}{\gamma}}} \tag{1.1}$$

where γ is the heat capacity ratio and $\beta = p_2/p_1$ is the compression rate. The cycle in reality has a different shape. In fact, as can be seen in figure 1.3, the shape changes and for a good reason: taking into account losses will cause an increase in entropy. Analyzing each section:

- 0= far field conditions;

- 0-1= compression due to engine intake: we can actually divide this part into two sections, one before the engine intake and one at the end of the engine intake. In fact, the air from the far field, due to the presence of the air intake, goes through an isentropic compression. Meanwhile, once we enter the air intake, we face some losses. Those two pieces are here merged together in a unique line;

- 1-2= inside the compressor, the air increases its pressure and temperature up to p_2 and T_2 respectively.
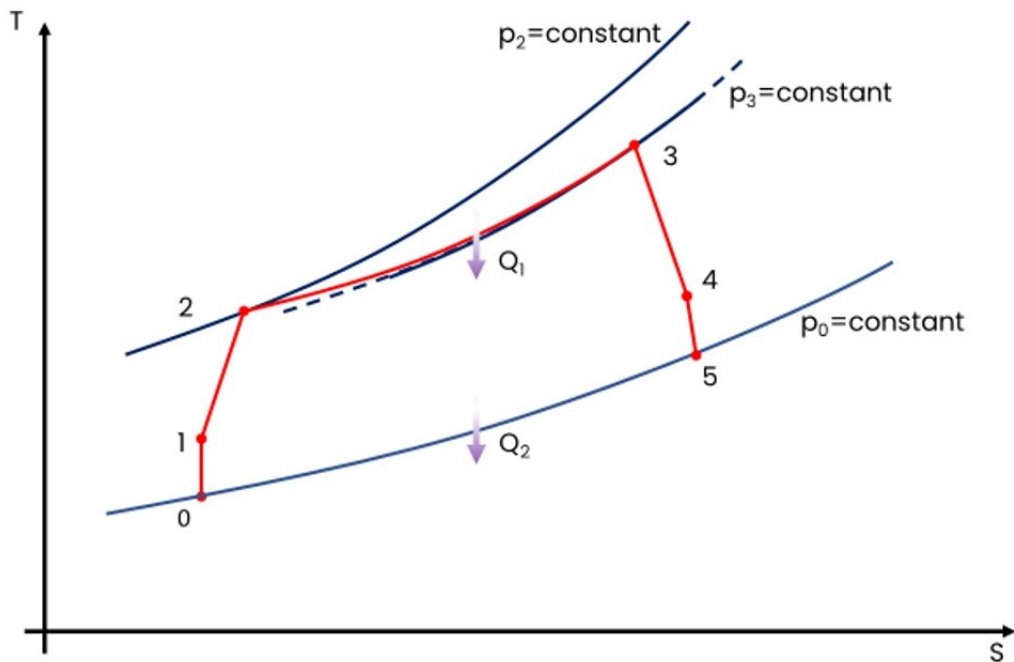
Figure 1.3: Schematic representation of the real Joule-Brayton cycle.

- 2-3= combustion. In this case, instead of an isobaric combustion, there is a lower pressure at the end of the combustion, combined with a greater entropy, hence greater losses. In this part, energy Q_1 is fed into the system;

- 3-4= expansion in the turbine stages;

- 4-5= expansion in the nozzle;

The cycle, is defined an open-cycle, since it gathers fresh air from the ambient and releases it again in the ambient at point 5. So the cycle must start at ambient pressure and end at ambient pressure. The consequences of this are big, because since we have to end at the same static pressure, this means that greater losses cause a lower expansion ratio in the turbine-nozzle section (from 3 to 5).

Since the turbine must extract a specific amount of energy (which is going to be used by the compressor and the utilities), the remaining part is going to be used to provide thrust, hence, greater pressure losses mean that the differential between the end com-

High T$_3$ Low T$_3$
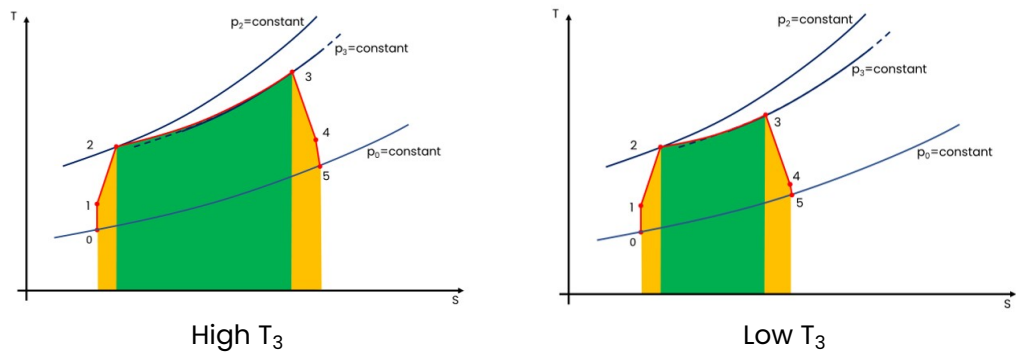
Figure 1.4: Graphical representation of the effect of the end combustion temperature on the cycle efficiency. In green, the energy fed into the system, in yellow, the losses.

bustion and the nozzle exit is going to be smaller.

The energy wasted in the cycle is represented by Q_2. Given that, we can define the efficiency as:

$$\eta_{real} = \frac{Q_1 - Q_2}{Q_1}$$

where the work done by the cycle is $L = Q_1 - Q_2$. Lowering the losses, or on the other side, lowering the relative importance of the losses over the energy fed into the cycle, increases the efficiency (with a constant β). We can clearly see this by analyzing the effect of the T$_3$=end combustion temperature over the efficiency η_{real} in figure 1.4: higher T$_3$ mean that more energy is provided, so Q_1 is higher hence the relative importance of Q_2 is lower in the efficiency equation, so the efficiency increases (up to the ideal value) [10] [11].

1.1.1   Turbojet

The Turbojet engine is the first engine to be made, and is the same shown in previous page, like the one in figure 1.1. Nowadays, in commercial aircraft is in disuse and has been replaced by tur-bofan engines due to the higher efficiencies of the latter despite having an higher thrust, especially at high Mach numbers. The working principle of the engine is the same as explained before
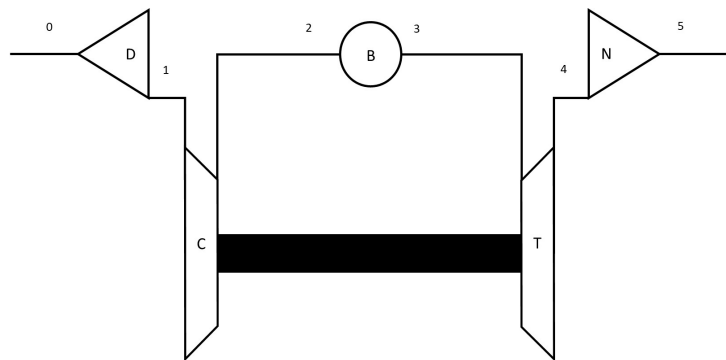
Figure 1.5: Scheme of a typical turbojet engine.
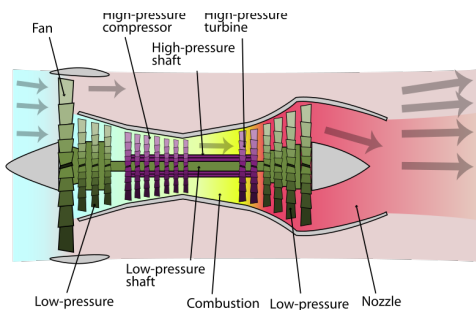
Figure 1.6: Turbofan engine section [2].
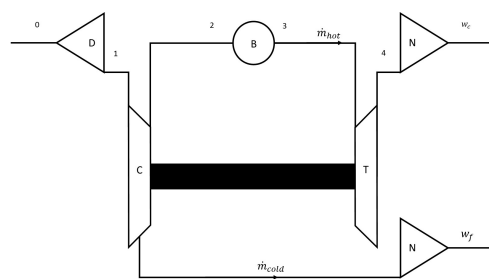
Figure 1.7: Turbofan engine schematic.

and in figure 1.5 we can see a schematic representation of the engine components.

1.1.2 Turbofan

Is an evolution of the turbojet engine. It differs from it mainly by the introduction of a fan at the end of the inlet and by a splitting of the flow: in fact, as can be seen in figure 1.6 and in figure 1.7, the flow is divided in two parts:

- $\dot{m}_{cold}$: cold flow, is the part of the air which does not go to the compressor;

- $\dot{m}_{hot}$: hot flow, gets ingested inside the compressor, hence goes through the thermodynamic cycle typical of a turbojet.

The ratio between those two mass flows is called *By-Pass Ratio*:

$$BPR = \frac{\dot{m}_{cold}}{\dot{m}_{hot}}$$

The advantage of this solution is a decrease in the specific fuel consumption and an increase in the specific thrust with an increasing BPR (up to certain levels).[11]

Moreover, we can find two types of turbofan:

- Mixed flow turbofan: characterized by a low BPR and typically used for supersonic flight, thanks to their lower frontal dimension at the same thrust;

- Unmixed flow turbofan: high by-pass ratio and typically used in subsonic flight due to their lower consumption.

1.1.3 Turboprop

The turboprop engine (figure 1.8) is similar to a turbofan engine but the energy extracted from the hot flow is given to a propeller instead of the fan. In this architecture majority of the thrust is produced by the propeller itself, and the remaining (but small) part is produced by the high-speed exhausts. Moreover, the By-Pass Ratio of this kind of engine is higher than in a typical turbofan engine thanks to the propeller and usually the BPR>50.[19]
The typical configuration is reported in figure 1.9 a free-turbine turboprop, where the power is only given to the propeller. Alternatively, part of the power could be transmitted to a compressor.
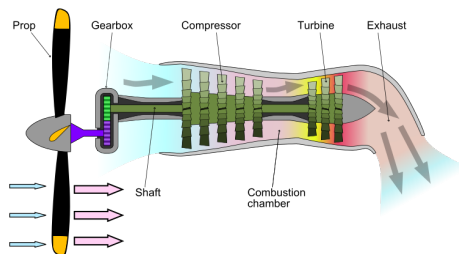
Figure 1.8: Turboprop engine section [20].
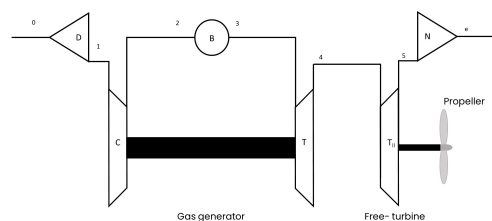
Figure 1.9: Turboprop engine schematic.

The main advantage of the turboprop engine is represented by the lower specific fuel consumption but at the same time, it starts to have problems for M>0,5 so it is suggested for low Mach speeds.

1.2   Low Pressure Turbines

As mentioned before, the turbine is responsible for extracting the power to move the compressor and the utilities (or the propeller based on the configuration). Based on the compression ratio we can have more shafts in order to maximize the compressor and the turbine efficiency.

In fact, we can usually find two turbines: **High-Pressure Turbine** (HPT) and the **Low-Pressure Turbine** (LPT). This division is necessary in order to maximize the efficiency of every turbine: in this case, the LPT is designed in order to work at its best for low pressure ratios, minimizing the number of *stages* for each turbine.

For this reason, to avoid a too rapid pressure drop, the turbines are designed with a divergent geometry, so their span length increases along the engine axis in order to keep a near constant axial velocity and limit the pressure drop. On the other hand, this poses aeroelastic problems with relatively high aspect ratio blade, especially in LPT, and the industry tendency is to further increase this value to improve the turbine (and engine) efficiency.

Moreover, one important thing to be noted about LPT is that its efficiency is greater compared to the compressor stage for one specific reason: the turbine operates in a negative pressure gradient along engine axis (hence pressure lowers), and this gives the possibility to design blades with more aggressive geometries since the boundary layer is less prone to separation, thus making possible to extract more energy.

On the other side, the turbines face much higher temperatures due to the fact they are placed downstream the burner, placing a great challenge for the designers: as we saw before, higher combustion temperatures are crucial since mean higher efficiency but this is limited from materials and cooling capabilities of the blades.

Since the present thesis work focuses on LPTs, from now on the focus will be on this piece of equipment. Regarding the components of a LPT we can divide it in stages, as mentioned before and as displayed in figure 1.10. Every stage, as can be seen in figure 1.11, is divided in a stationary and a rotating part, respectively the
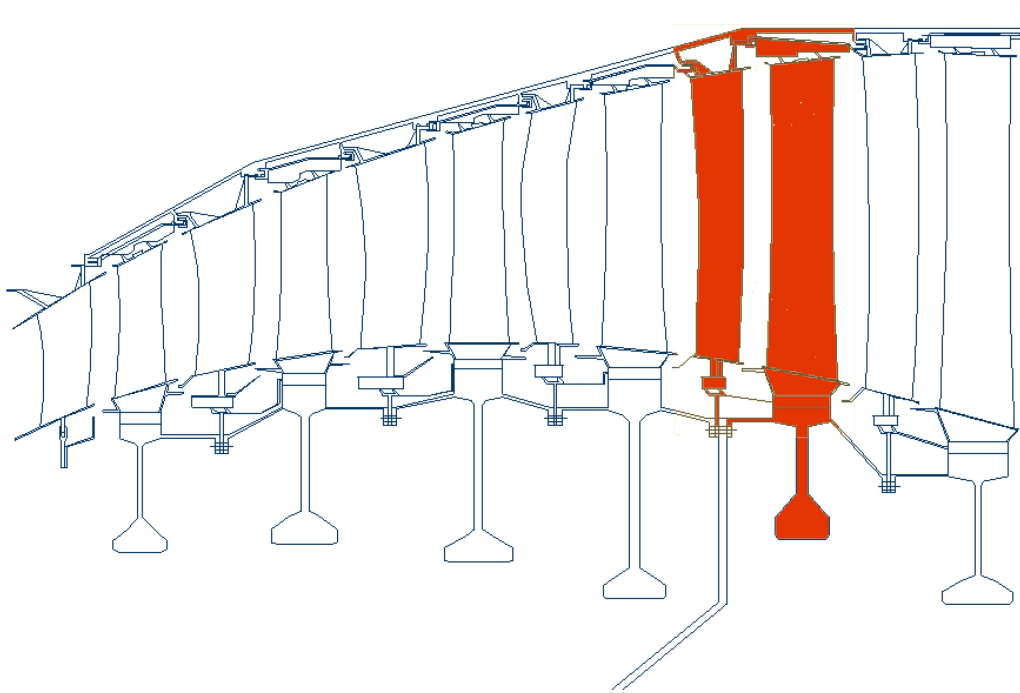
Figure 1.10: Example of a six stage turbine. In red, highlighted a single stage composed by a nozzle and a rotor.[8]

nozzle and the *rotor*:

- **Nozzle**: the static part of the turbine. It's objective is to accelerate the flow, giving an increased tangential velocity, thus deviating the velocity direction and preparing for the rotor downstream;

- **Rotor**: the moving part of the turbine. It is typically composed by the blade, connected to the rotating disk. The former is the connected to the main shaft. This configuration is typically called *balded-disk*. As mentioned before, there is the need to keep ideally a constant velocity along the axis: to do that, since the blade rotates, a twist from root to tip is needed in order to obtain a proper angle of attack of the blade

11
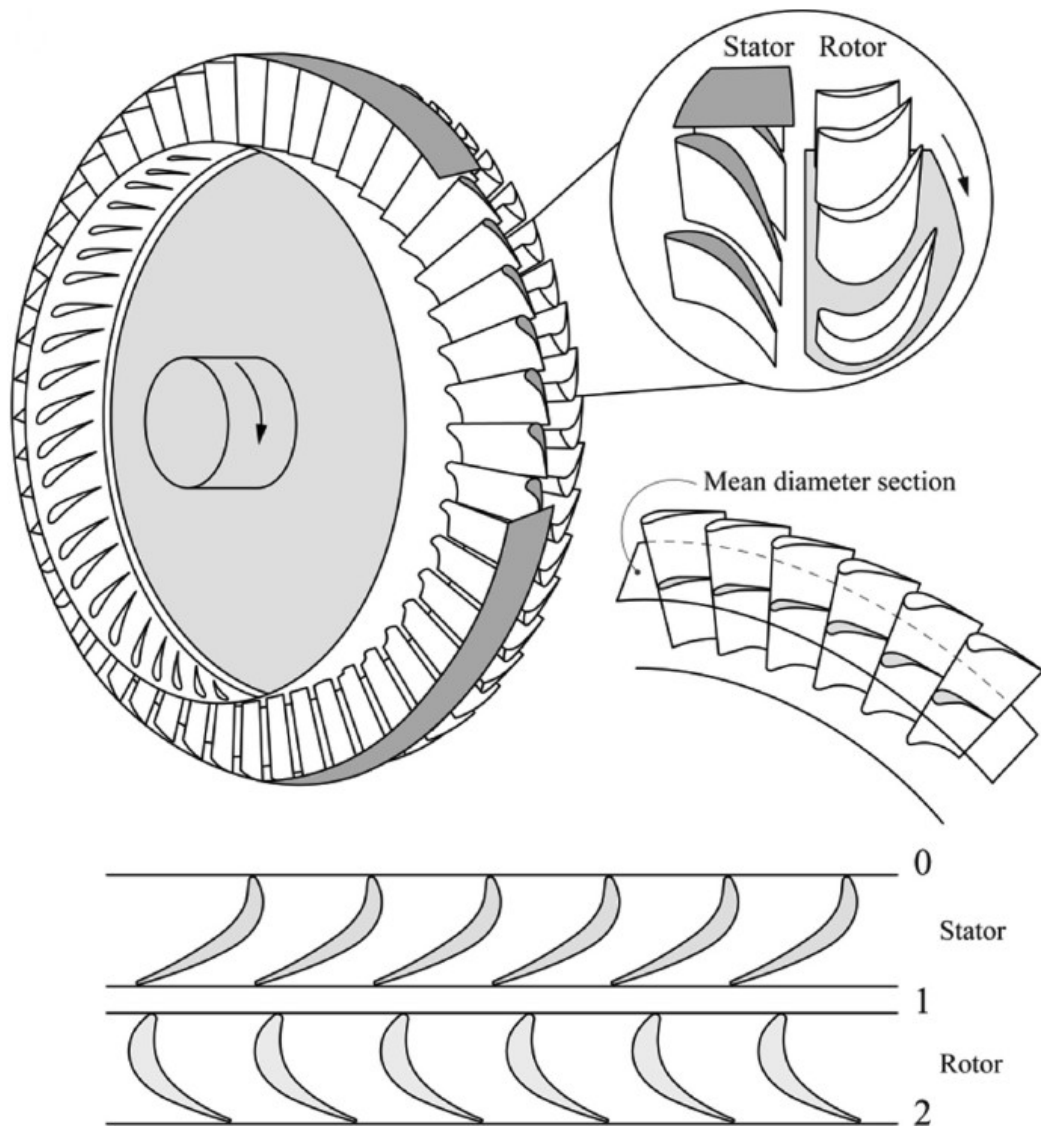
Figure 1.11: Example of a six stage turbine. In red, highlighted a single stage composed by a nozzle and a rotor.[7]

In the present thesis work, the piece analyzed is representative of a rotor blade–disk. We can also divide the rotor blade itself in different portions (from hub to tip):

1. **Shank**: is lowest part of the blade and connects the blade to the disk. It can have different geometries, like a *dovetail* or *fir tree* roots geometry (figure 1.12). This part is of crucial importance since it is a critical part for safety reasons and part of the vibrations can be dissipated here;

2. **Airfoil**: the airfoil is the part of the blade with the actual airfoil geometry, responsible for extracting energy from the fluid.

3. **Shroud**: The tip of the blade. It is used both for limiting the gas leakages at the tip (crucial for improving the efficiency) and improve the aerodynamic efficiency, limiting the tip vortices. Moreover, it has a crucial role in damping the blade vibrations.
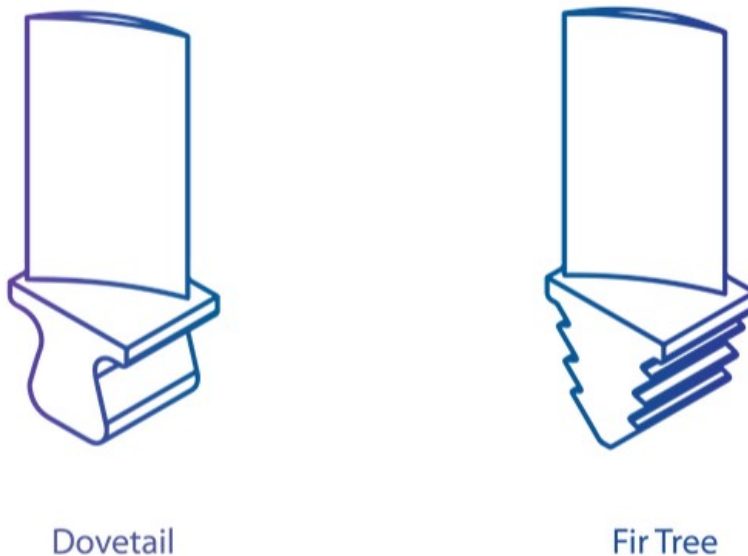
Dovetail   Fir Tree

Figure 1.12: Example of fir tree and dovetail blade roots.[6]

1.3 The ARiAS project

The ARiAS project has been founded by the European Union and is basically an experimental campaign. The project itself is divided in different work-packages (WP):

WP1: Advanced understanding and quantification of compressor forced response and flutter;

WP2: Understanding, non-linear aero-elastic interactions in turbine bladed-discs;

WP3: Understanding, Predicting and Controlling Flutter in Labyrinth Seals;

WP4: Future Enabling Technologies;

WP5: Dissemination, exploitation, communication and e-learning.

The present thesis is a well placed inside the WP2 and WP4, since it deals with some of the experimental results carried inside the WP2 but the results are obtained through the software used in WP4 and help to predict the flutter stability.

Moreover, the ARiAS project is the natural continuation of the FUTURE project: the objectives are clearly different, but some similarities are present. First of all, the blades number and geometry is the same in order to be able to use again the same facilities and the same pieces used in the FUTURE campaign. In this way, some money could be saved and reused for the experiments itself. For this reason, the blade number is fixed to 144 blades.

Regarding the mistuning masses, in the ARiAS project it has been reduced. The reason is to trigger flutter instability: in the FUTURE project the objective was to completely remove the flutter, meanwhile in the ARiAS project, the objective is to reduce the flutter oscillations but to make them visible.

Objectives The ARiAS project objectives are various but in general, the aim of the project is to improve the design methods to predict aeromechanics vibrations. Regarding the WP2, which has seen as major player both Avio Aero and CTA, we have the following objectives:

1. Understand the non-linear interaction between flutter and forced response;

2. Impact of intentional mistuning on flutter and forced response;

3. Impact of under-platform dampers;

4. Enhance and validate numerical methods to increase the reliability of simulations to ease the exploration of new design spaces and reduce development costs;

To do that, two test campaign have been carried out by Avio Aero and CTA:

- CTA's test campaign: a test campaign done in Bilbao at CTA's facilities. The tests consisted in the usage of a cold flow LPTs rig;

- Avio Aero test campaign: test campaign in a in-vacuum test rig, carried out at Sangone facilities and with the aim to measure the damping characteristics without the influence of the aerodynamics;

The experiments are used to investigate existing unconfirmed hypotheses, and to build a stable database for the validation of future numerical methods.

In the present thesis, the test of interest are the one's done at CTA's, since Avio Aero's tests have been done in vacuum conditions. With that said, its important to note that the same type of tests have been done in terms of configuration.

Components and configurations As said before, different configurations have been tested. Overall, the blade has been designed to be representative of a modern LPT turbine, hence with:

- Low thickness;

- Relatively high aspect ration (around 5);

The blade has some peculiar characteristics and they also differ base on the configuration chosen to be tested. In general we can find (based on the test):

- **Blades number**= the blade number has been fixed to 144. It is the same for every configuration. In figure 1.13 an example
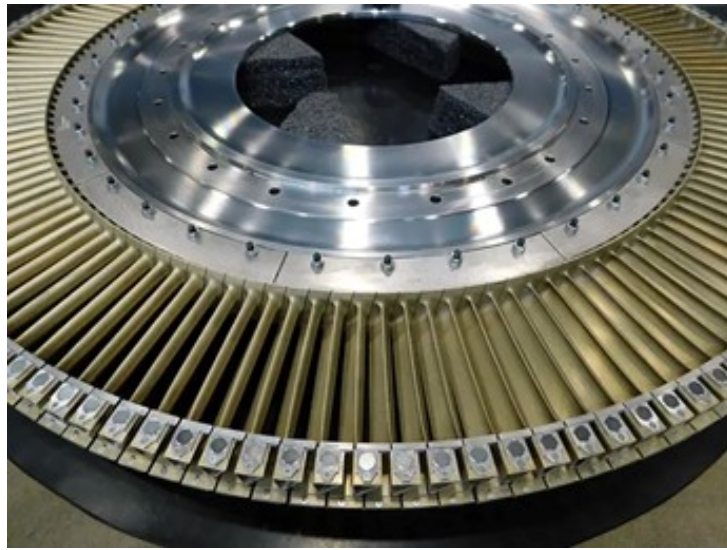
Figure 1.13: Example of the blades mounted on the disk.[16]
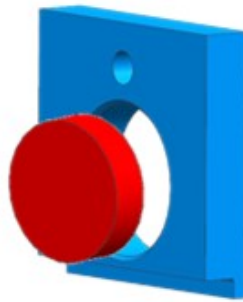
Figure 1.14: Example of the rear magnet cad.[16]

of the blades mounted on the disk;

- **Rear magnet**= the rear magnet, which can be seen in figure 1.14, is a permanent magnet placed in the tip shroud, at the trailing edge. It's objective is to react with a series of fixed permanent magnet in the test rig (see figure 1.15) making possible to recreate a periodical forced response, with different Engine Order (EO, more about that in next chapter) based on the number of permanent magnets placed. The engine orders which could be exited are EO4 and EO6, both separately or simultaneously. The magnets were placed so that a repulsive force was applied and the intensity could be changed based on the distance between the magnets;
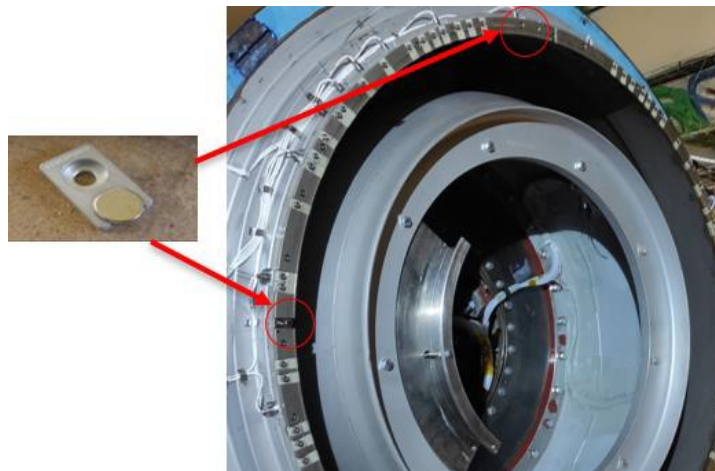
Figure 1.15: Stationary magnets placed in the holder in order to excite the blade at engine order 4 or 6, both separately or simultaneously.[17]
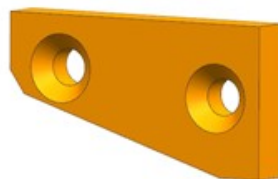
Figure 1.16: Example of the balancing mass cad.[16]
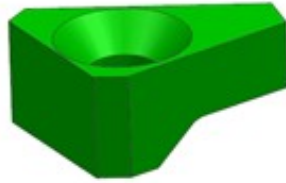
Figure 1.17: Example of the mistuning mass cad.[16]
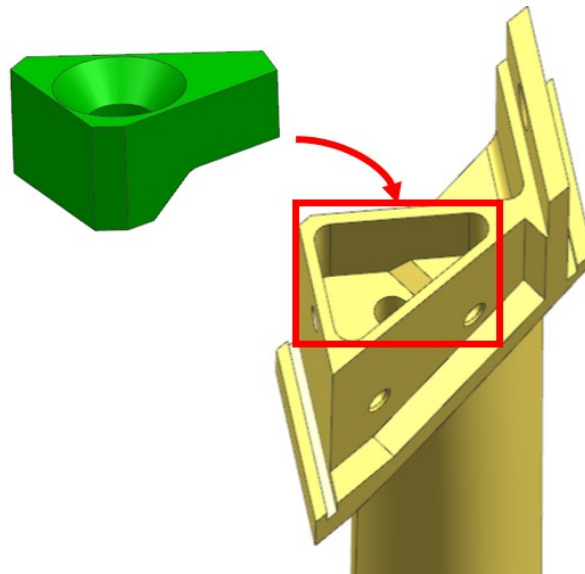
Figure 1.18: In the image above, the mistuning mass and, in red, highlighted the slot dedicated to it on the blade tip shroud.[16]

- **Balancing mass**: the balancing mass (figure 1.16), is placed on the blade to counterbalance the aerodynamic forces which are not present in the Avio Aero tests, making possible to compare the results.

- **Mistuning mass**: the mistuning mass (figure 1.17) is placed in a slot at the tip shroud (figure 1.18) and which makes possible to change the blades resonant frequency, thus uncoupling the resonance between two (or more) blades. In that way, when one blade is prone to vibrating the other is not and will damp the vibration of the former. Regarding the mistuning, different mistuning patterns could be tested: alternate mistuning 10, mistuning 1000, tuned etc. More on the tested configurations later;

18
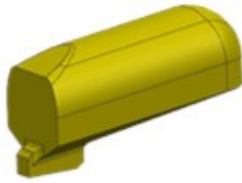
Figure 1.19: Example of the under platform damper cad.[16]
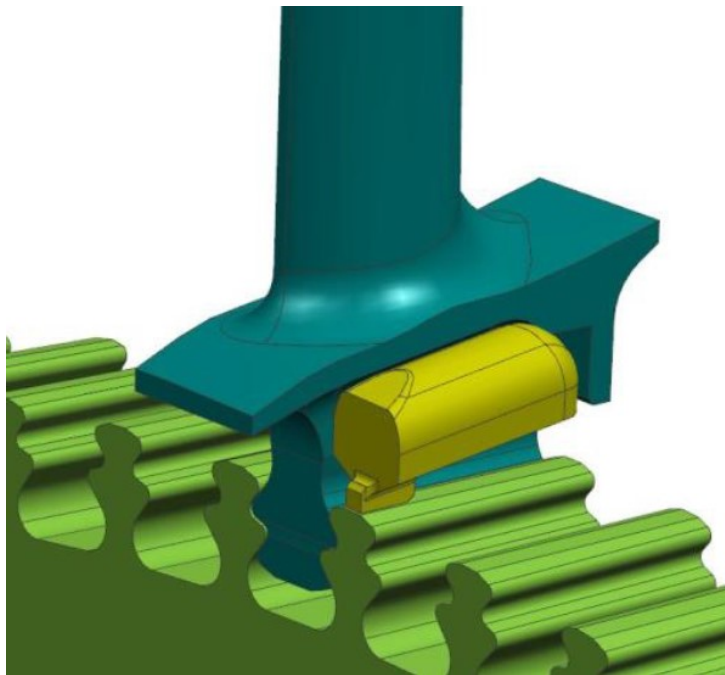
Figure 1.20: In the image above, the underplatform damper positioned under the shank slot.[17]

- **Under platform damper**: the under platform damper (figure 1.19) is used, as the name suggested, to dampen the blade vibration and is placed in a slot in the shank, between the blades as can be seen in figure 1.20. Two materials have been tested in Avio Aero test campaign, one in Aluminium and one in Steel with the latter being more effective. In the CTA experiments, only the Steel damper has been used.

In figure 1.21 can be found an example of the real components. In figure 1.22 the components mounted on the blade.
In the case of the CTA, the tests have been performed in a cold flow facility but it did not have an upstream or downstream disturb in order to excite the blade in terms of forced response (like a vane row).
In order to do that, it was needed to mount on the blade a permanent magnet (placed in the shroud trailing edge) which reacts with a series of fixed magnets mounted on the rig as can be seen in figure 1.23.

Cold flow testing in CTA's LPT rig   In the testing campaign in cold flow rig different tests have been done, with more than 600 experimental points [1]. The test matrix includes:

- Different density values, mainly for scaling the aerodynamic forces (this value remained fixed in the present thesis);

- Different Mach numbers (this value remained fixed in the present thesis);

- Different rotational speeds;

- Different mistuning patterns;

- Tests with and without under platform dampers;

- Two types of execution:

  1. Acceleration and deceleration;

  2. Constant rotational speed;

In-vacuum testing in Avio Aero's spin rig   The main objective of the tests performed in the Avio Aero's spin-rig aims to address the damping characteristics of the model. Configuration with and
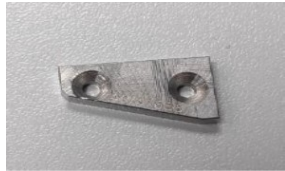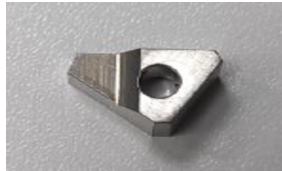
Balancing mass   Mistuning mass   Under   platform
damper

Rear magnet   Blade

Figure 1.21: Example of the real components used in the experiments.[16]
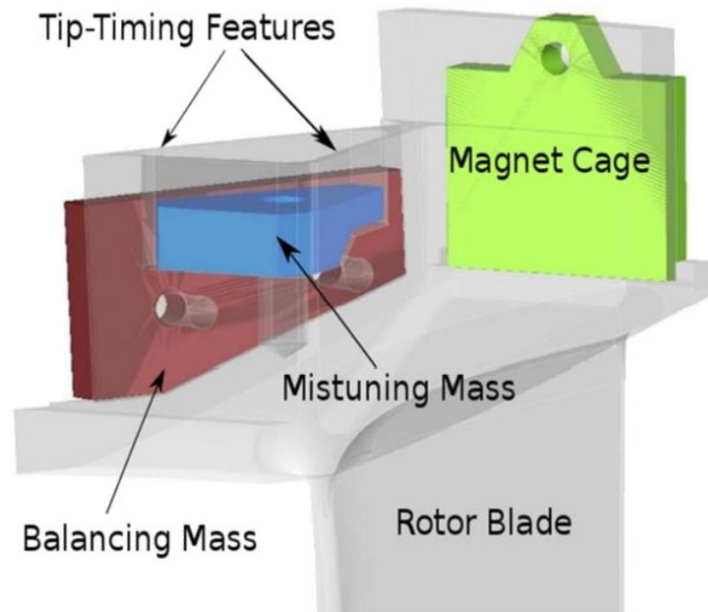
Figure 1.22: CAD example of the CTA's test components mounted.[17]

without the under-platform dampers have been tested, and the mechanical damping has been derived from the measured amplitude response function.

The test matrix has been set to consider several combinations to investigate:

- Tuned and mistuned configurations: two mistuned configurations had been tested, with a mistuning pattern 10 and 1000 (see figure 1.24);

- The blade bending and torsional modes have been excited using permanent magnets;

- Synchronous and asynchronous excitation sourcing: the excitation could come from two magnet carriers, one stationary, with 4 or 6 magnets, thus recreating engine orders 4 or 6 synchronous with the test article operative speed. Moreover, a rotating magnet carrier with 24 magnets has been used to recreate an engine order 24. Playing with the relative counterrotating rotating speed of the test article and the magnet carrier, has been possible to recreate an asynchronous excitation (see figure 1.25);
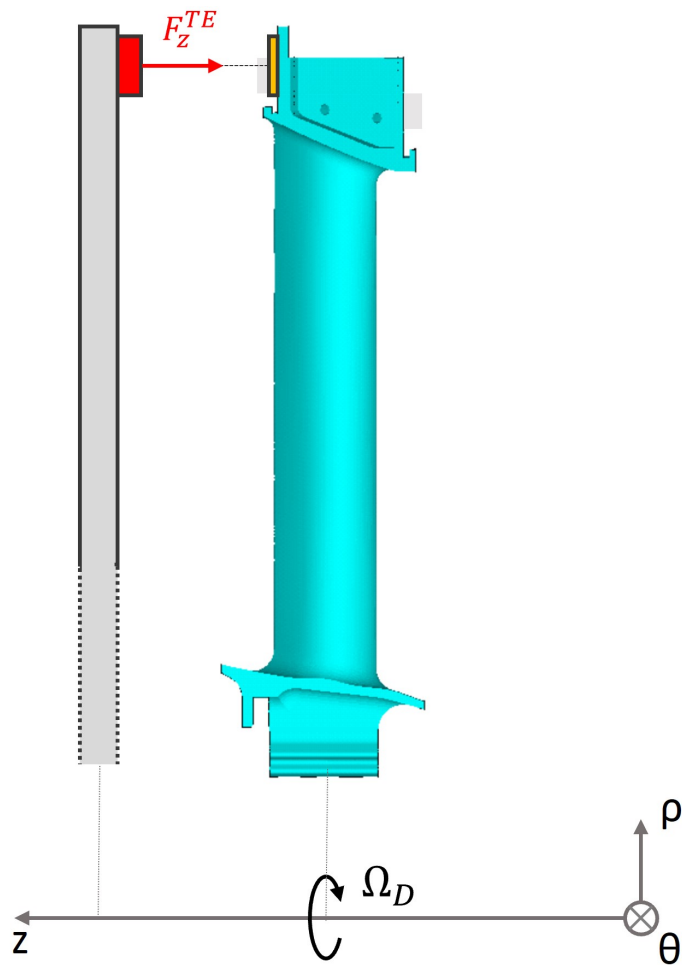
Figure 1.23: Working principle of the rear magnets: Ω_D=disk rotational velocity.
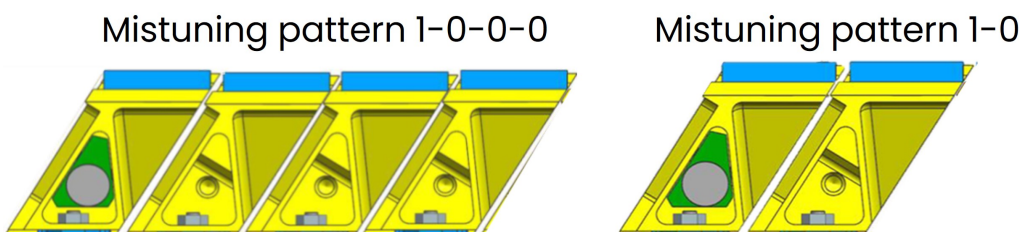
Figure 1.24: Mistuning patterns used in Avio Aero's spin rig
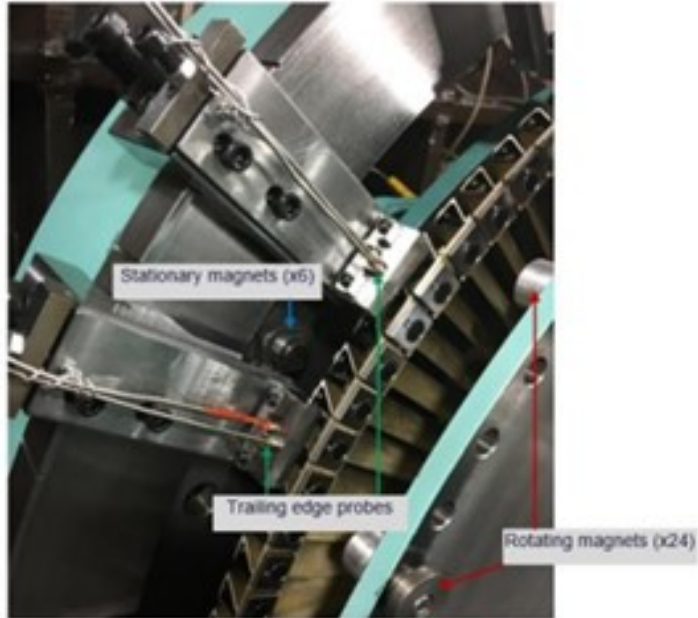
Figure 1.25: Rotating and stationary magnet carriers with the position of the trailing edge tip timing probes.[16]
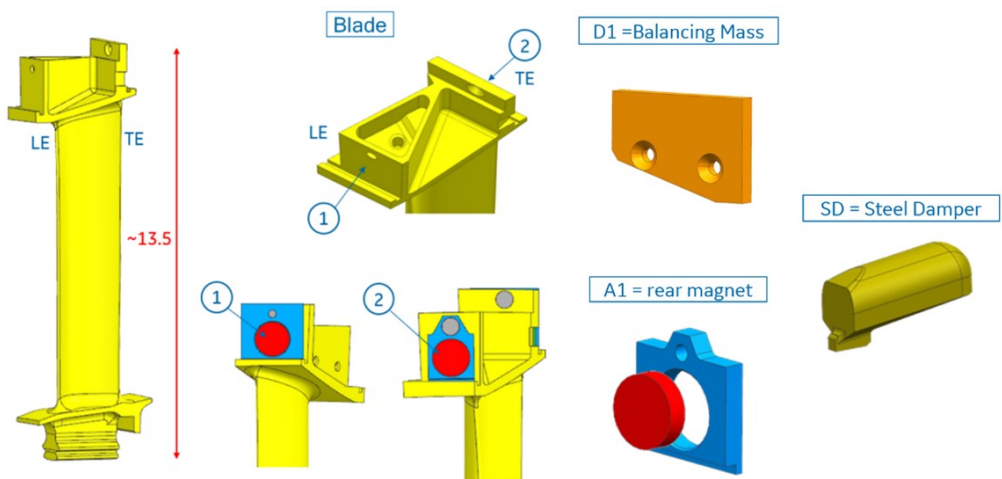
Figure 1.26: In-vacuum test article main features.[16]
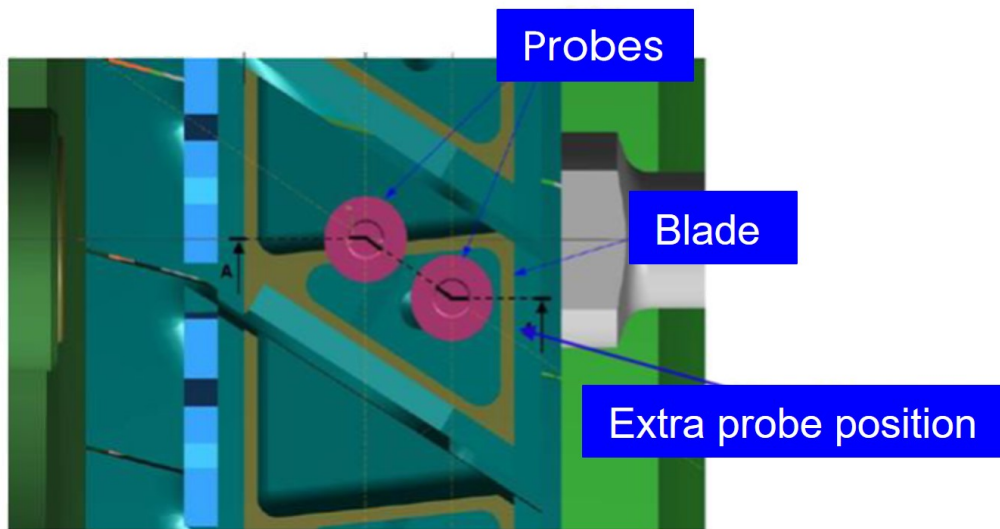
Figure 1.27: Blade Tip Timing probes position.[17]

For a given configuration, the test has been performed at different speed levels. The before mentioned tests had been carried at Avio Aero Sangone Experimental test center, in an in-vacuum test rig. The main features of the test article are reported in figure 1.26

- Blade: designed to be flutter instable. Same blades have been tested in the cold flow in CTA for aeromechanic experiments;

- Front and rear magnets: the two magnets are needed to excite the test article itself. The magnets are attached to the blades by using a magnet holder and a screw;

- Mistuning mass: the mistuning mass is places in the slot on the top of the blade. Its mass is equal to 2.7 grams;

- Under platform dampers: they were used to increase the mechanical damping. The effect of the material density has been explored having two different sets of dampers, one in aluminum, and one in steel;

The vibrations are analyzed by Blade Tip Timing probes (BTT) provided by Rolls-Royce (together with the software). A total of 16 probes have been installed, 8 at the leading edge and 8 at the trailing edge (see figure 1.27)

25

In order to evaluate the damping characteristics, a form of sorting was needed in order to identify the peak response. Once this had been done, the damping evaluation method used is the single DOF resonance peak fitting, extracting the Q-factor with simple Half Power methodology. So, based on that tests some studies have been performed in collaboration with the AerMec team from Politecnico di Torino with the aim to develop a nonlinear method to predict the FR of a Mistuned configuration, using some ROM strategies.

PoliTo spin rig   Not all the post-processed data with BTT on the 144-blade disk can be used for the validation of the developed tools due to test rig complexity. Some of them show unexpected behavior for some blades which require deeper investigation (damper not in the nominal position, contact and intrinsic mistuning).

Starting from the current bladed disk a simplified disk is produced for dynamic test at AerMec Laboratory of Politecnico di Torino, for a better understanding of the blade array dynamics in different configurations: nominally tuned, mistuned, linear and nonlinear response.

The blade geometry, the under-platform damper, the distance between the blades at the platform/shank regions of Polito and Sangone rigs are the same. Despite the lower number of the blades, the Inter Blade Phase Angle has been set to be the same for the excited Nodal Diameter modes of the reference disk (ND6, ND24). In this way, the kinematics at the blade platforms is the same for the reference disk. In particular, the ratio between the number of blades of the original assembly (144) and the scaled one (48) can be used to scale the ND of interest as well (see table 1.1).

Table 1.1: Scaling of the ARiAS configuration and the configuration used by AerMec Laboratory.

	Old	New
Blades	144	48
Nodal diameters	6	2
Nodal diameters	24	8

Figure 1.28: Polito Rig new parts.
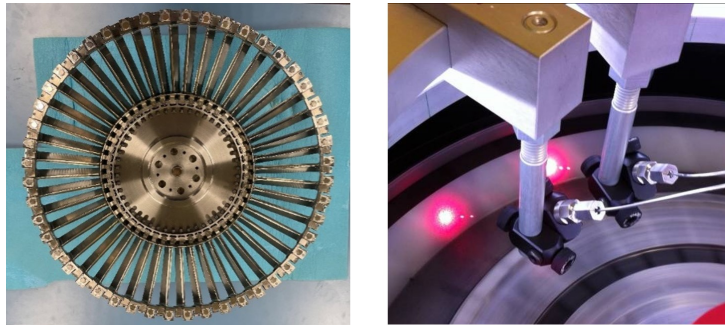
Figure 1.29: Aermec assembled disk and BTT probes.

BTT and magnetic excitation has been used as in Sangone test. The mode shape excitation was kept by means of permanent magnets at leading edge and trailing edge and the force amplitude can be measured by loadcells applied at the non-rotating permanent magnet. The disk mode shapes are detected, as before, by the Blade Tip Timing measurement system available at the AerMec laboratory with up to 6 sender-receiver optical laser sensors for blade vibration detection and one rev sensor for the disk rotational speed.

In figure 1.28, 1.29 and 1.30 the images of the new parts and the test rig.
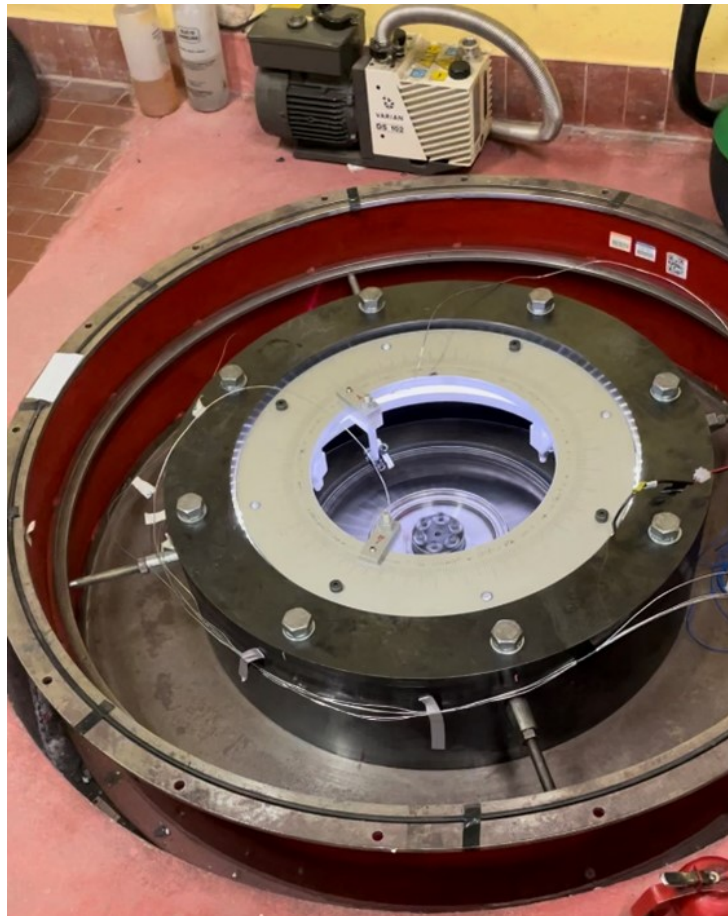
Figure 1.30: PoliTo test rig.

Chapter 2

Rotor dynamics

In the present thesis work, we are going to deal with a so called bladed disk. In order to design and optimize a bladed disk is important to know the excitation which are applied to the blade and the operative range of the blade.
The excitation applied to the blade are usually non stationary and are the main responsible of high cycle failures. To study the response of bladed disks to these forces, is important to study its dynamics to predict the natural frequencies and the mode shapes, in order to avoid a resonant condition and instabilities in the operative range.

2.1   Cyclical symmetry and modal analyses

The bladed disks are often analyzed by using the cyclic symmetry condition. This thanks to the fact that, in the ideal case, neglecting the inherent differences between each blade, they are the identical each other and the disk has homogeneous properties, so the balded disk can be divided in slices each of them equal to the others, so the analyses of only one of this sectors is possible without differences in the results obtained by considering the whole bladed disk, which would require high memory and computational power.

Thus, in this way, we can decompose the overall system in single blocks which interact each other. A single sector is characterized
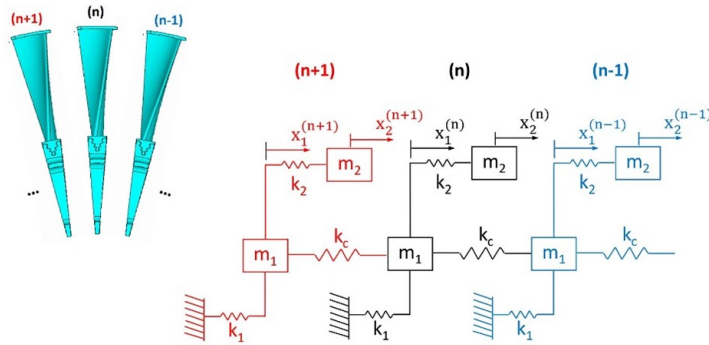
Figure 2.1: Turbine sector model [21].

by an angle $\alpha = \frac{2\pi}{N}$=sector angle, where N=number of blades.

In Finite Element Analyses (FEM) we discretize the bladed disk in Finite Elements and we can obtain, by applying the fundamental equation for a solid without damping:

$$[M]\{\ddot{x}\} + [K]\{x\} = 0 \tag{2.1}$$

where [M]=mas matrix, K=stiffness matrix and x=position vector of the finite element nodes degrees of freedom.

For every sector, we can decompose the position vector $\{x\}$ in a sub-set of nodal vectors:

$$\{x\} = \begin{Bmatrix} \{x^{(1)}\} \\ \{x^{(2)}\} \\ \vdots \\ \{x^{(N-1)}\} \\ \{x^{(N)}\} \end{Bmatrix}$$

where $\{x^{(n)}\}$ are the nodal coordinates for the n_{th} sector with $n = 1, ..., N$.

Every sector has n_n degrees of freedom and can be divided in three parts:

- $x_R^{(n)}$ = nodes on the right-hand side at the interface between two adjacent sectors;

a) ND=1   b) ND=2
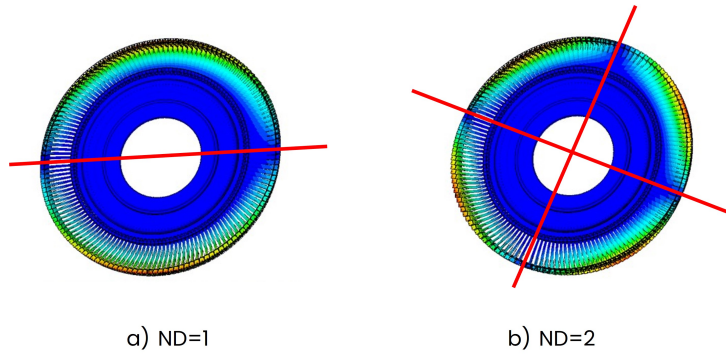
Figure 2.2: Example of ND=1 and ND=2.

- $x_L^{(n)}$ = nodes on the left-hand side at the interface between two adjacent sectors;

- $x_I^{(n)}$ = inner nodes in the sectors;

With that said, we can write the motion system of equations, before applying the cyclic symmetry condition, as:

$$(-\omega^2 [m^{(n)}] + [k^{(n)}])\{x^{(n)}\} = 0$$

where:

$$\{x^{(n)}\} = \begin{Bmatrix} \{x_R^{(n)}\} \\ \{x_I^{(n)}\} \\ \{x_L^{(n)}\} \end{Bmatrix}$$

and, since the left interface of the n_{th} sector coincides with the interface on the right of the $n_{th} - 1$ sector, we can connect the left and right interfaces with the following equation, thus enforcing the cyclical symmetry condition:

$$\{x_R^{(n)}\} = \{x_L^{(n)}\}e^{i\phi_n}$$

where ϕ_n =Inter Blade Phase Angle (IBPA) and represents the phase shift between adjacent blades in the mode shape.
In fact, we can have two types of mode shapes:

31

- **Real modes**: only one eigenvalue is present and all the points of the blade vibrate in phase with each other.

- **Complex modes**: this modes are characterized by a complex eigenvalue and the mode shape shows a traveling wave through the row. Based on the harmonic of the wave, one or more lines with zero displacement will appear in the row: this lines are called *Nodal diameters* (ND). In figure 2.2, an example of a bladed disk with nodal diameter 1 and 2.

So, for complex modes (where the real modes are only a particular case of the latter), a phase shift between adjacent blades is going to be present (IBPA) and the mode rotates, thus the sectors move with different phases.
Not every phase shift between the sectors is admittable. In fact, we can write the mode shape of the generic sector as:

$$\theta^{(n-1)} = \theta^n e^{-i\phi}$$

After N rotations of the eigenvector, in the sector n-1 we must obtain again the same eigenvector. This relationship can be expressed as:

$$N\phi = 2\pi h$$

So, after N rotations the sum of the $N \cdot \phi$ must be equal to 360° or 2π. In the above expression, we have h=harmonic index and is an integer.

The values of harmonic index admittable, and so of IBPA, depend upon the number of sectors in the row:

N even:
$$h = 0, 1, 2, \ldots, \frac{N}{2} - 1, \frac{N}{2}$$

N odd:
$$h = 0, 1, 2, \ldots, \frac{N-1}{2} - 1, \frac{N-1}{2}$$

Note that the harmonic index coincides with the before mentioned nodal diameter.
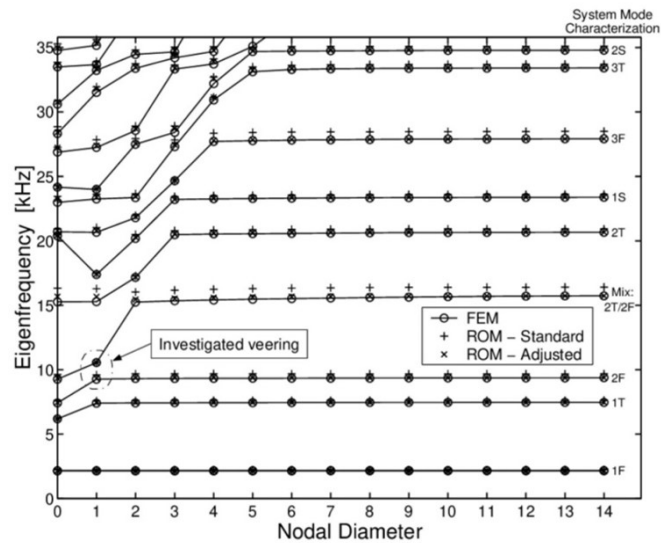
Figure 2.3: Example of FreND [3].

From this analyses we finally obtain the **FreND** diagram, which shows how the natural frequency of a mode shape changes with respect to the nodal diameters (or the harmonic index).
As shown in the figure 2.3, every curve is representative of a mode shape natural frequency and as the nodal diameters increase, so does the natural frequency up to an asymptotic value. This is due to a stiffening in the structure: higher nodal diameters mean more zones with zero displacement, hence a stiffer structure.

2.2   Aeromechanics in turbomachinery

The aeromechanics deals with the interaction between the fluid and elastic bodies inside the fluid. This interaction can occur in different ways and is wel summarized by the Collar diagram in figure 2.4.

The diagram, shows the mutual interaction which can occur between the physical phenomena in play: they can interact between each other, and the study of each field implies specific simplifications or, on the other way, they could be considered in the problem all together. In that case, we talk about *dyanamic aeroelasticity*.

For the study of dynamic aeroelasticity, we often use the Camp-

33
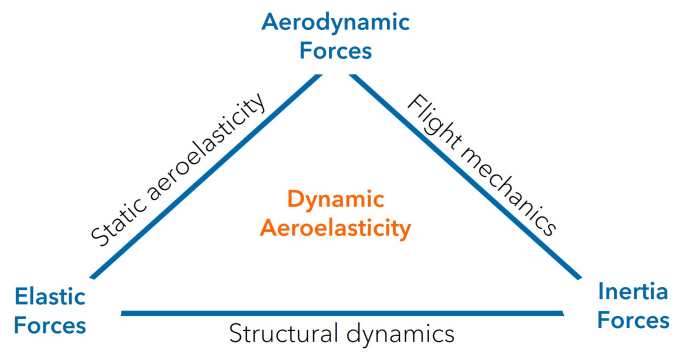
Figure 2.4: Collar diagram.
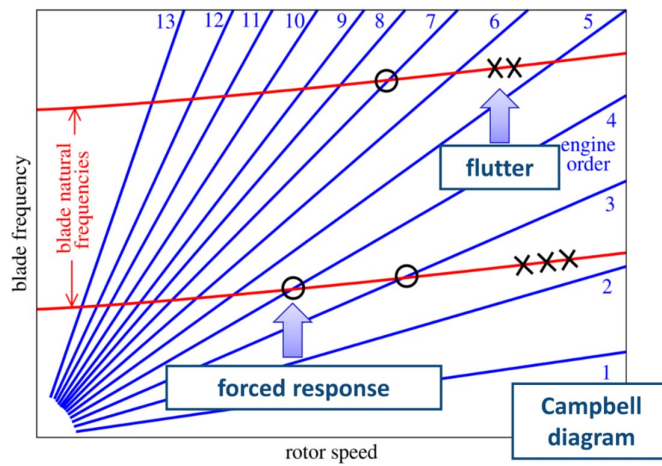
Figure 2.5: Campbell diagram example.[13]

bell diagram shown in figure 2.5. The diagram, shows on the y-axis the frequencies and in x-axis the engine rotational speed. In the graph itself, we represent the natural frequencies as a function of the rotational speed (in red). Meanwhile, the straight lines in blue represent the so called Engine Orders: the engine orders represent the phenomenons which occur as a multiple of the engine rotational speed. So, the engine order 3 is a curve which tells us that a phenomenon happens with a frequency 3 times the engine rotational speed.

When the curves of the natural frequency intersect the engine order curves and the intersection is inside of our operational rotational speed we have an instability, hence resonance.

The aeroelastic phenomenons which happen with a frequency proportional to the engine rotational speed are called *Forced response* and a typical example, shown in figure 2.6, is that of the disturbs from the wake of the nozzles on the rotating blades.

On the other side, we can also have another type of aeroelastic phenomenon, which is the one analyzed in the current thesis work: the *Flutter*. The flutter, is an aeroelastic phenomenon which is auto excited and self-sustained, hence it appears at a given rotational speed and with a certain frequency as a instationary force on the blade. This force is due to the interaction between the fluid and the structure: as the blade moves, the aerodynamic forces do not adapt instantly to such change, hence the circulation in the blade does not instantly adapt, there is a shift between the aerodynamic forces and the blade displacements.

This shift could be so big that, if we imagine an airfol moving up and down, when the airfoil is moving upwards, the lift instead of decreasing could be reaching it's peak value, which should have been reached before, when the blade was moving downwards. This causes a net increase in the blade energy: the air surrounding the blade is feeding energy to the blade itself, hence increases the amplitude of the vibrations.

This phenomenons could lead to a limit cycle oscillation, and thus to HCF problems, or even worse to a rapid increase in amplitude and hence a rapid failure of the component.

In this thesis, the parameter we analyze to evaluate whether the
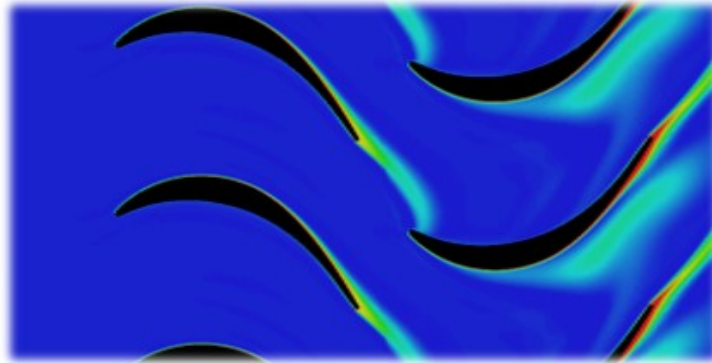
Figure 2.6: Example of forced response.[13]

blade is or not stable to flutter, is the *aerodamping*, defined as:

$$\xi = \frac{-L}{8\pi E_k}$$

where L=work done by the fluid on the blade and E_k=blade kinetic energy. The blade itself vibrates with a selected mode shape and does not feel the influence of the fluid, but the fluid ha to adapt to the movement. We thus analyze the work done on the blade.

Regarding the results obtained, we extract the Aerodamping plots as a function of the IBPA, shown in figure 2.7: if the aerodampong parameter is positive then the blade is giving energy to the fluid thus the blade is stable, if the aerodamping is negative, the blade is receiving energy from the fluid, so the blade is going to be unstable.
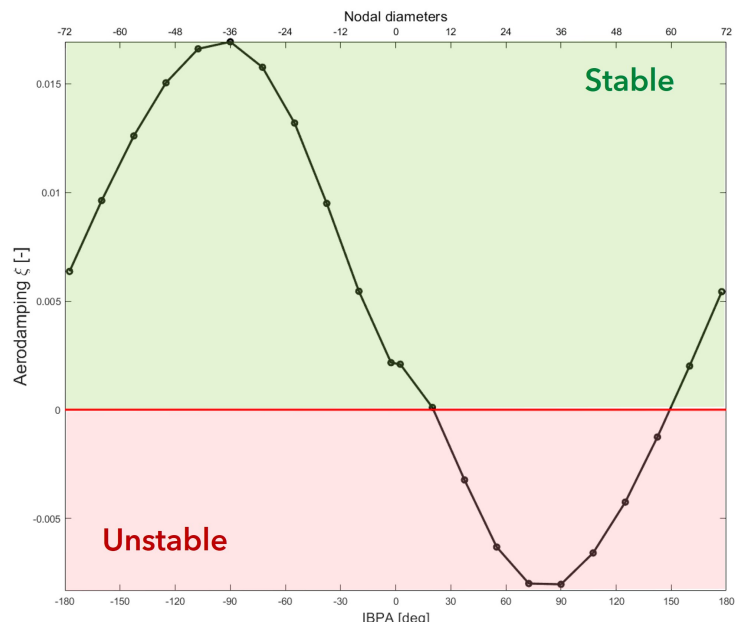
Figure 2.7: Example of aerodamping plot.

Chapter 3

Flutter stability analyses

3.1 Introduction

In the present thesis work the objective is to study a group of configurations tested inside the ARiAS project and verify what is the effect of the different parameters on the flutter stability analyses. Specifically, the flutter stability analyses aim to understand the start of the flutter, rather than its evolution, thus assessing whether or not the blade is unstable for a given mode shape and a given vibration frequency.

In fact, the software which have been used, or specifically, the solvers we used, do not guarantee the coupling between the aerodynamic forces and the structure, but rather o one-way coupling, where the structure and influences the aerodynamics but at the same time the aerodynamics does not influence the structure. More on that in the next sections. With those premises, the only thing we can measure is the blade stability at the start of the movement which, even though simplified with respect to the fully coupled approach, is a rather difficult task.

Thus, in the present thesis, we are going to focus mainly on the mistuning effect, but also other effects are going to be take into account.

3.2 Test description

As mentioned previously, the present thesis deals with the flutter stability analyses of the ARiAS project bladed-disk. Regarding the analyses carried in this thesis work, different tests have been performed. All of the tests have been done only from a numerical point of view, with a flutter solver which has been extensively validated by UniFi both previously and thanks to ARiAS project, respectively LARS and TRAF [12]. More on that later in the chapter.

With that said, the test matrix performed takes into account several configurations and conditions:

- **Solver effect**: for every configuration, two different solvers have been tested.

    - LARS: linearized solver;

    - TRAF: non-linear solver.

- **Rotational speed effect**: the rotational speed has been varied among the configurations to test the effect of the rotational speed. Every configuration is with respect of the nominal design speed:

    - N62: 62% of the nominal rotational speed, 1716 RPM;

    - N90: 90% of the nominal rotational speed, 2490 RPM;

    - N103: 103% of the nominal rotational speed, 2850 RPM;

- **Mode shape**: two mode shapes have been tested, Edge Wise (abbreviated to EW) and Flap (see figure 3.1);

- **Effect of mistuning mass and mistuning pattern**: The configurations tested included several tests regarding the effect of the mistuning mass. Regarding that, the objective was to see the stability of the blades without the mistuning mass, and see whether or not the addition of the mistuning mass to every blade (tuned configuration) would be beneficial in terms of flutter stability. After that, we investigated the possible effects of applying a mistuning pattern. In this case, we tested the effects of applying an alternate mistuning **1-0**, as shown in figure 3.2.
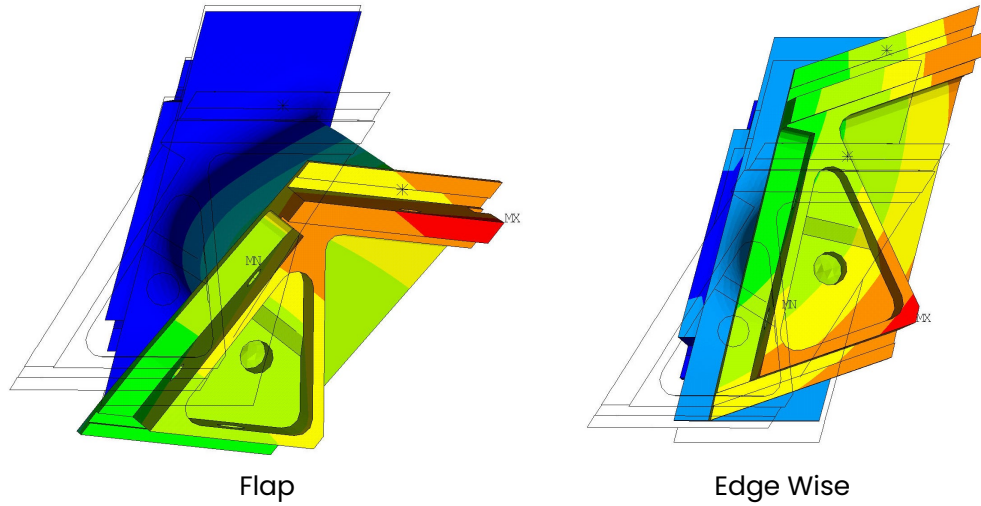
Flap   Edge Wise

Figure 3.1: Example of Flap and Edge Wise mode shapes. Tuned config-
uration.

Mistuning pattern 1-0-0-0   Mistuning pattern 1-0
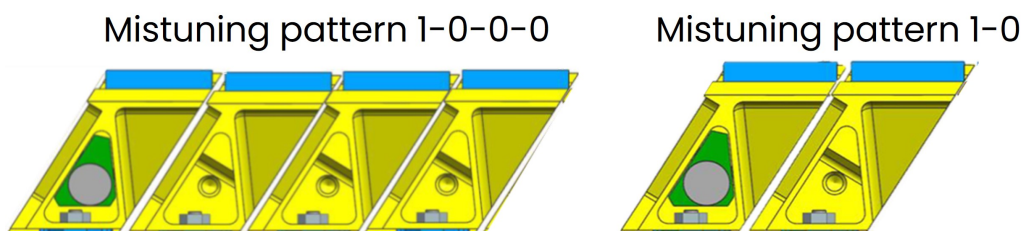
Figure 3.2: Mistuning patterns tesed. On the left, the alternated mistuning
pattern 1-0, on the left the pattern 1-0-0-0. Note, in green the mistuning
mass C2, in blue the rear magnet A1.
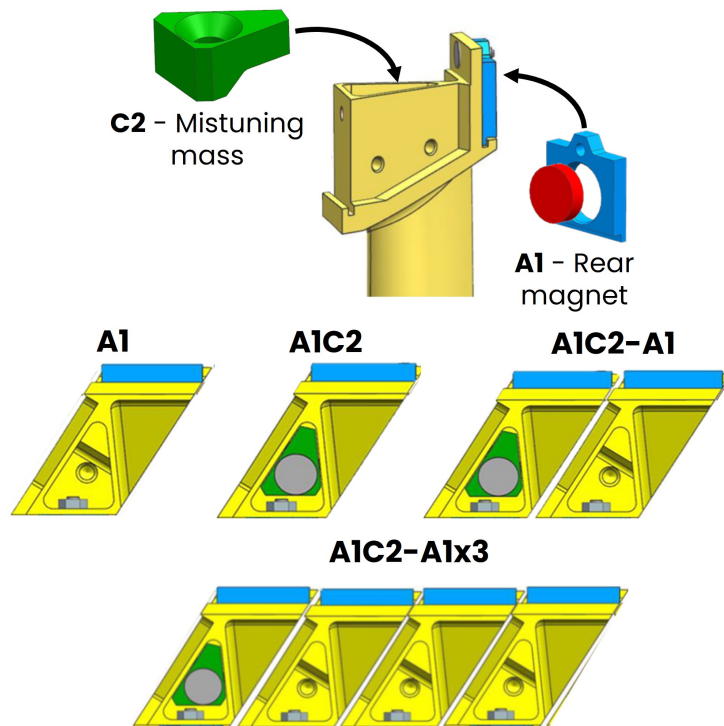
Figure 3.3: In the figure, the components used in the various configurations, which are shown in the lower part of the image.

Moreover, we further investigated the effects of another mistuning pattern, namely **1-0-0-0**, where every four blades one has the mistuning mass and three does not (see figure 3.2).

Note that every component mounted in the blade has a code name, which we are going to refer in the following pages for every configuration. In figure 3.3 are displayed the components name and the configurations associated to the different combinations. All in all, the configurations tested are the following:

- Tuned configuration **A1**: all the blades do not have the mistuning mass but only the rear magnet. A1 stand for the rear magnet;

- Tuned configuration **A1C2**: all the blades have the rear magnet and the mistuning mass. C2 stands for the mis-

tuning mass;

- Mistuned configuration **A1C2-A1**: this is the alternate mistuning pattern 10, as shown in figure 3.2. A1C2 represents the first blade, with rear magnet and mistuning mass. Meanwhile, A1 stands for the second blade with only the rear magnet;

- Mistuned configuration **A1C2-A1x3**: this is the mistuning pattern 1000, as shown in figure 3.2. As before, A1C2 represents the blade with mistuning mass, but A1x3 represents the three blades after, without the mistuning mass;

Note that every configuration mentioned above have been tested with every solver and rotational speed.

Moreover, regarding the different configurations, every one of them has been performed applying the cyclical symmetry condition, hence, for the tuned blades only one blade has been tested in every FEM analysis. Same can be said for the mistuned configuration but with two blades (and so on with the 1000, with four blades).

From now on, we will use the code names above (A1, A1C2 etc.) to refer to the various configurations tested. For example, when talking about A1C2-A1, we are talking about the mistuned configuration with mistuning pattern 10 (or the opposite, when talking about 10 we are talking about A1C2-A1). Meanwhile, in the following pages, some comparisons will be done between them and, since the number of blades differs from one another, when we will compare configurations with a different number of blades, we are going to enumerate the blades compared. As an example, when comparing A1 with A1C2-A1, the former is going to be referred simply as A1 (since only one blade is present), while with the latter we will refer to the blade without the mistuning mass as *blade 2*: we will number the blades from the blade with the mistuning mass from 1 to N, where N is the number of blades in the cluster (so, in this case, is 2).

Another trivial situation, which will appear in the next sections, regards the modes of the configurations. In fact, the for every modeshape the number of modes changes with the number of blades: for every mode shape, there is a number of modes equal to the

Flap1 mode
Flap2 mode
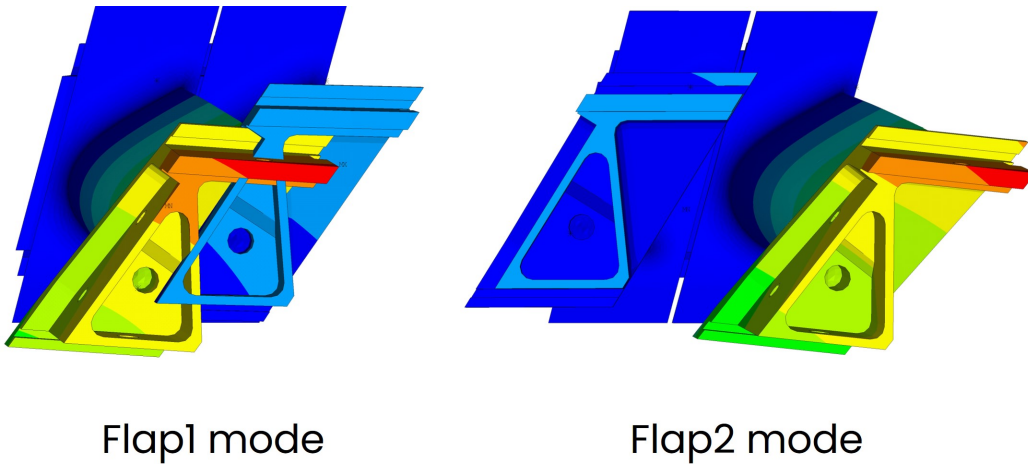
Figure 3.4: In the figure, an example of the Flap mode shape for the configurations A1C2-A1. In this case, we have two modes, one where the blade 1 moves more, here displayed on the left and named Flap1 and one where the blade 2 moves more, on the right, named Flap2. Blade 1 has the mistuning mass and blade 2 does not. The nodal diameter is ND=1.

number of blades.

So, considering as an example the mode shape **Flap**, we have for each configuration:

- **A1**: 1 mode (as said before, the number of blades in the FEM model is in this case equal to one since the cyclical symmetry condition has been applied);

- **A1C2**: 1 mode;

- **A1C2-A1**: 2 modes;

- **A1C2-A1x3**: 4 modes;

To distinguish between every mode, inside the two mode shapes Flap and EW, we will numerate each mode, as done before, with consecutive numbers, so in the case of the A1C2-A1x3 we will name the modes as Flap1, Flap2, Flap3 and Flap4. The first mode is going to be relative to the first blade, which is the blade with the mistuning mass.

The reason behind that is simple: when performing a modal analyses, every mode within a mode shape, is associated with a blade

43

which is moving more than the others, as show in the example in figure 3.4 relative to the configuration A1C2-A1, Flap mode shape. Note that the blade moving more on the right is the blade 1, which has the mistuning mass, and the other blade is blade 2, which does not have the mistuning mass.

Considering the configuration A1C2-A1, we have two blades with distinct natural frequencies: the blade 1 (with the mistuning mass), has a natural frequency lower than the blade 2, so when performing the modal analyses, the two modes are well distinguished, since they have two different natural frequencies. The Flap1 mode is associated to the blade blade 1 (blade 1 is the one which moves more) and Flap2 is associated to blade 2 (blade 2 is the one which moves more) as can be seen in figure 3.4.

As mentioned before, the number of modes is equal to the number of blades but, the modes of the configuration A1C2-A1x3 are cluster modes, hence, we cannot associate a mode precisely with a blade. Meanwhile, we can say that every mode in the blade A1C2-A1 can be associated with the two blades.
This is again due to the different natural frequencies of the blades: in the case of A1C2-A1, the blade number 1 (with the mistuning mass) has a lower natural frequency and is well separated from the natural frequency of the second blade, so the two modes are well distinguished and are associated to the two blades respectively.

On the other side, the same thing can't be said for the configuration A1C2-A1x3: in fact, while the first mode is always connected to blade 1 since the frequency is lower than the other blades and there is only one blade with that natural frequency, in the case of the other three blades, they all have the same natural frequency, which means that the mode is a cluster mode, hence given a mode shape, in the modal analyses for every nodal diameter we have four modes.

One mode is associated to the blade 1 and three are associated to the other blades, but which of them moves more changes among the nodal diameters since the mode is associated to the cluster, hence the three blades as a whole. In figure 3.5 we can see an example of a modal analyses at give nodal diameter where we can

a) Flap1 mode

b) Flap2 mode

c) Flap3 mode

d) Flap4 mode
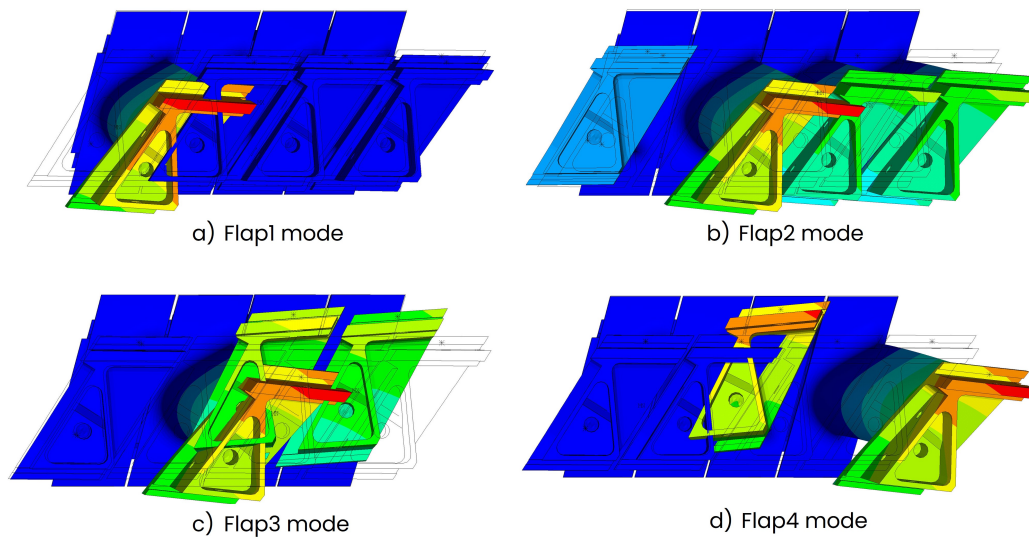
Figure 3.5: In the figure, an example of the Flap modes for the configurations A1C2–A1x3 at N62 and nodal diameter ND=1.

see that not every blades has a mode where moves more than the other.

For this reason, it was thought to be more convenient to simply enumerate the modes from one to the number of blades in the configuration in order to avoid any misunderstanding in the cases where modes are not well separated.

3.3 Flutter stability analyses workflow

The work flow for performing the flutter stability analyses follows a precise path:

1. **Modal analyses**: a modal analysis is performed for every configuration, at different rotational velocities. Between every configurations note that changes the maximum nodal diameter (different number of sectors due to the different number of blades analyzed).
   Cyclical symmetry condition is enforced. From every analysis we can extract the FreND diagram. Note that the maximum nodal diameters number changes with the number of blades in the configuration: in fact, if we analyze two blades,

45
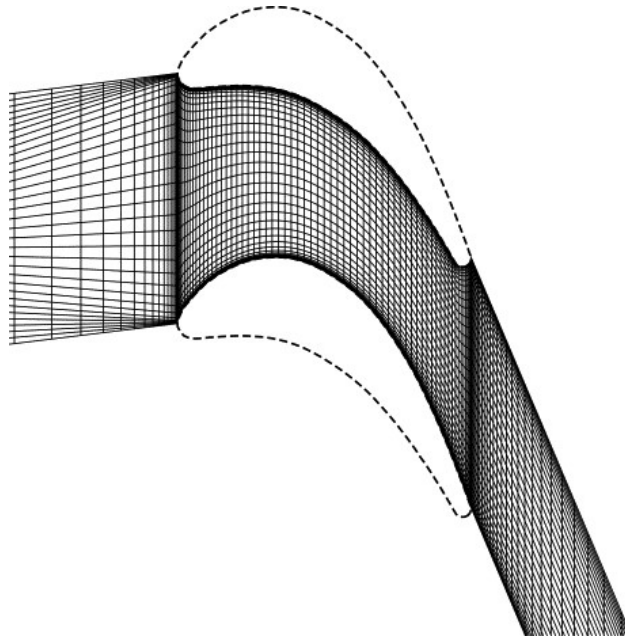
Figure 3.6: Example of H-type grid.[4]

72 groups of two blades are needed to reach the 144 blades of the ARiAS project.

This means that the maximum number of nodal diameters is 36 instead of 72. This means that when plotting friends, in order to obtain the same boundaries, we will plot the natural frequencies instead of as a function of nodal diameters as function of Inter-Blade Phase Angle (IBPA).

Note that the modes analyzed are complex modes, hence a rotating traveling wave forms.

2. **Steady CFD**: This CFD is needed since acts as a base for the aeroelastic calculations. It can be performed with various turbulent models. Moreover, it can be performed as a single row and with single or multiblock, hence calculating a single blade passage or multiples of it. The grid type is H-grid as shown in figure 3.6.

3. **Aeroelastic calculations**: this is the core of the flutter stability analyses.

In this part, another CFD is performed but this type we take into account the aeroelastci interactions. To do so, we have two options: **LARS** or **linearized** solver and **TRAF**, the non lin-

ear solver.

This part of the calculations is in both cases performed with an uncoupled approach between structure ans aerodynamics. In fact, the structure (or the boundary conditions) vibrates with a shape given by the mode and an intensity proportional to the it.

It does not feel the influence of the aerodynamics loads.

Meanwhile, the aerodynamics feels the structure movement and adapts to it with a phase lag as explained in previous chapter.

We thus obtain the aerodamping plots and evaluate the blade stability.

3.4 Solvers

As mentioned, we can find two types of solver in the present thesis work: the **LARS** and the **TRAF** code.

LARS   This is the linear code. In fact, the LARS code basically takes the modes and from that, extracts the real part of the modal displacement.

Once it is obtained, we can calculate the velocity disturb: this disturb must be small, ideally infinitesimal. We then calculate the velocity field as:

$$\underline{U}' = \underline{U} + Re[\hat{\underline{U}}_\delta e^{j\omega t}]$$

Where $\underline{U}'$=*disturbed velocity field*, $\underline{U}$=*mean velocity field* (previously obtained through the steady CFD), and $Re[\hat{\underline{U}}_\delta e^{j\omega t}]$=*real component of the modal disturbs*. We then finally place this quantities inside the governing equation (in our case the RANS equation) and we obtain two equations:

- Mean flow equation;

- Modal disturbs equation;

We can now solve the two equations, by applying the disturbs to the boundary conditions and linearizing the problem. [15]

TRAF The TRAF solver is similar, it also uses the modal analyses results but this time, instead of applying the disturb to the boundary conditions, **the blade itself vibrates with the specific mode**. To be more precise, the grid vibrates.

This means that the equations are resolved in time. For every time step, the CFD goes to convergence and then another time step is calculated.

The period of computation is given by the blade vibration frequency and the physical time step is calculated as:

$$\Delta\tau = \frac{2\pi}{\omega} \frac{1}{N_{div}}$$

with ω=*angular frequency*, N_{div}=*number of divisions of the blade vibration period*. [12]

Chapter 4

Solver effect

The two solvers give different results also due to the different nature of the calculations.

A typical LARS aerodamping plot can be seen in figure 4.1, relative to the configuration A1, mode shape Flap at N62.
In this case, we can see appreciate the sine-like curve pattern for the aerodamping curve. This pattern is typical for a tuned configuration and is seen, with a more or less pronounced shape, in every tuned test as will be shown in the chapter.
So, analyzing this configuration, it is clear it is heavily unstable, and a result like this would be totally unacceptable for a real case scenario.

The same can be said for the configuration A1 but mode shape EW. As shown in figure 4.2, the graph is like mirrored compared to the Flap mode shape.

But in this case, the difference is clear in the central zone: around IBPA=-20°, we have a clear peak value.
This peak is typical (though not always present) of the LARS solver and is due to an **acoustic resonance**: this peak, makes the LARS calculations not very precise in this region, causing a possible underestimation of the blade instability.

In fact, comparing the two curves in figure 4.3, where are represented the curves obtained with LARS and TRAF solver for the configuration A1 at N62 for EW mode shape, we can clearly see an un-
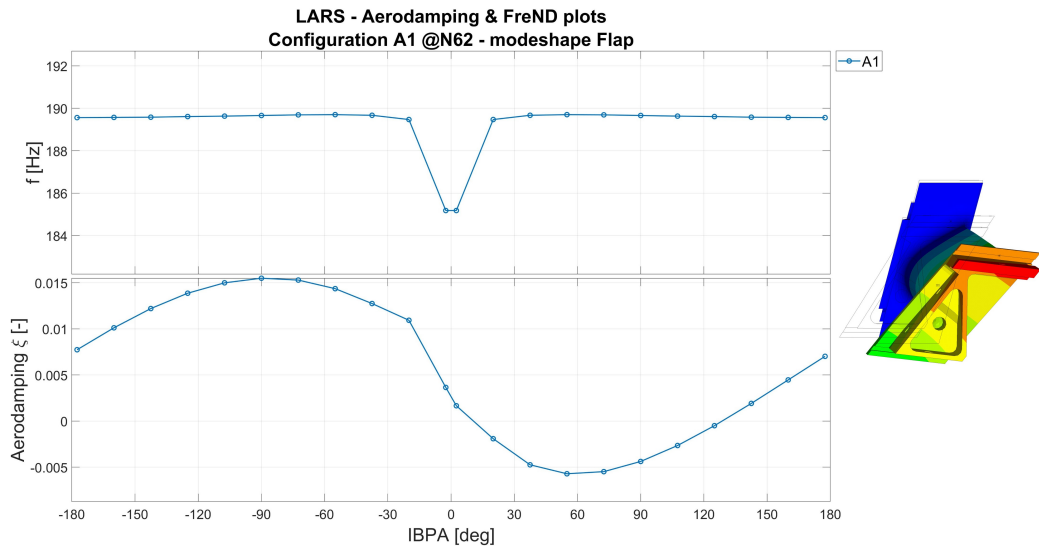
Figure 4.1: FreND and aerodamping curve for configuration A1, mode shape Flap at N62: LARS solver.
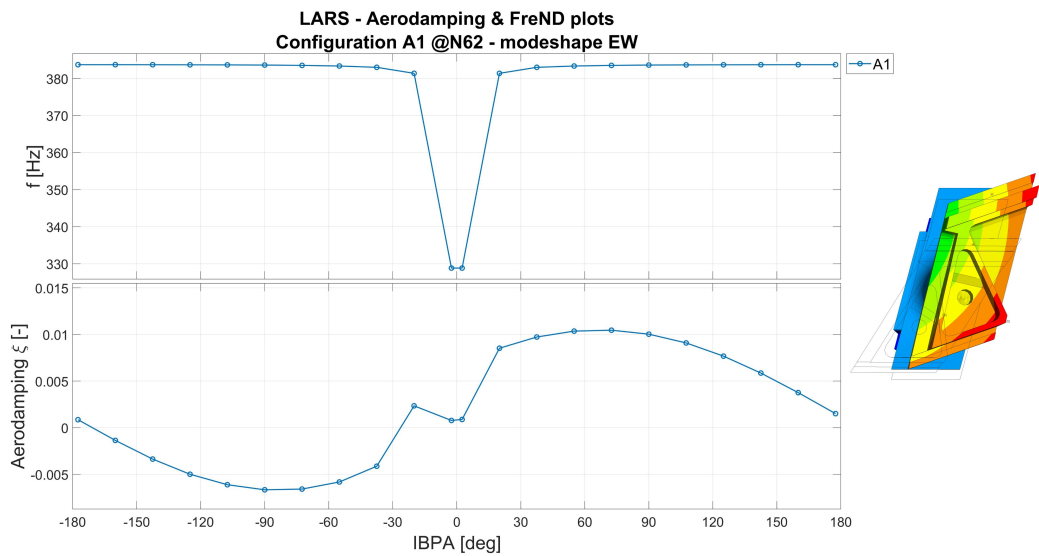
Figure 4.2: FreND and aerodamping curve for configuration A1, mode shape EW at N62: LARS solver.
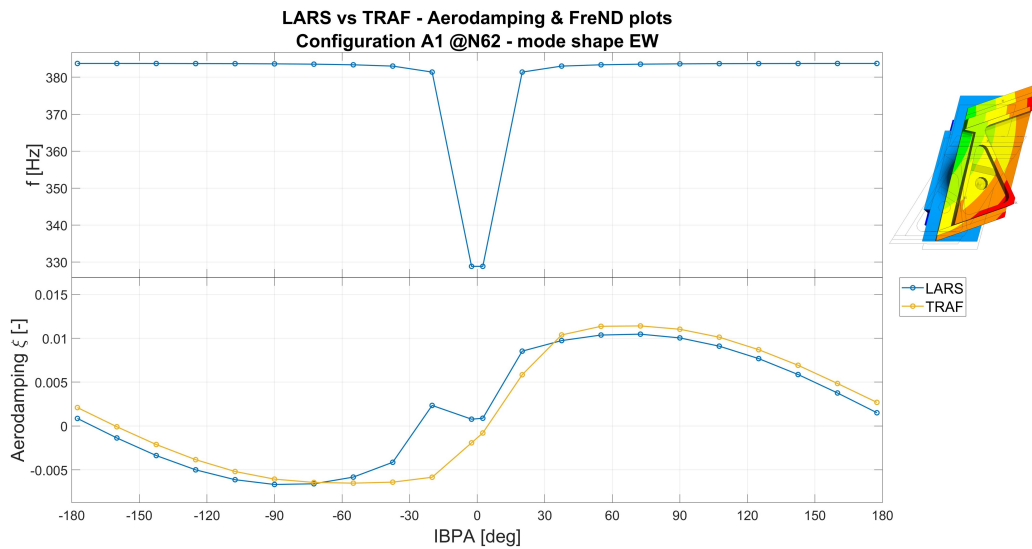
Figure 4.3: Comparison of LARS and TRAF solver results for configuration A1, mode shape EW at N62.

derestimation of the blade instability in the region between -72.5° and 2.5°.

Moreover, in the unstable region the is a shift toward the right, with the minimum values which moves towards positive IBPA.

Note that this underestimation is amplified by the resonance, but the same underestimation trend can be noted in figure 4.4 for the Flap mode shape, although with a different pattern.

Also, in this case, the unstable region in the TRAF case is much wider: extends from 20° to around 150°, meanwhile the LARS case goes from 10° to around 125°, meaning there has been an extension of the unstable range of the 13%.

In addition to that, the instability is much higher, with a lower minimum value. Again, also in this case there is a clear shift towards higher IBPA of the minimum aerodamping value.

This fact is crucial since, apart from the higher or lower instability, missing by great margin the instability region means that we could miss the unstable frequencies.

As can be seen in figure 4.4, where the aerodmaping and FreND plot are displayed, we can see that the natural frequency changes with the IBPA (ans so with the ND).

In our case, the disk has been designed to be stiff in order to en-

51
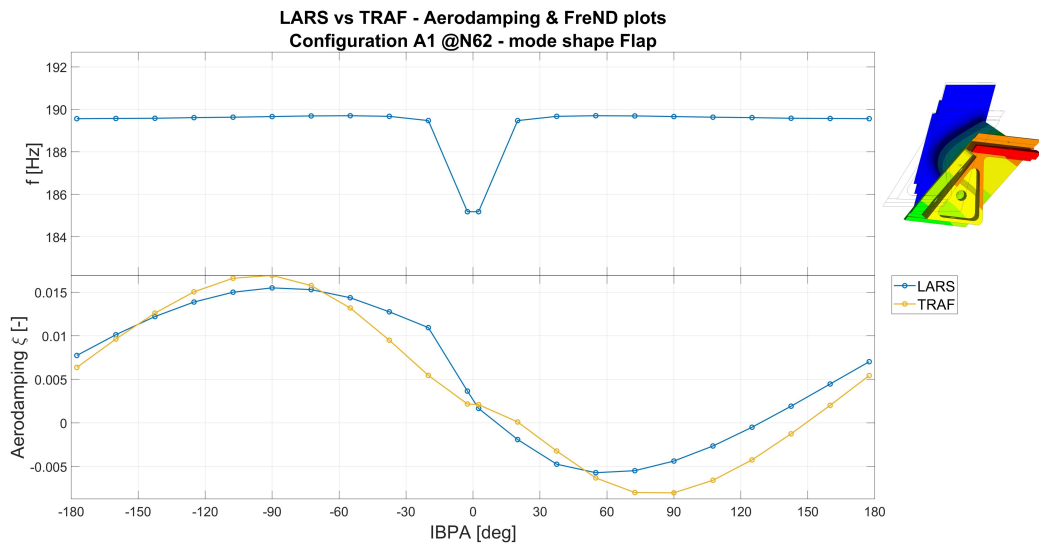
Figure 4.4: comparison of LARS and TRAF solver results for configuration A1, mode shape Flap at N62.

hance the blade modes, hence the FreND plot quickly flattens with increasing IBPA but, in a real case scenario, the frequency plot does not flatten this fast and keeps increasing and tends to the asymptotic value.

The same pattern can be seen not only at different rotational speed, but also with the configuration A1C2, as can be seen in figure 4.5 and 4.6 at rotational speeds N90 and N103 for configuration A1 and in figure 4.7 for the configuration A1C2 at N62 (all of them for EW mode shape).

Moreover, if we pay attentions to the graphs in figure 4.3, 4.5 and 4.6, we can notice that the gap between the LARS and the TRAF solver gets smaller with increasing rotational speed, indicating that the LARS solver, as could be expected since it is linearized, performs worst than TRAF at conditions near far from the design speeds.

This effect can be seen also for the Flap mode shape, shown in the figures 4.4, 4.8 and 4.9.

The difference between LARS and TRAF code is evident also for the configurations with more blades, like A1C2-A1 and A1C2-A1x3, as shown in figure 4.10 and 4.11, even though not as big as before, especially for the latter case. It has to be noted that the shape also
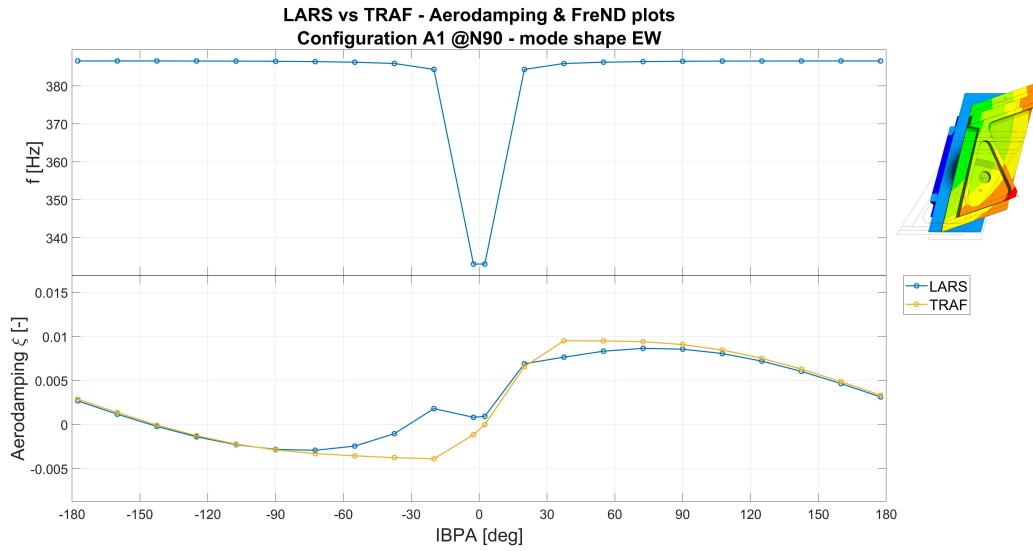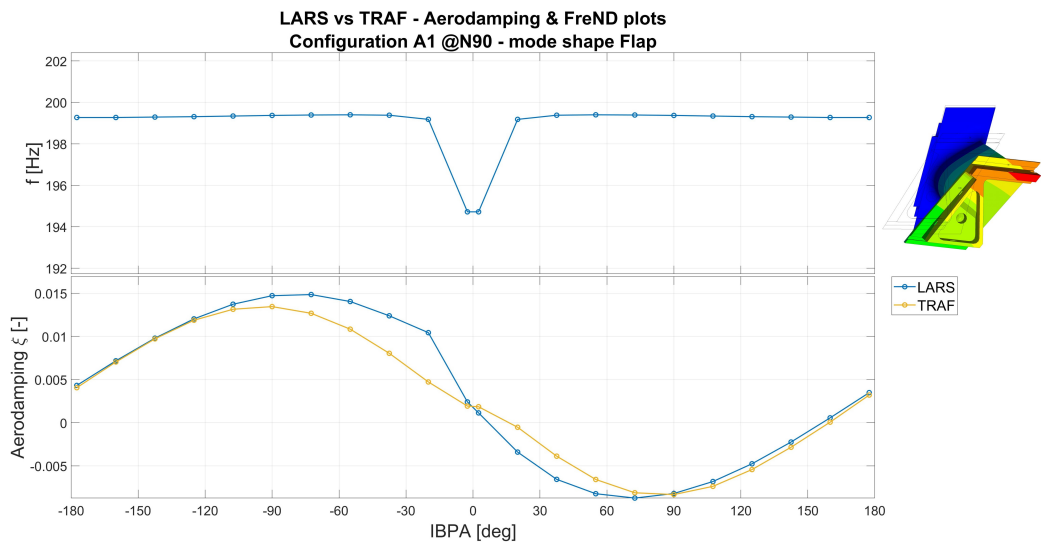
Figure 4.5: Comparison of LARS and TRAF solver results for configuration A1, mode shape EW at N90.
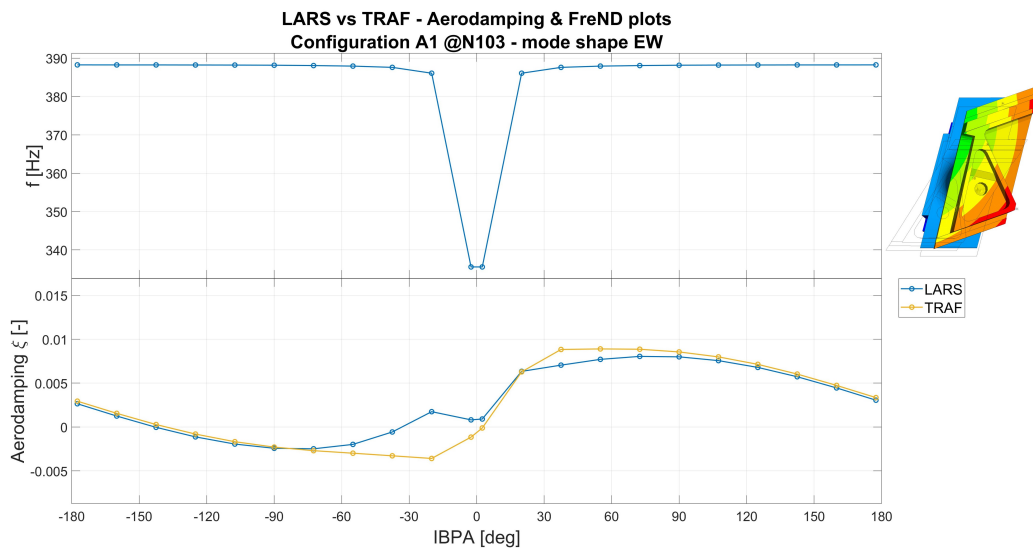
Figure 4.6: Comparison of LARS and TRAF solver results for configuration A1, mode shape EW at N103.
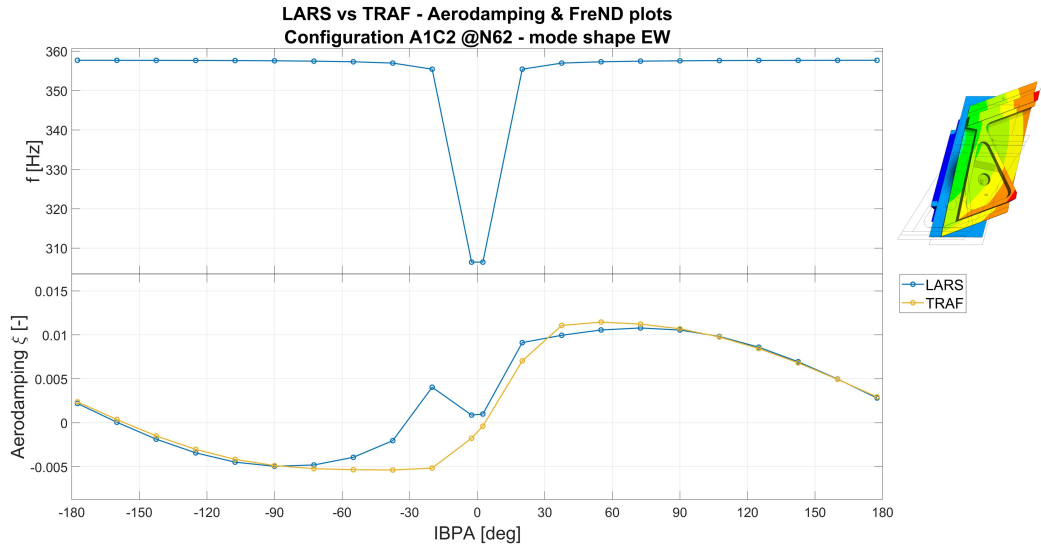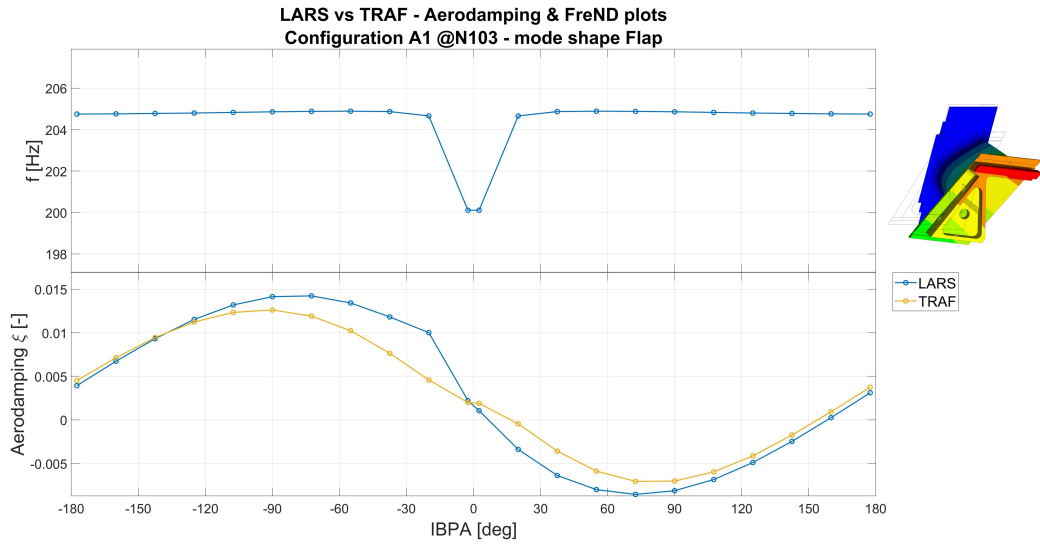
Figure 4.7: Comparison of LARS and TRAF solver results for configuration A1C2, mode shape EW at N62.
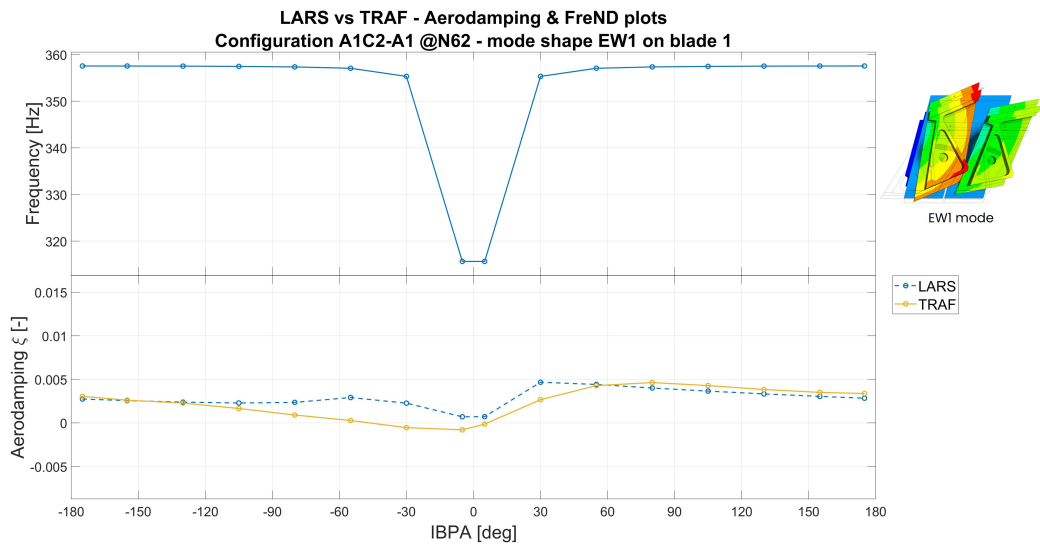

Figure 4.8: comparison of LARS and TRAF solver results for configuration A1, mode shape Flap at N90.
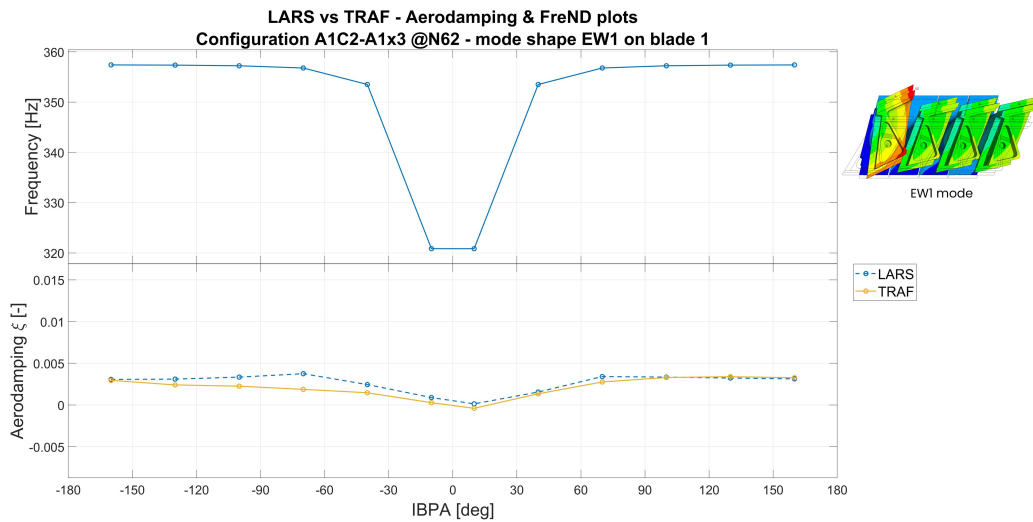
Figure 4.9: comparison of LARS and TRAF solver results for configuration A1, mode shape Flap at N103.

Figure 4.10: comparison of LARS and TRAF solver results for configuration A1C2-A1, Flap1 mode on blade 1 at N62.

Figure 4.11: comparison of LARS and TRAF solver results for configuration A1C2-A1x3, Flap1 mode on blade 1 at N62.

changes drastically in those two cases, being completely different from the sine-like of the two previous cases.
On the other hand, in some of those cases the LARS actually overestimates the blade instability, like in the case shown in figure 4.9, even though this is limited to very few cases.

In general, using the LARS solver could cause an underestimation of the blade stability, but on the other hand, we can generally find a good agreement between the two in terms of trends: as a rule of thumb we could say that in case the stability is marginal, hence we are close to the instability region, or in case we are far from the design speeds, we should consider to perform a TRAF analyses at the cost of an higher computational cost.

In fact, if we compare the computational cost for the configuration A1C2-A1x3 we can clearly see, as shown in table 4.1, a great increase in computational time of the two simulations, with an increase of 127%.

Given the higher accuracy and to avoid any misunderstanding, in the next sections we are going to consider only the stability analyses performed with the TRAF solver unless specified.

56

Table 4.1: Comparison between LARS and TRAF computational time.

	T [h]	$\Delta T\% = (T_{LARS} - T_{TRAF})/T_{LARS}$
LARS	2.6	–
TRAF	5.9	127%

Chapter 5

Rotational speed effect

The next stage is to evaluate the effect of the rotational speed in the different configurations.
In general, what we expect at an increasing rotational speed is a stiffening of the blade due to the rotational speed.
This effect can be seen in the FreND plot in figure 5.1 for the configuration A1, Flap mode shape.

The natural frequency increases with the rotational speed, a clear consequence of the stiffening due to the centrifugal force. To make a comparison, with the configuration A1 we have an increase of around 7.8% between N62 and N103.

This situation changes with different mode shapes: we still have a stiffening effect also with mode shape EW but the effect is more limited as shown in figure 5.2 (same configurations as before), with an increase of around 1% on average.

From this premises, we can thus analyze the effect on the aerodamping.
What we could expect is an increased stabilization with an increased rotation speed, hence with higher stiffness. This is partially true, since not in every mode shape this applies.
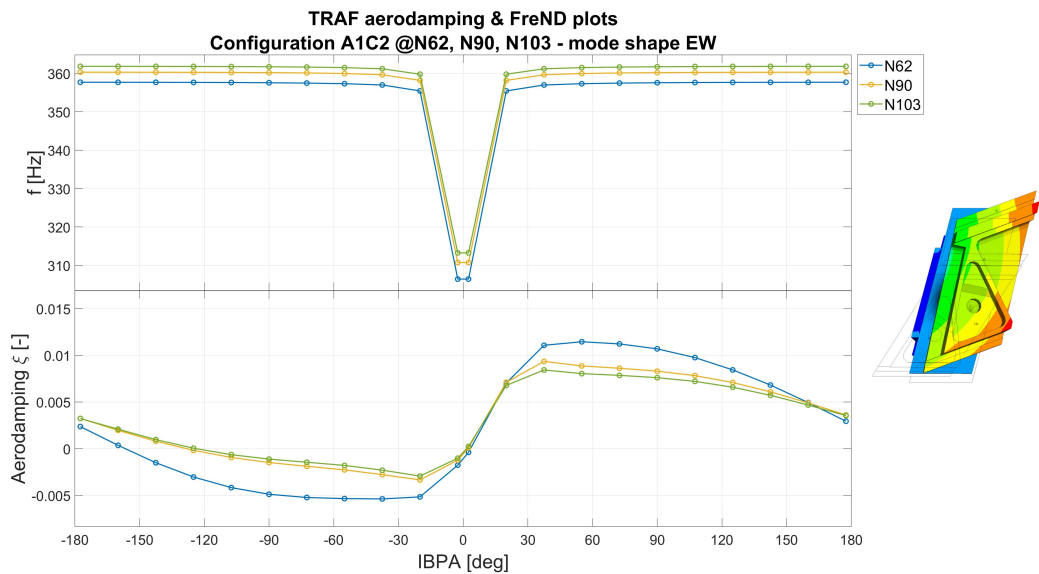
In fact, analyzing the mode shape EW we indeed find out that the an increasing rotational speed stabilizes the blade vibration, as
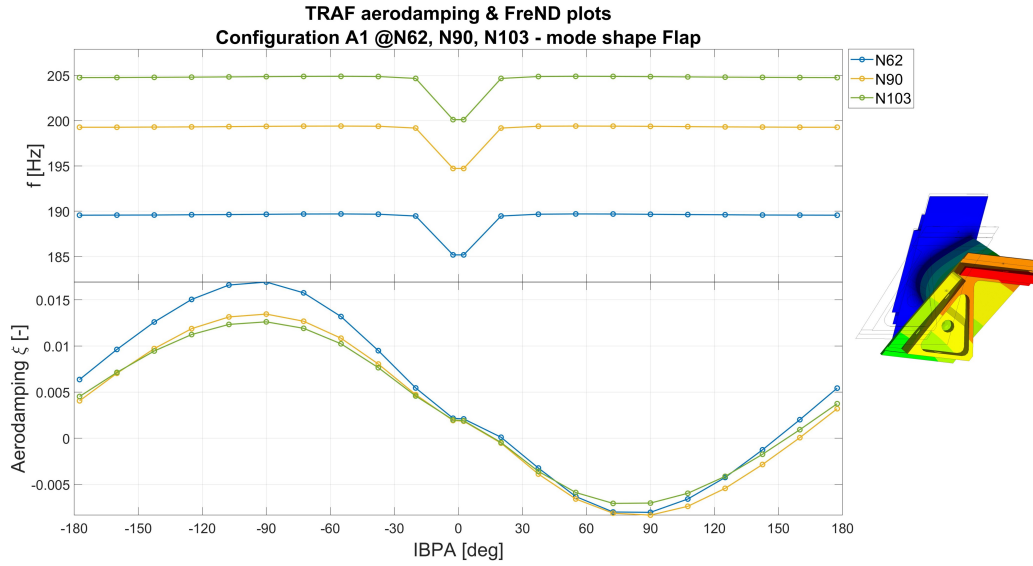
Figure 5.1: Effect of rotational speed for configuration A1, Flap mode shape and TRAF solver.
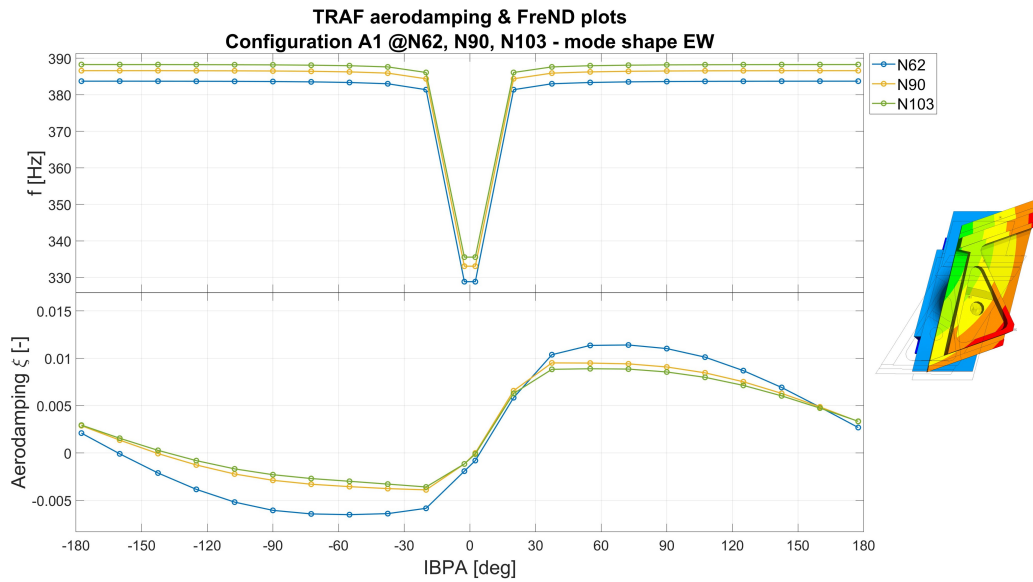
Figure 5.2: Effect of rotational speed for configuration A1, EW mode shape and TRAF solver.

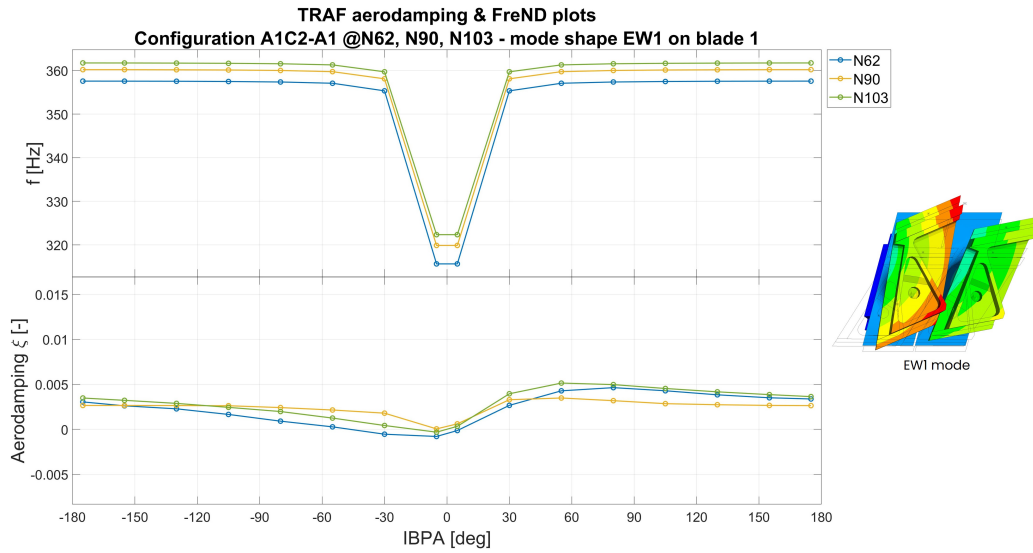**Figure 5.3:** Effect of rotational speed for configuration A1C2, EW mode shape and TRAF solver.

shown in figure 5.2 for the configuration A1.

Same goes for the configuration A1C2 in figure 5.3, always for the mode shape EW.

Things get a bit more complicated when analyzing the configurations A1C2-A1 and A1C2-A1x3, where the aerodamping curves are closer together making difficult to find a precise pattern in some cases. Despite that, we can see in figure 4.10 and 4.11 respectively that in general, at higher rotational speeds, we have an higher stability for the mode shape EW.

With that said, we still have to consider the Flap mode shape. Considering the configurations A1 and A1C2 in figure 5.1 and 5.6, we can see that between N62 and N90 the increasing in the rotational speed velocity atually destabilizes the blade but, on the other side, for the case of N103 there is an inversion in tendency, with a part where the N103 curve is more stable than the N62 case, with a later inversion compared to N62, even though still more stable than N90.
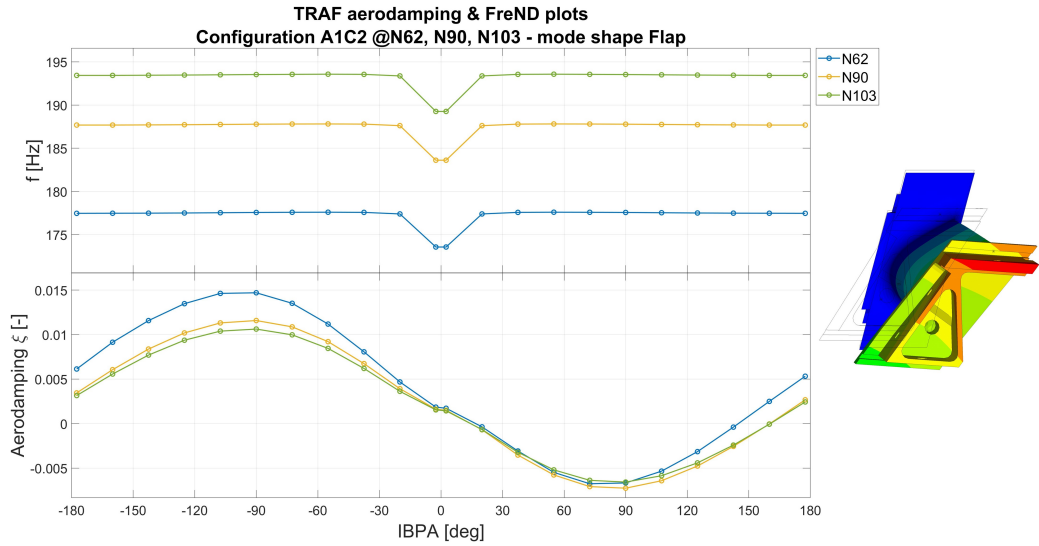
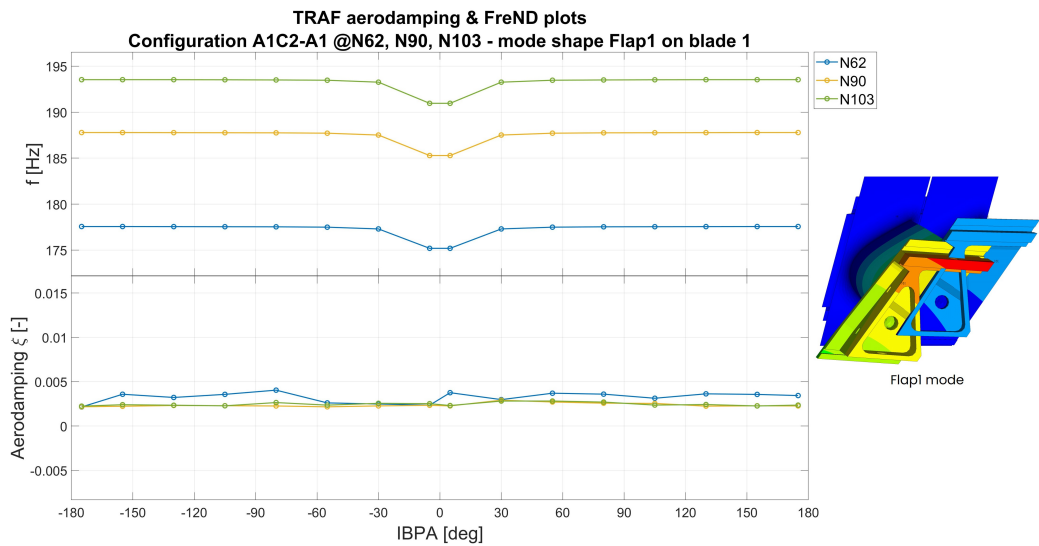But, on the other side, analyzing the cases A1C2-A1 and A1C2-A1x3

Figure 5.4: Effect of rotational speed for configuration A1C2–A1, EW1 mode on blade 1. TRAF solver.
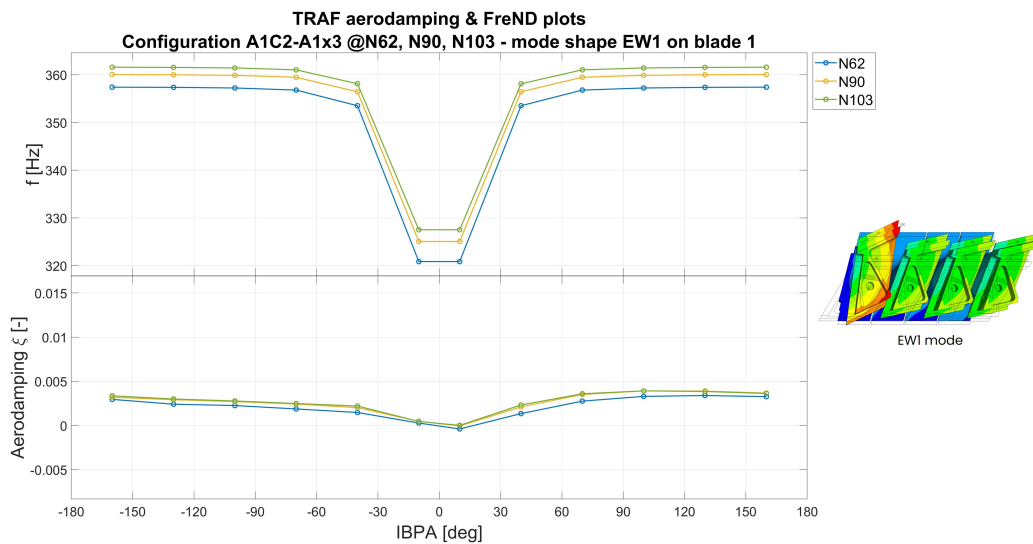
Figure 5.5: Effect of rotational speed for configuration A1C2–A1x3, EW1 mode on blade 1. TRAF solver.
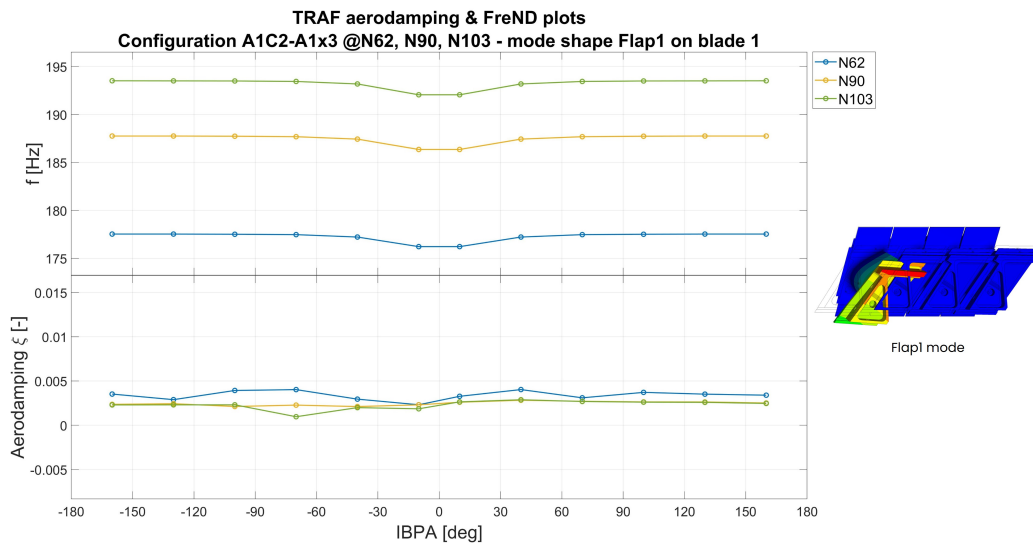
Figure 5.6: Effect of rotational speed for configuration A1C2, Flap mode shape and TRAF solver.

Figure 5.7: Effect of rotational speed for configuration A1C2-A1, Flap1 mode on blade 1. TRAF solver.
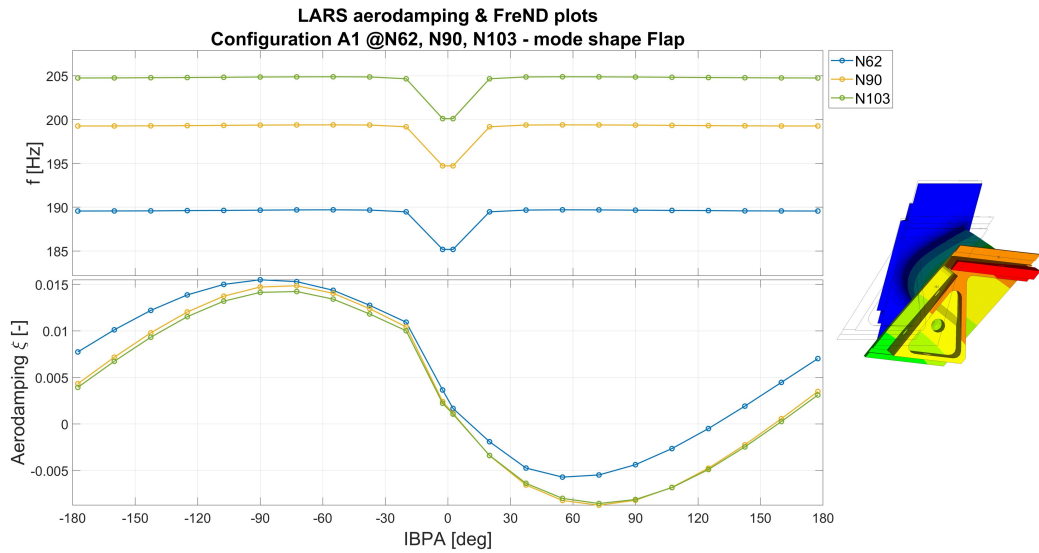
Figure 5.8: Effect of rotational speed for configuration A1C2–A1x3, Flap1 mode on blade 1. TRAF solver.

(Flap1 mode on blade 1), it is clear, as shown in figures from 5.7 to 5.8, that the N62 is generally more stable than the other, with the N103 usually more unstable.

So all in all, we can say that:

- Mode shape Flap: an increasing in rotational speed usually makes the blade unstable;

- Mode shape EW: an increase in rotational speed make the blade more stable;
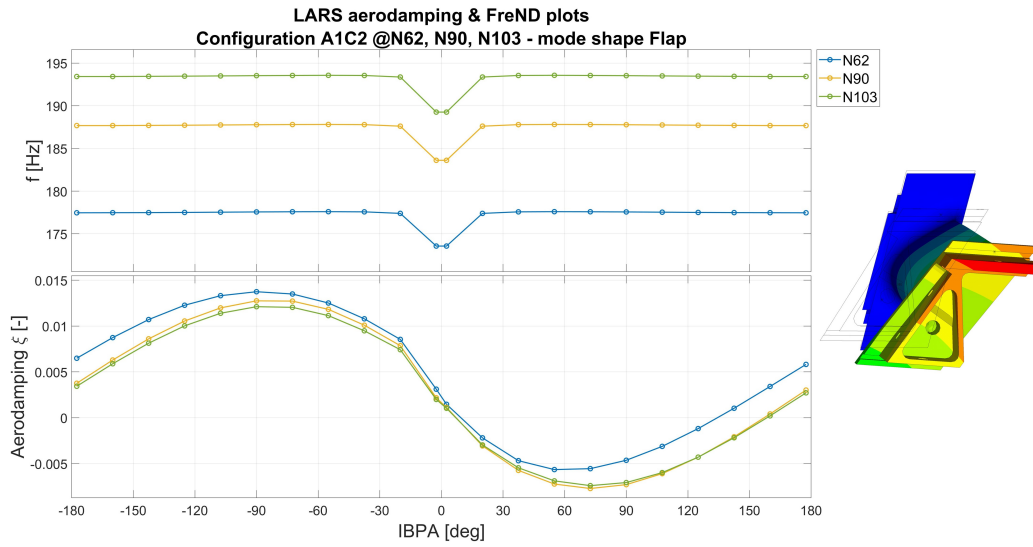
Note that it is interesting to see that this pattern can be also seen in the case of the LARS solver as shown in the figures from 5.9 to 5.16.
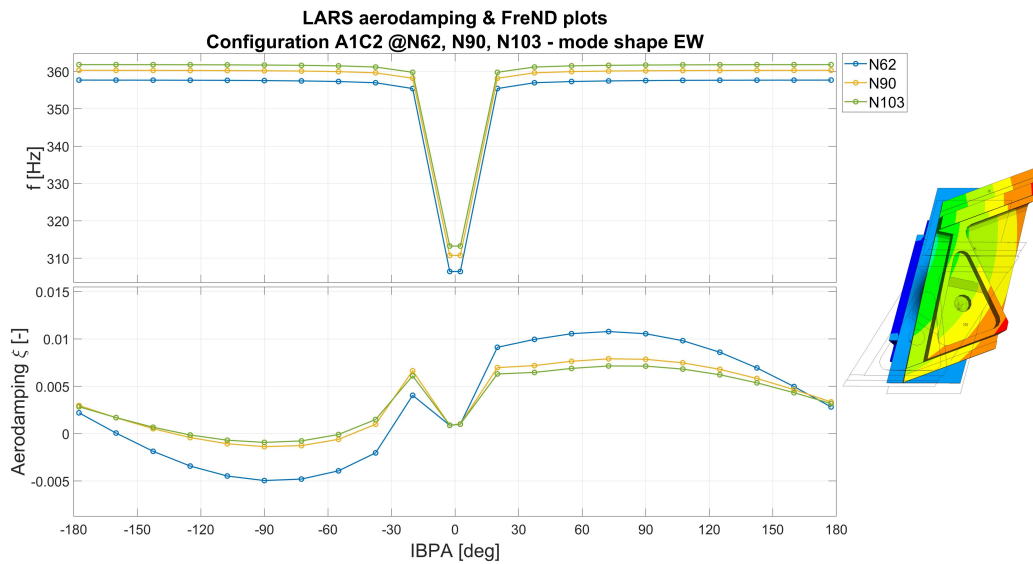
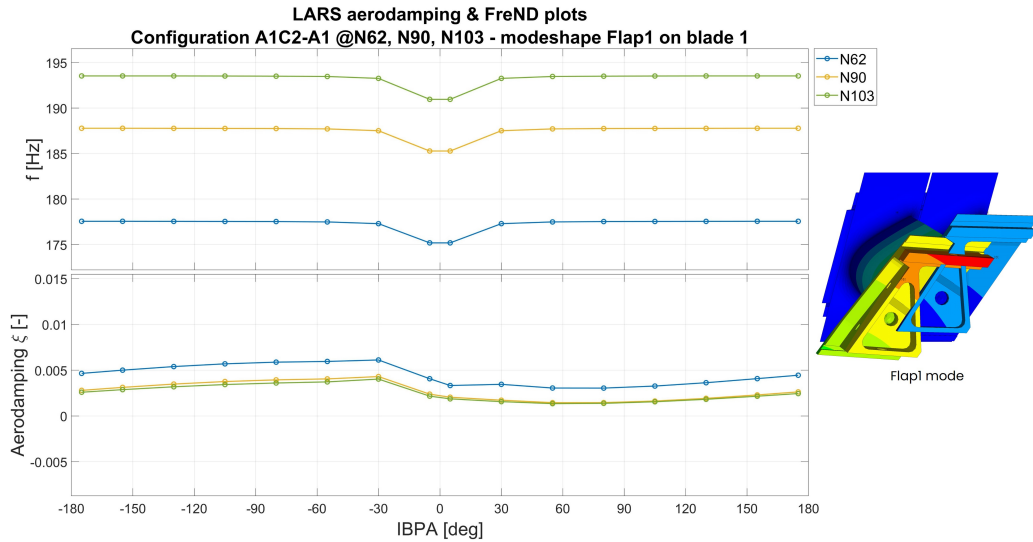**Figure 5.9:** Effect of rotational speed for configuration A1, Flap mode shape and LARS solver.
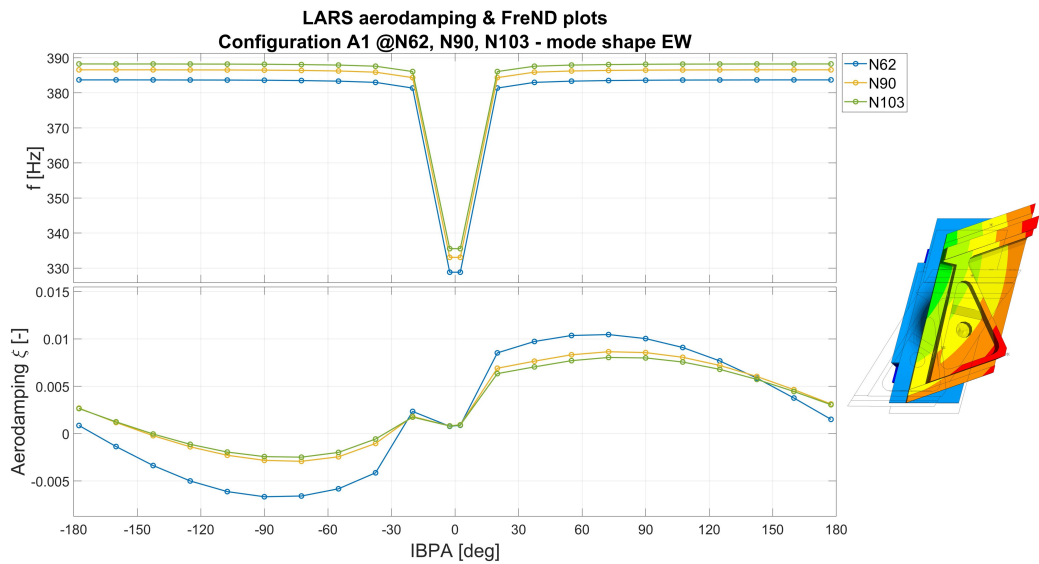
Figure 5.10: Effect of rotational speed for configuration A1, EW mode shape and LARS solver.
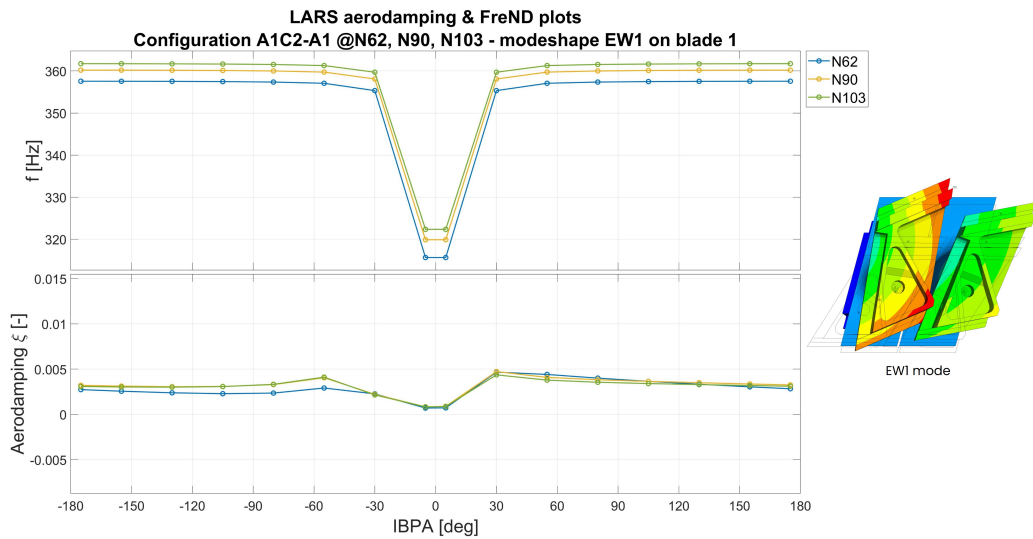
Figure 5.11: Effect of rotational speed for configuration A1C2, Flap mode shape and LARS solver.
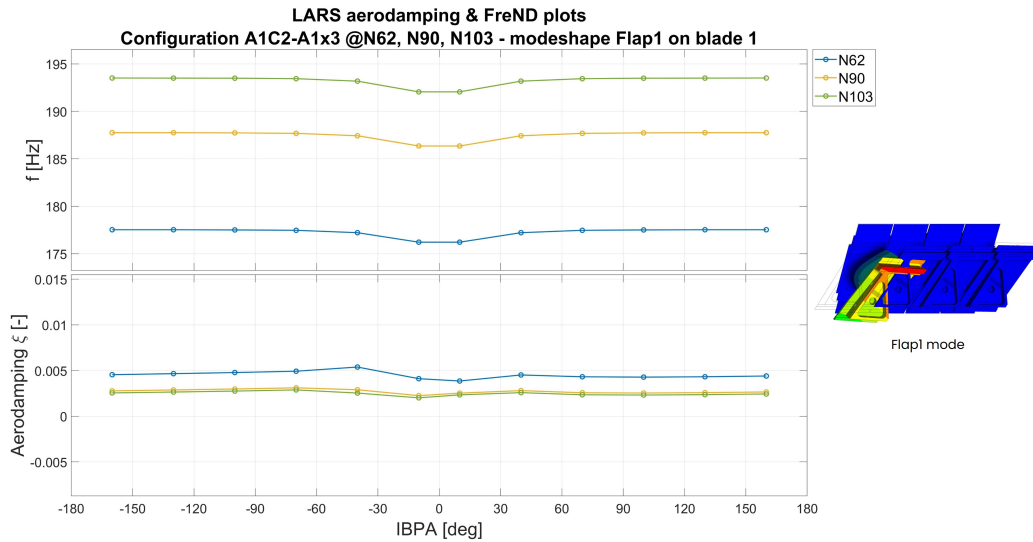

Figure 5.12: Effect of rotational speed for configuration A1C2, EW mode shape and LARS solver.

Figure 5.13: Effect of rotational speed for configuration A1C2-A1, Flap1 mode on blade 1. LARS solver.

Figure 5.14: Effect of rotational speed for configuration A1C2-A1, EW1 mode on blade 1. LARS solver.
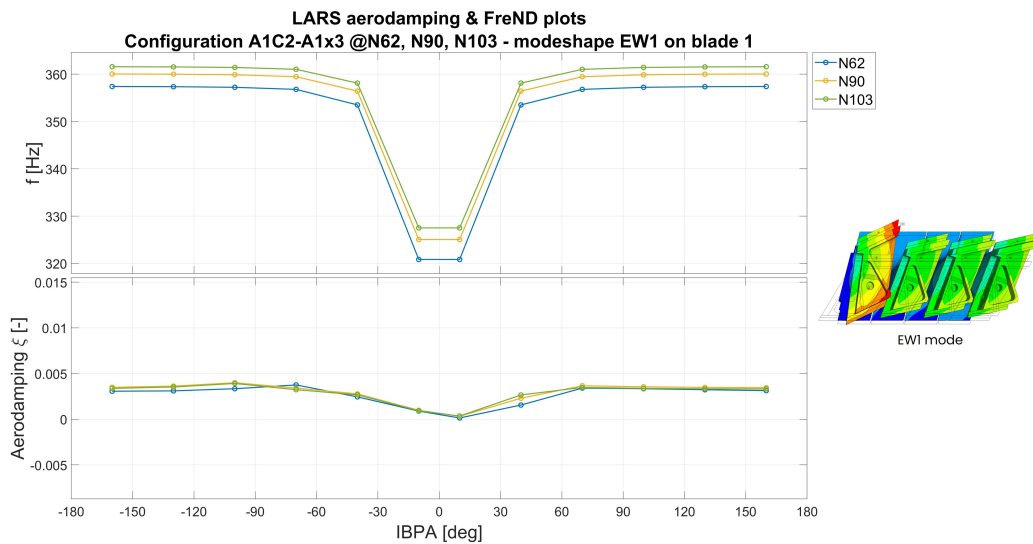
Figure 5.15: Effect of rotational speed for configuration A1C2–A1x3, Flap1 mode on blade 1. LARS solver.

Figure 5.16: Effect of rotational speed for configuration A1C2–A1x3, EW1 mode on blade 1. LARS solver.

Chapter 6

Effect of mistuning in flutter stability analyses

6.1 Tuned configuration: Mistuning effect

After analyzing the rotational speed effect, we wanted to analyze more in depth the differences by introducing the mistuning mass by comparing the tuned configurations with and without the mistuning mass, respectively A1C2 and A1 configurations, at different mode shapes.
As always, the mode shapes taken into account are the Flap and EW.

Starting from the Flap mode shape, we instantly notice, as shown in figure 6.1 for the N62 rotational speed, that the natural frequency is well distinguished between the two configurations thanks to the mistuning mass with a difference of approximately 7%.
Regarding the aerodamping, the mistuning mass actually has a stabilizing effect on the blade, but the stabilizing effect is marginal, with very little effect.

Same goes for the case with EW mode shape, as shown in figure 6.2, with the same stabilizing pattern as in figure 6.1 (same rotational speed, N62).

And again, same effect can be seen at various rotational speeds
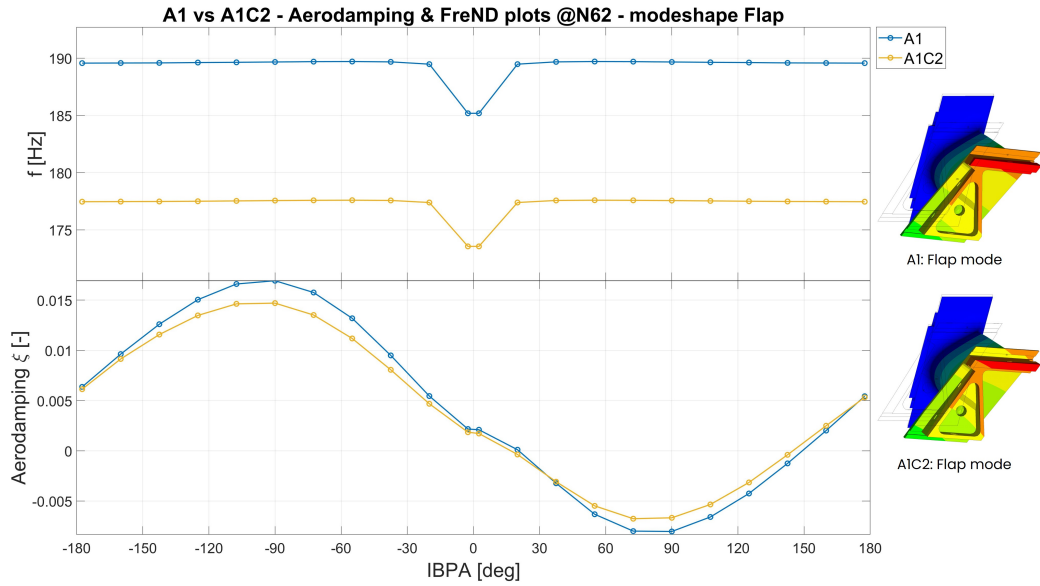
Figure 6.1: In the figure above, the aerodamping and FreND plots for the configurations A1 and A1C2 at N62 for the Flap mode shape.
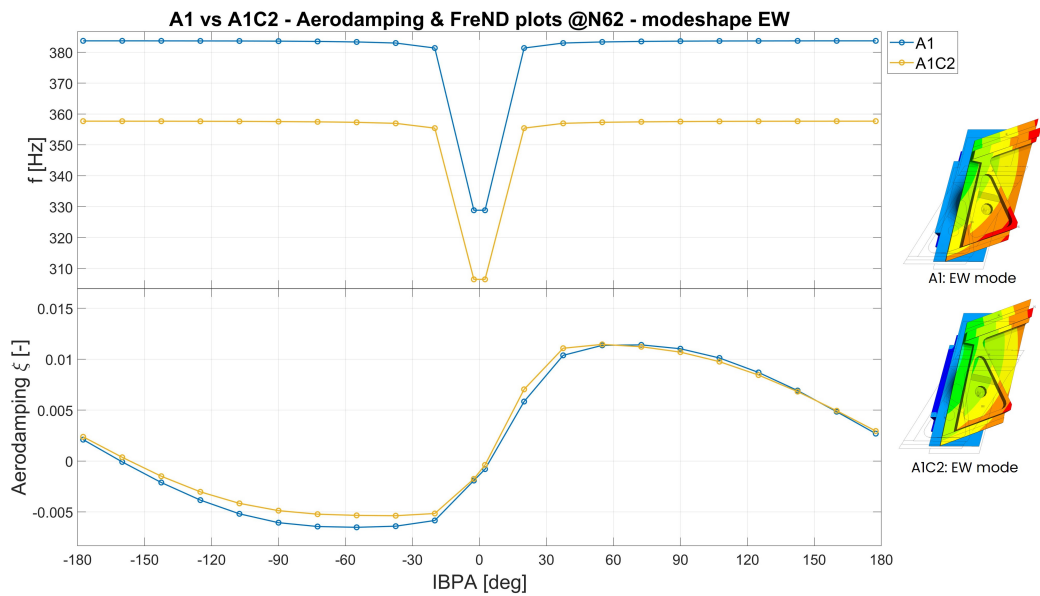
Figure 6.2: In the figure above, the aerodamping and FreND plots for the configurations A1 and A1C2 at N62 for the EW mode shape.
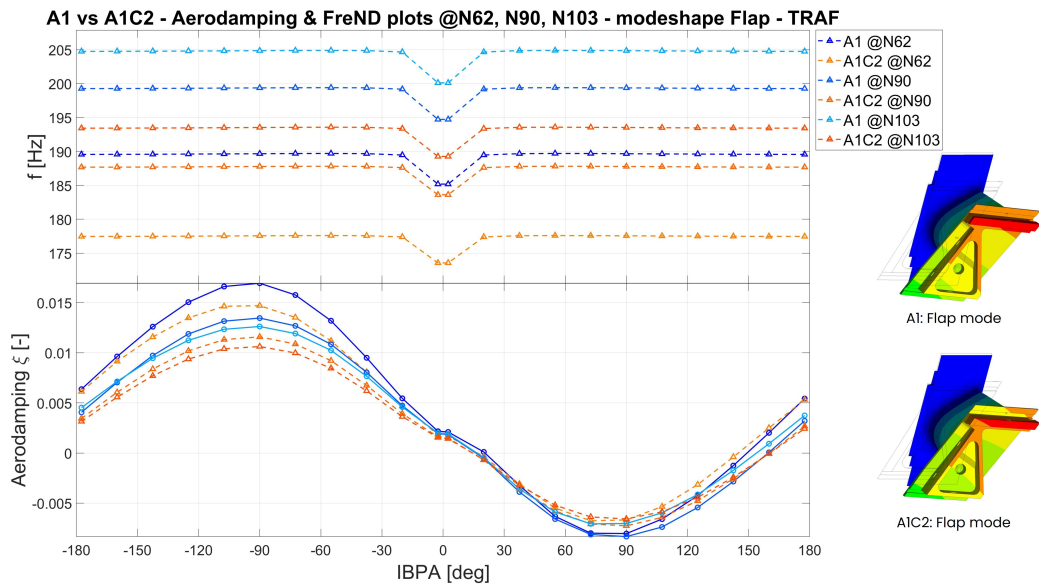
Figure 6.3: In the figure above, the aerodamping and FreND plots for the configurations A1 and A1C2 at N62 for the Flap mode shape.
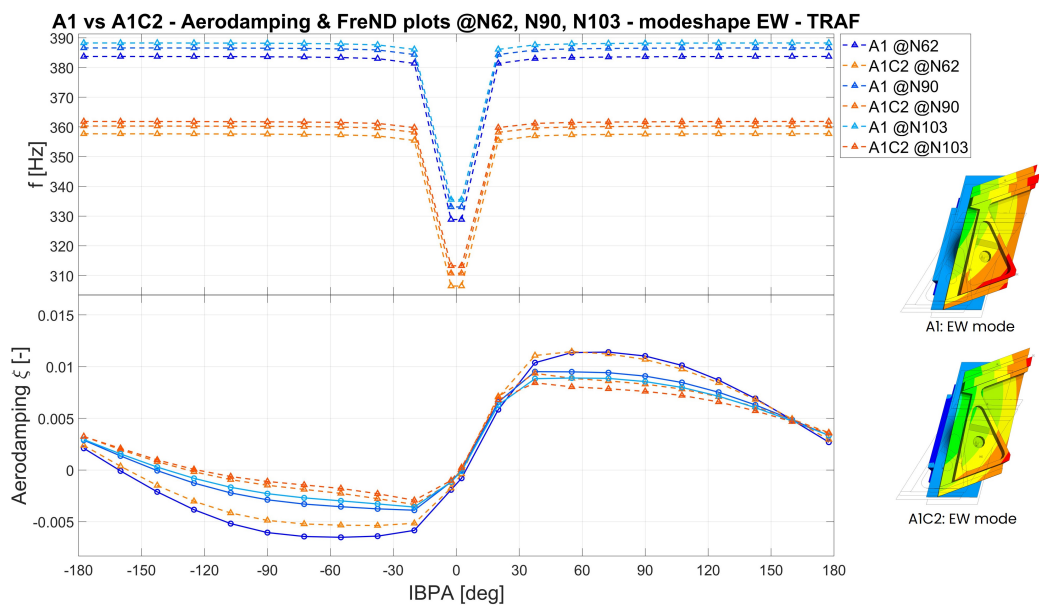

Figure 6.4: In the figure above, the aerodamping and FreND plots for the configurations A1 and A1C2 at N62 for the EW mode shape.

for the mode shape EW and Flap in figures 6.3 and 6.4.

So, adding the mistuning mass to every blade, in a tuned configuration, stabilizes the blade but it has a limited effect which does not guarantee to effectively stabilize the blade by making the aerodamping greater than zero.
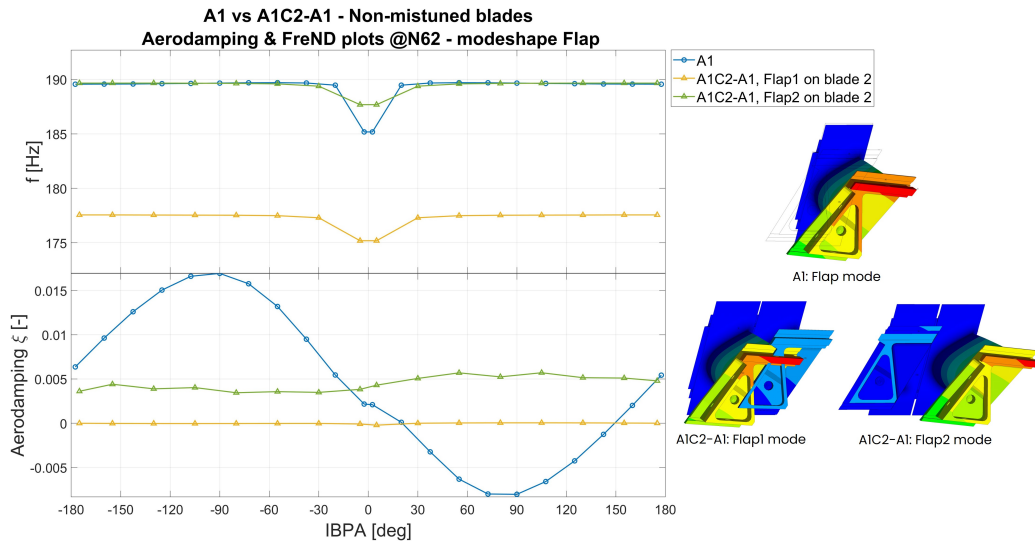
6.2 Mistuned configuration: Mistuning pattern effect

As a next step, we though whether applying a mistuning pattern to the blade would be beneficial since this could make the modes different from blade to blade and when one blade vibrates the other is not, thus damping the vibration.

To do so, as mentioned before, two mistuning patterns have been tested:

- Mistuning pattern 1-0: configuration A1C2-A1 (see figure 3.2);

- Mistuning pattern 1-0-0-0: configuration A1C2-A1x3 (see figure 3.2);

So, we will now analyze this two configurations. First, we are going to compare the results from the A1C2-A1 blades with the tuned configurations A1 and A1C2. The reason behind that is because A1C2-A1 has two blades: one blade with mistuning mass and one without, blade 1 and blade 2 respectively. This has been done in order to make the graphs clearer and most importantly to compare blades with the same configuration. Also graphs with aggregated data will be shown.
Therefore, we compare A1C2-A1 blade 1 with A1C2 and blade 2 with A1. Same goes for A1C2-A1x3, where we will compare blade 1 with A1C2 and blades 2 to blade 4 with A1 since they have the same configuration.

Figure 6.5: In the figure above, the comparison between the configuration A1 and A1C2-A1 for mode shape Flap at N62. The modes Flap1 and Flap2 are applied to the blade 2.

6.2.1   Mistuning pattern 1-0

The first possibility evaluated has been the mistuning pattern 1-0. We will now evaluate a comparison between A1C2-A1 blade 2 against A1, hence we will first compare the effect on the blades without mistuning mass, and then we will move to compare A1C2-A1 blade 1 against A1C2 (blades with mistuning mass).

A1C2-A1 blade 2 vs A1   The first comparison is between A1C2-A1 blade 2 and A1 at N62. Starting with the mode shape Flap, we can see in figure 6.5 the FreND and aerodamping plots for the Flap1 and Flap2 (see figure 3.4) modes applied on blade 2 in the aerodamping plots against the configuration A1.

As can be seen from the FreND plot, the Flap2 mode has the same frequency as A1, as one would expect since they have the same configuration. Meanwhile, the Flap1 mode has a lower frequency due to the mistuning mass, exactly as happened before in the comparison between A1 and A1C2. Moreover, note that the frequencies are the same also between Flap1 and A1C2.
Analyzing the modes in figure 3.4, we can expect that the aerodamping of the Flap 1 on blade 2 to be almost flat and indeed this is

72
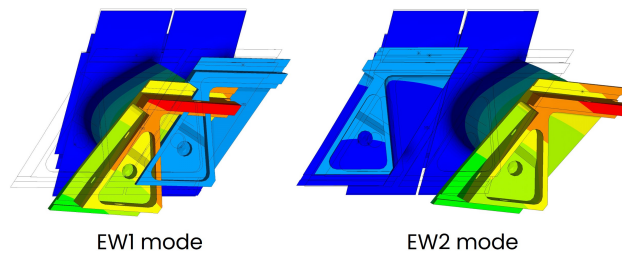
**Figure 6.6:** Example of A1C2-A1 EW mode shape at N62, ND=1.
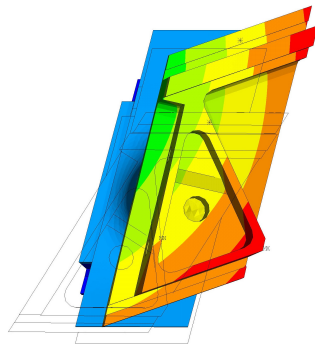
Figure 6.7: EW mode shape for configuration A1 at N62, ND=1.

the case as highlighted in figure xx in the aerodamping plot, apart from a small ripple at low IBPA. But most importantly is important to note that it is basically stable.

Moving on to analyze the Flap2 on blade 2, it is clear the effectiveness of the mistuning pattern 1-0 on the blade 2: the curve almost flattens and with a fairly margin over the zero line, effectively stabilizing the blade which otherwise had a great instability region, both in extension in terms of IBPA and in amplitude.

The same effects can be seen for the EW mode shape. In figure 6.6 the EW1 and EW2 modes for A1C2-A1 and in figure 6.7 the EW mode for A1.

As shown in the graph in figure 6.8, the frequencies are as always splitted, and the graph is analogous to what we have seen in figure 6.5 for mode shape Flap, even though in this case, the EW1 and EW2 modes are slightly more unstable than in Flap1 case: it has a bigger instability at low IBPA for EW1 mode and, regarding EW2, between IBPA -90° to -20° the aerodamping lowers, reaching a value slightly lower than zero compared to Flap2 mode, which caused a
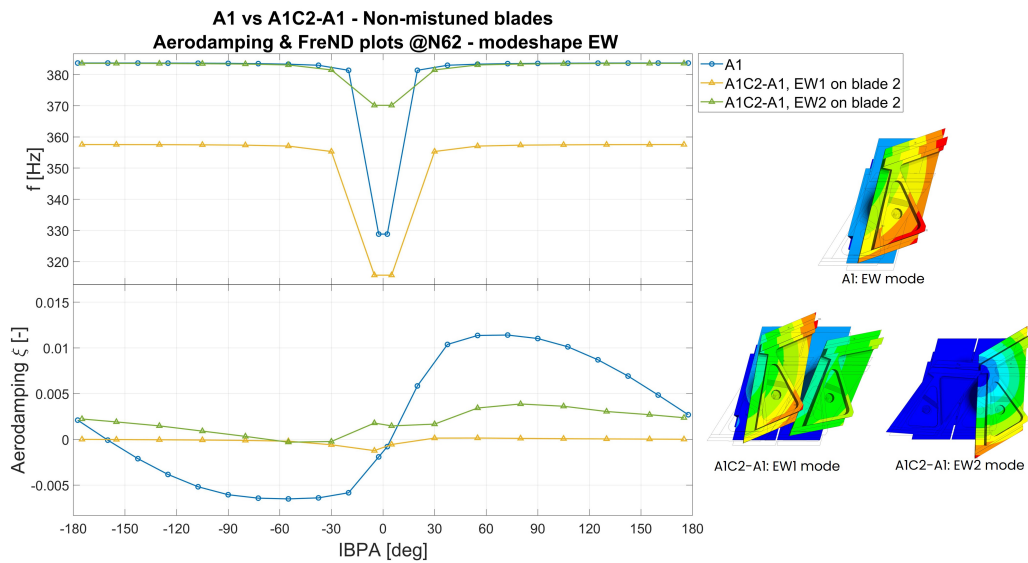
Figure 6.8: In the figure above, the comparison between the configuration A1 and A1C2-A1 for mode shape EW at N62. The modes EW1 and EW2 are applied to the blade 2.

basically flat and well stable aerodamping curve.

So, what we can see is that the EW mode shape is more unstable compared to Flap mode shape on A1C2-A1, hence the mistuning pattern 1-0 is less effective in stabilizing the blade and avoiding the energy to be fed into the structure from the flow around it in the case of EW mode shape at N62.

The same pattern to some extent, can be seen from figure 6.9 to 6.12 for the cases at N90 and N103, even though as explained before, the rotational speed has a stabilizing effect.

A1C2-A1 blade 1 vs A1C2 We now move to compare A1C2-A1 blade 1 with A1C2 at N62 in order to see the effects on the blade with mistuning mass.

Starting from Flap mode shape, we can see in figure 6.13 the analogous of the previous paragraph regarding the FreND plot, with the Flap1 mode this time having the same frequency as the A1C2 Flap mode.
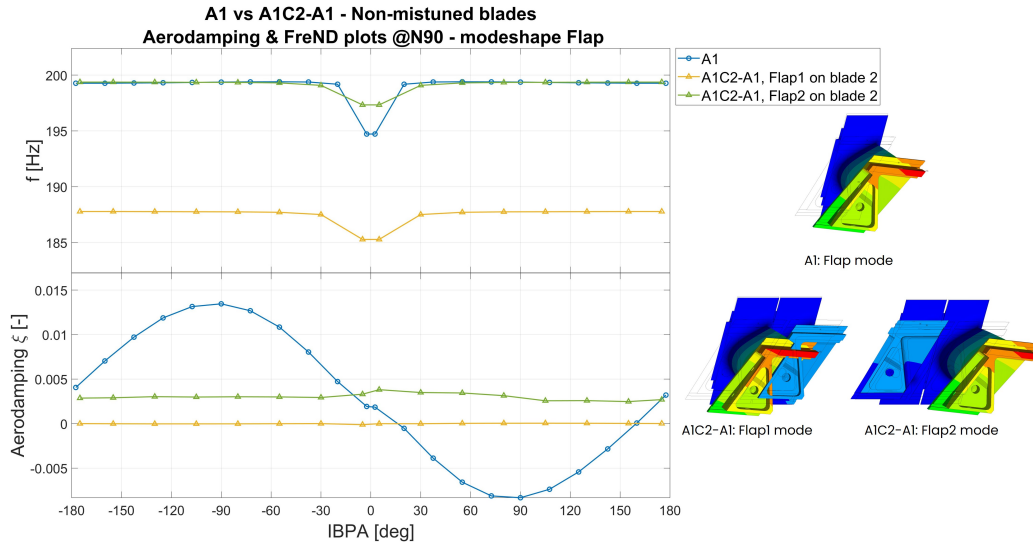
Figure 6.9: In the figure above, the comparison between the configuration A1 and A1C2-A1 for mode shape Flap at N90. The modes Flap1 and Flap2 are applied to the blade 2.
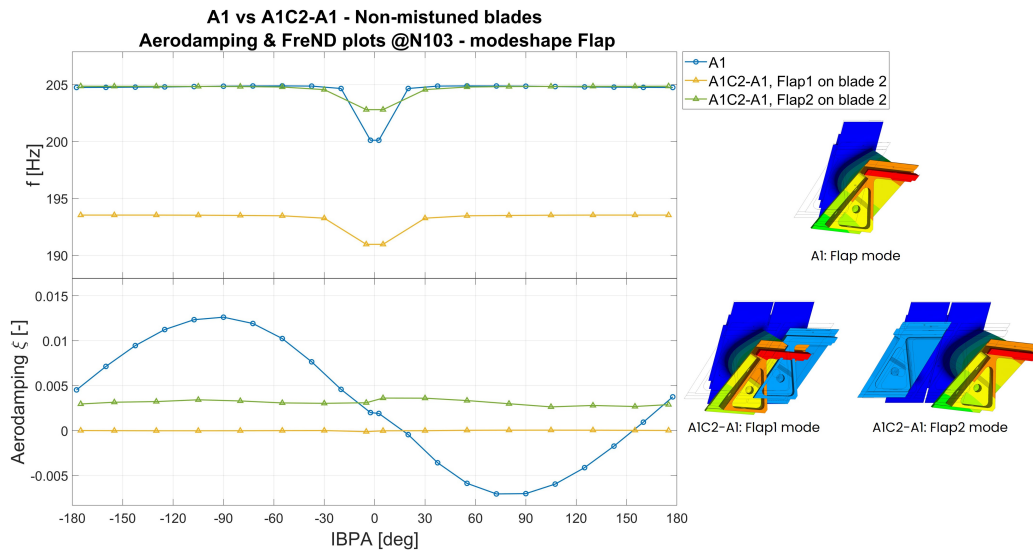
Figure 6.10: In the figure above, the comparison between the configuration A1 and A1C2-A1 for mode shape Flap at N103. The modes Flap1 and Flap2 are applied to the blade 2.
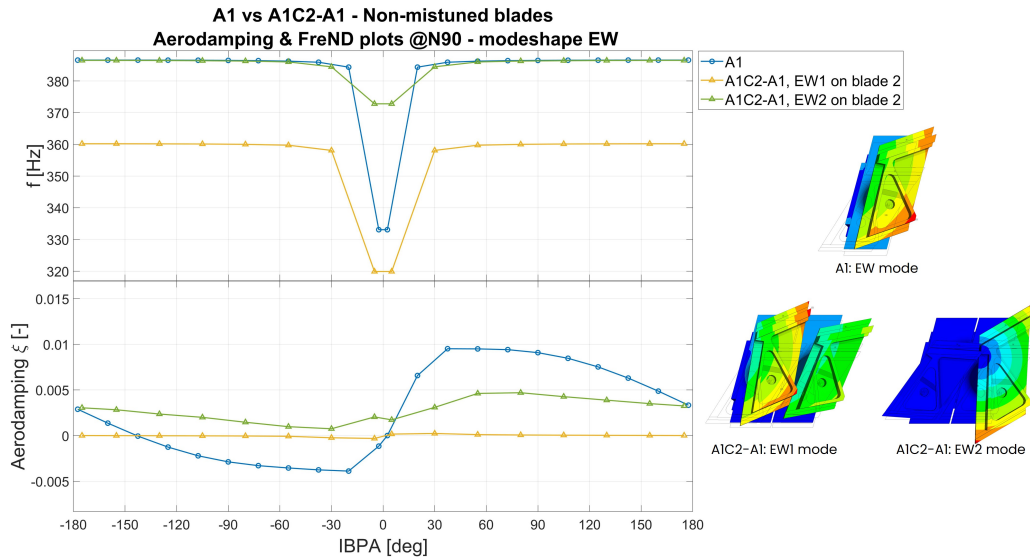
Figure 6.11: In the figure above, the comparison between the configuration A1 and A1C2-A1 for mode shape EW at N90. The modes EW1 and EW2 are applied to the blade 2.

Figure 6.12: In the figure above, the comparison between the configuration A1 and A1C2-A1 for mode shape EW at N103. The modes EW1 and EW2 are applied to the blade 2.
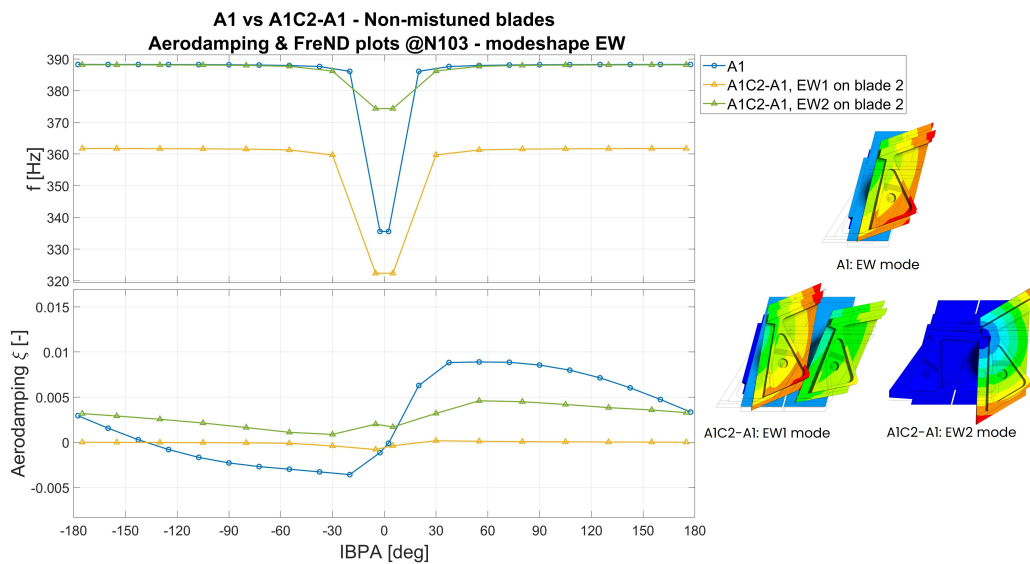
Figure 6.13: In the figure above, the comparison between the configuration A1C2 and A1C2-A1 for mode shape Flap at N62. The modes Flap1 and Flap2 are applied to the blade 1.
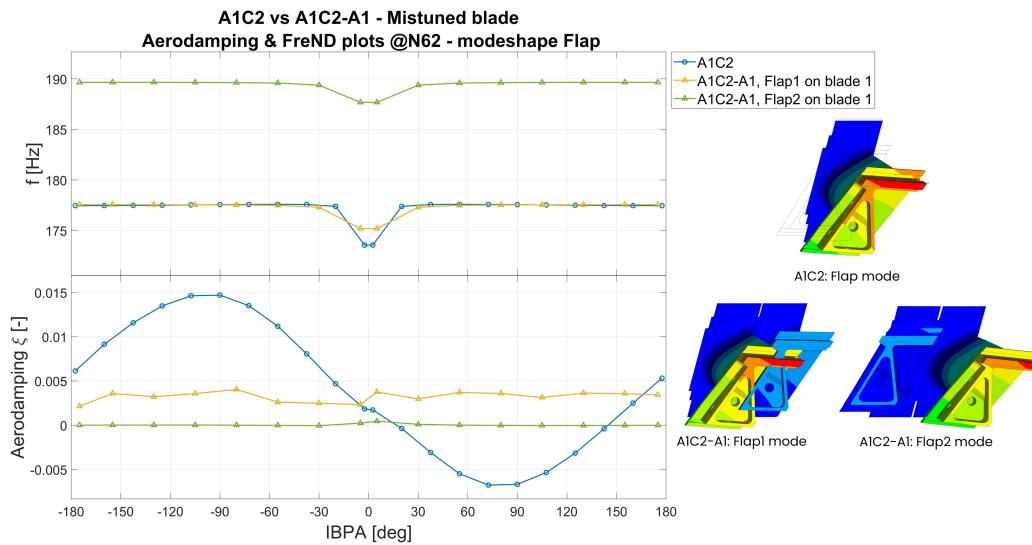
Moving on to the aerodamping, here the aerodmaping lines are switched, with the Flap1 on blade 1 being higher and the Flap 2 on blade 1 being almost always equal to zero and completely flat.

Regarding the Flap 1 on blade 1 the aerodamping curve is again completely in the stable region even though with a lower margin compared to the previous case but, at the same time, the Flap 2 on blade 1 curve has a ripple on the positive side of the graph, making the curve completely stable.

If we now evaluate the EW mode shape, we have slightly different situation, but still similar. As shown in figure 6.14, the EW mode shape is again more unstable compared to the Flap mode shape but still effective on stabilizing the blade. Moreover, in this case, the blade which moves less, with hence an almost flat and near zero value of aerodamping, the EW2 on blade 1, is in this case more stable than in the previous case, with the whole curve over zero, also at low IBPA where meanwhile, in the case of EW1 on blade 2, we had a slightly unstable region.

On the other side, the EW1 on blade 1 is more unstable than what happened in EW2 on blade 2.
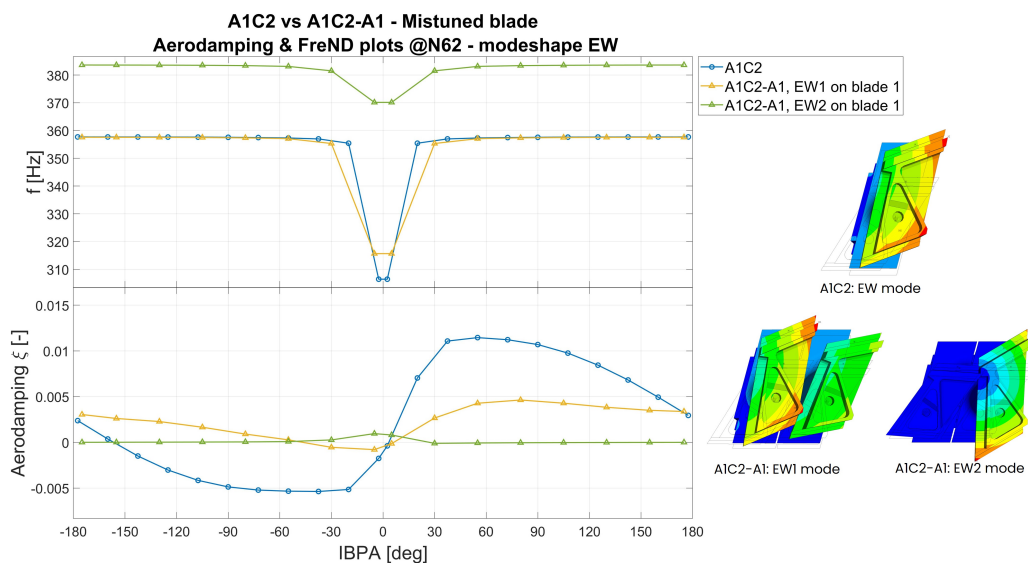
Figure 6.14: In the figure above, the comparison between the configuration A1C2 and A1C2-A1 for mode shape EW at N62. The modes EW1 and EW2 are applied to the blade 1.

Despite that, it is undoubted the beneficial overall effect of the mistuning pattern 1-0 both on EW and Flap mode shapes.

Same effect as before with rotational speed for both Flap and EW as shown from figure 6.15 to 6.18.

6.2.2 Mistuning pattern 1-0-0-0

As a final test, we tried to test whether or not introducing a different mistuning pattern would be more beneficial, compared to the mistuning patter 1-0, or actually worse. For this reason, we tested the mistuning patter 1-0-0-0 shown in figure 3.2.
So, the objective of this section will be to compare the A1C2-A1 configuration with A1C2-A1x3.

The mode shape tested are again EW and Flap and have been reported in figures 6.19 and 3.5 for N62 case at ND1.

So since the graphs can start to get confusing since the number of curves start to multiply especially for the case of A1C2-A1x3 (mistuning pattern 1-0-0-0): we would have, for a single mode shape,
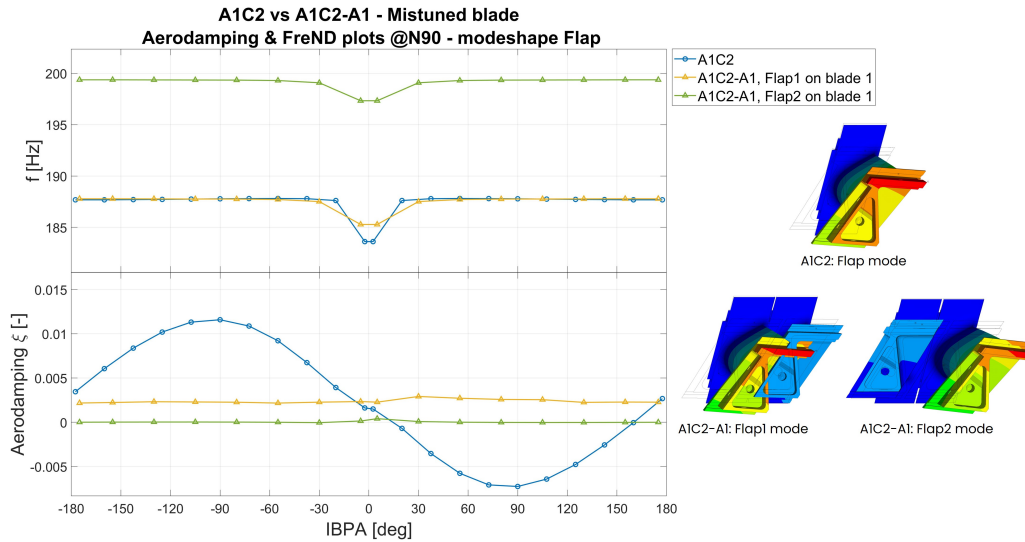
Figure 6.15: In the figure above, the comparison between the configuration A1C2 and A1C2-A1 for mode shape Flap at N90. The modes Flap1 and Flap2 are applied to the blade 1.
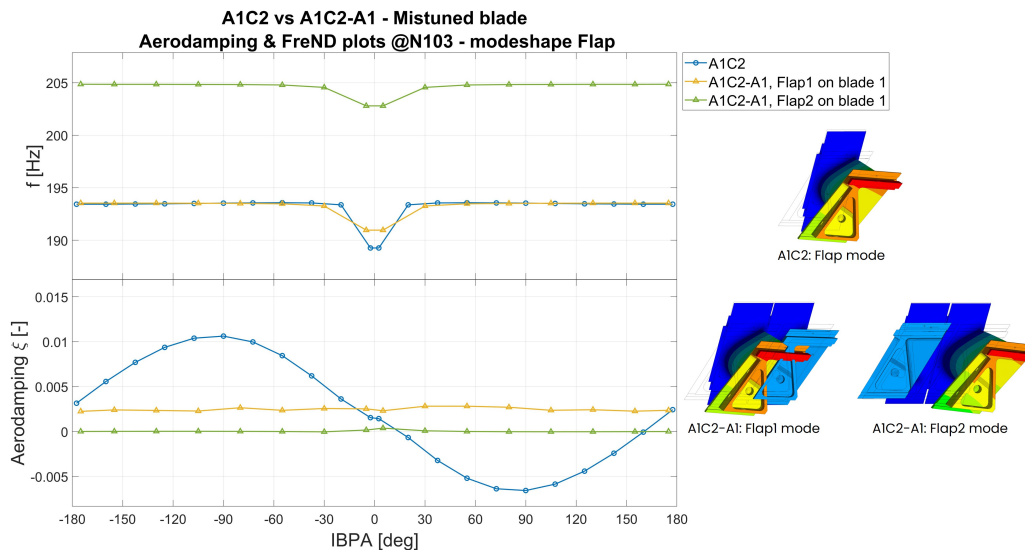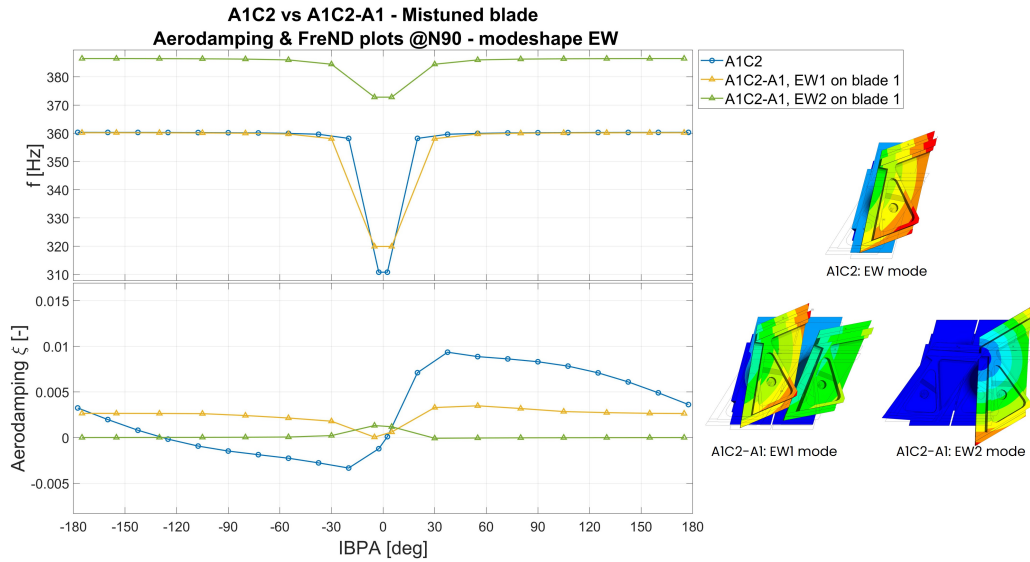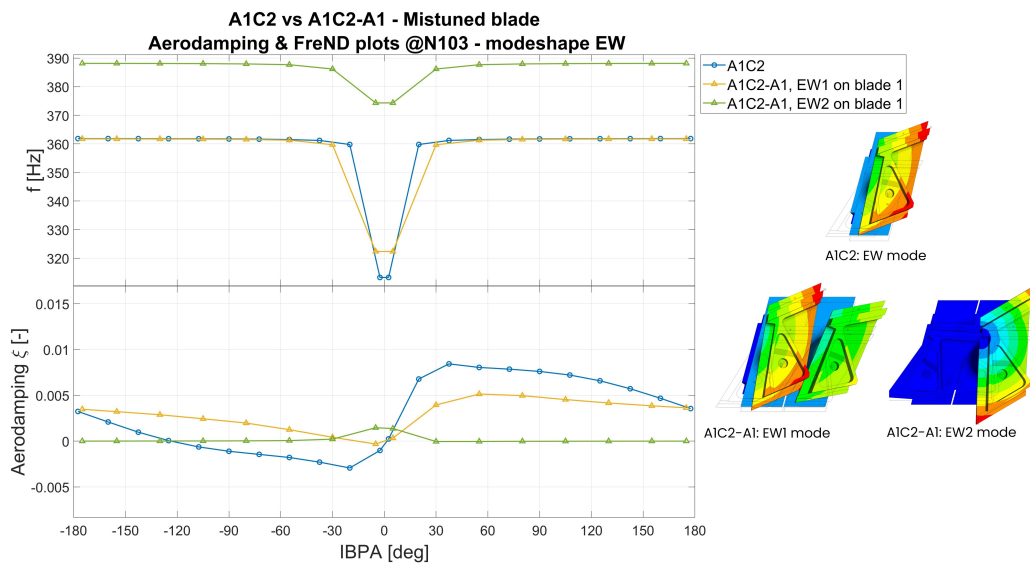

Figure 6.16: In the figure above, the comparison between the configuration A1C2 and A1C2-A1 for mode shape Flap at N103. The modes Flap1 and Flap2 are applied to the blade 1.

Figure 6.17: In the figure above, the comparison between the configuration A1C2 and A1C2-A1 for mode shape EW at N90. The modes EW1 and EW2 are applied to the blade 1.
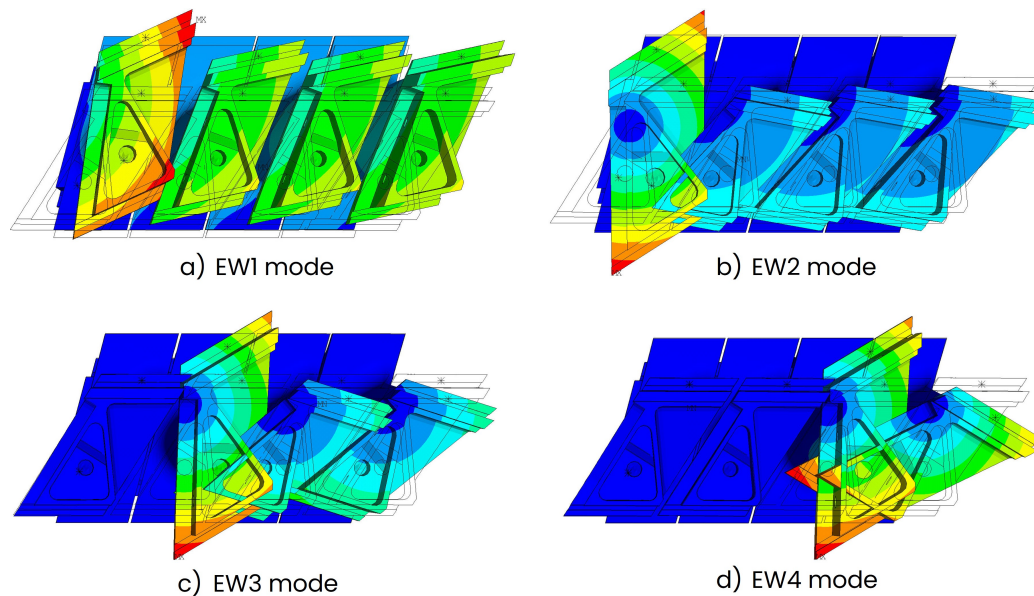

Figure 6.18: In the figure above, the comparison between the configuration A1C2 and A1C2-A1 for mode shape EW at N103. The modes EW1 and EW2 are applied to the blade 1.

a) EW1 mode   b) EW2 mode

c) EW3 mode   d) EW4 mode

Figure 6.19: EW modes for A1C2–A1x3 at N62, ND=1.

a total of 16 curves, 12 in the case we consider only the blades without the mistuning mass and 4 for the only mistuning mass.

This again is due to the fact that for every mode we calculate the aerodamping for every blade.
For this reason, in the graphs in this section we will evaluate only the curves where the displacement is high enough to give a significant information in the aerodamping graphs, hence the curve is not flat and near zero.

A1C2–A1 blade 2 vs A1C2–A1x3 blade 2 to 4   As before, we start the comparison with the blades without mistuning mass between A1C2–A1 and A1C2–A1x3 at N62, so the baled 2 for A1C2–A1 and the blades from 2 to 4 for A1C2–A1x3 and mode shape Flap.

It is apparent, from the aerodamping plot in figure 6.20, that also the configuration A1C2–A1x3 seems effective in stabilizing the blades as demonstrated by the curves of modes:

- Flap2 mode on blade 2;
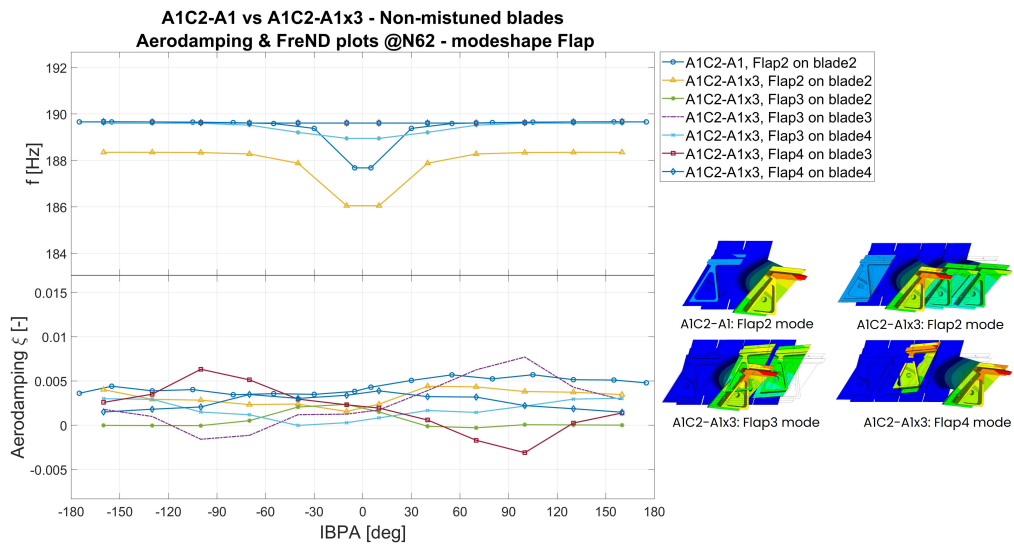
Figure 6.20: In figure, the comparison for mode shape Flap between configurations A1C2-A1 and A1C2-A1x3 for N62 and for blades without mistuning mass with a relative aerodamping result.

- Flap3 mode on blade 2;

- Flap3 mode on blade 4;

- Flap4 mode on blade 4;

But on the other side, it is evident how it fails to properly stabilize the blade number three in the case of Flap3 and Flap4 modes (the other blades are all stable).
In fact, the aerodamping values go deep below the negative values, making clear that the blade would be unstable.

Moreover, the situation does not get better with increasing rotational speed as shown in figure 6.21 and 6.22 for N90 and N103: the velocity itself does not help to stabilize the blade enough and the instability keeps being deep and with a decent extension as before in both cases.

This situation can be explained by the fact the blade is the one more distant from the mistuned blade which would have help stabilize the blade. The stabilization in fact happens in the cases of blade 4 and 2 but does not occur for blade 3 as well depicted by the figure 6.20.
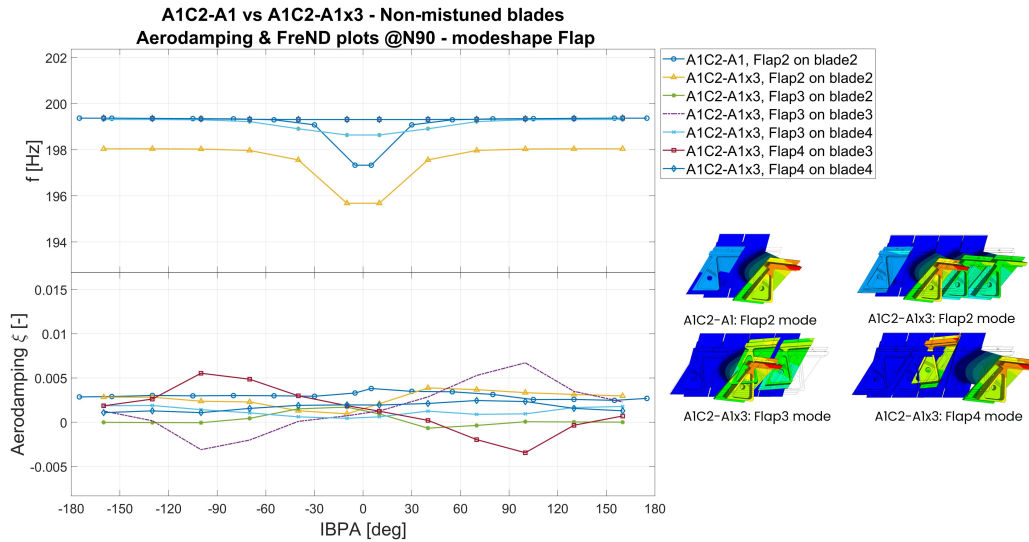
Figure 6.21: In figure, the comparison for mode shape Flap between configurations A1C2-A1 and A1C2-A1x3 for N90 and for blades without mistuning mass with a relative aerodamping result.
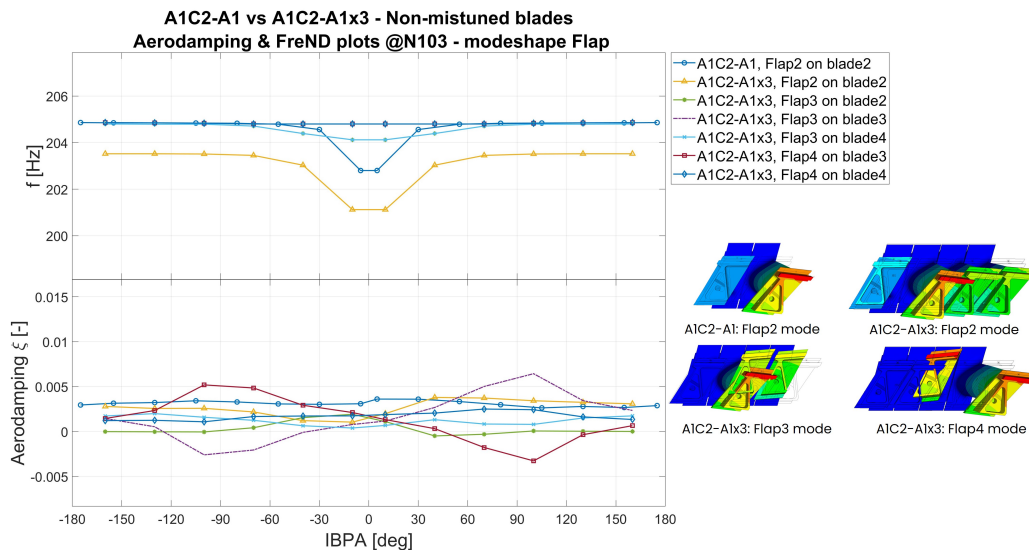
Figure 6.22: In figure, the comparison for mode shape Flap between configurations A1C2-A1 and A1C2-A1x3 for N103 and for blades without mistuning mass with a relative aerodamping result.
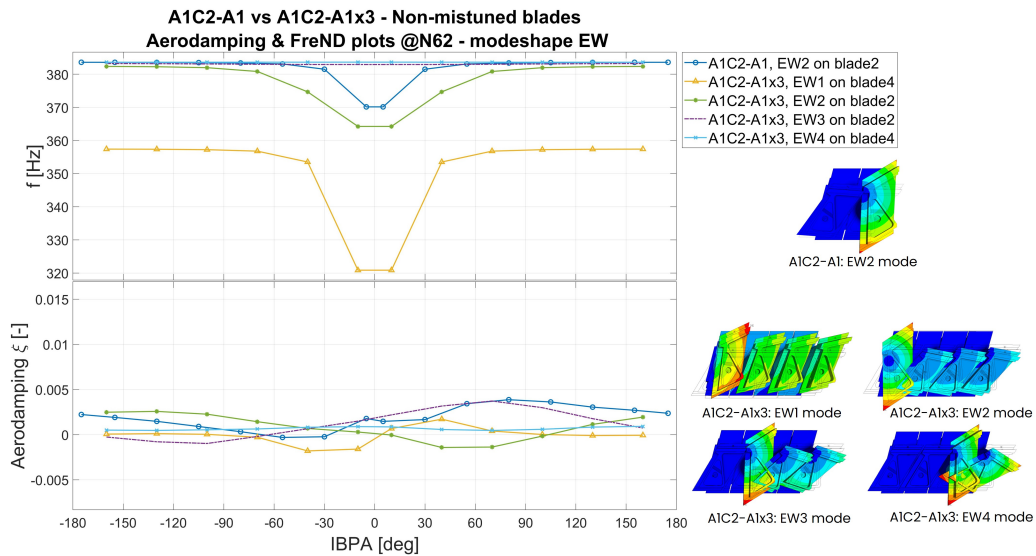
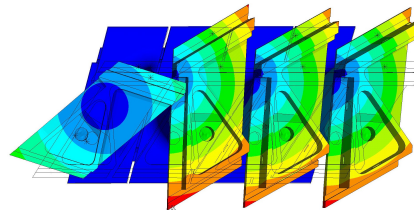**Figure 6.23:** In figure, the comparison for mode shape EW between configurations A1C2-A1 and A1C2-A1x3 for N62 and for blades without mistuning mass with a relative aerodamping result.


Figure 6.24: EW2 mode for configuration A1C2-A1x3 at N62 and ND=4.

Moving to the EW modeshape (figure 6.23), we have a sight destabilizing effect on blade 4 from -70° to 0° IBPA with EW1 mode.

A particular effect is seen in the case of EW2 mode on blade 1: in this case, the mode has for IBPA -10° to 10° a major movement still for blade 1 but, as we move to higher IBPA (or higher ND), we see that the blade which moves more is the blade 2, as one would expect and as shown in figure 6.24. The suspect in this case is a mode intersection, with the mode here named EW2 at ND=1 (or IBPA=10°) to be more like a second EW mode shape for the blade 1 (so a 2EW mode shape).
Nevertheless, the blade 1 also in this case is stable but, the same can't be said for blade 2 which between IBPA 10° to 100° has an unstable zone.
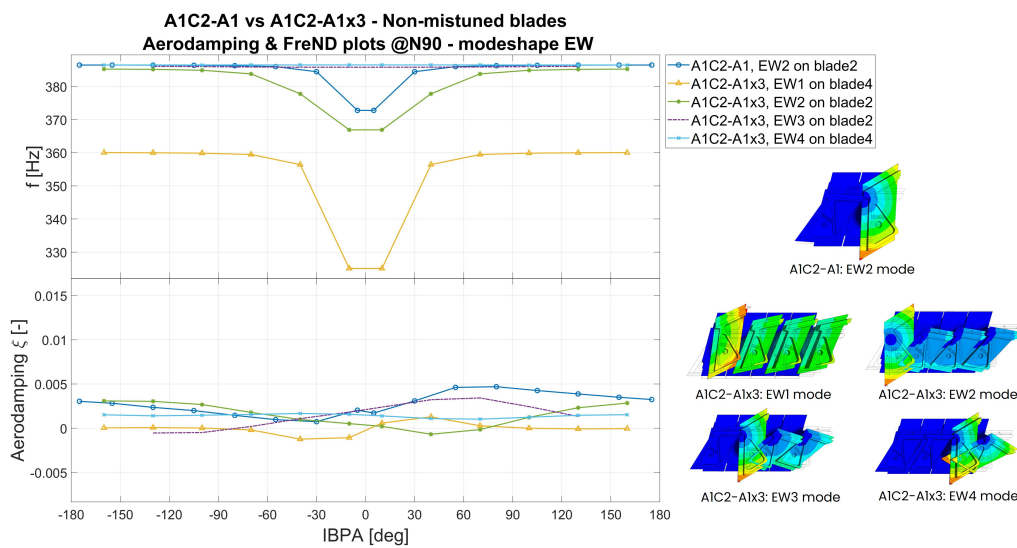
Figure 6.25: In figure, the comparison for mode shape EW between configurations A1C2-A1 and A1C2-A1x3 for N90 and for blades without mistuning mass with a relative aerodamping result.

The other important instability can be found with EW3 mode on blade 2, with a little instability, almost marginal, between -160° to -70°.

In figure 6.25 and 6.26 the graphs for N90 and N103.

All in all, the EW mode is rather stable compared to the Flap mode but in any case it is definitely more unstable compared to A1C2-A1.

A1C2-A1 blade 1 vs A1C2-A1x3 blade 1   We now move to the final comparison, between the blade 1 of A1C2-A1 and A1C2-A1x3, which we remember are the mistuning pattern 1-0 and 1-0-0-0 respectively.

Starting from Flap mode shape as always, we consider only the Flap1 on blade 1 for both the configurations since the only blade moving in both cases, as shown in figure 3.5 and 3.4, is the blade 1 and, in addition to that, the aerodamping plots for the other blades are not really representative since are almost flat and around zero, so we are going to consider them as stable (as it really is).
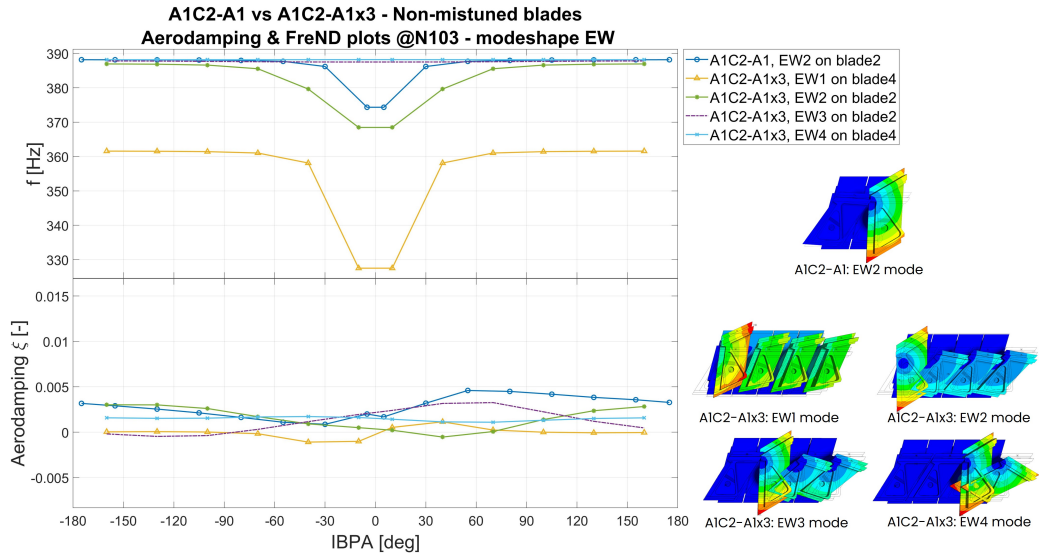
Figure 6.26: In figure, the comparison for mode shape EW between configurations A1C2-A1 and A1C2-A1x3 for N103 and for blades without mistuning mass with a relative aerodamping result.
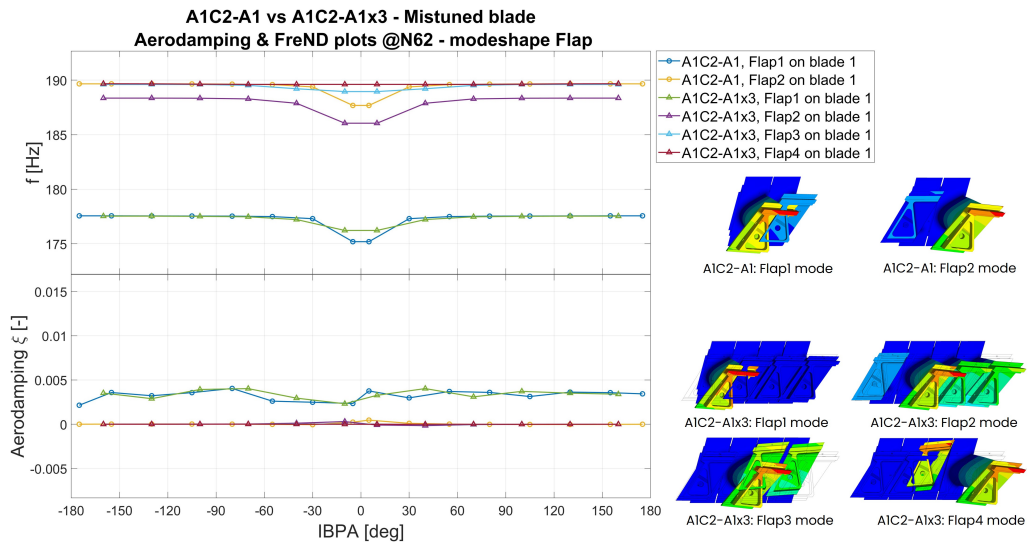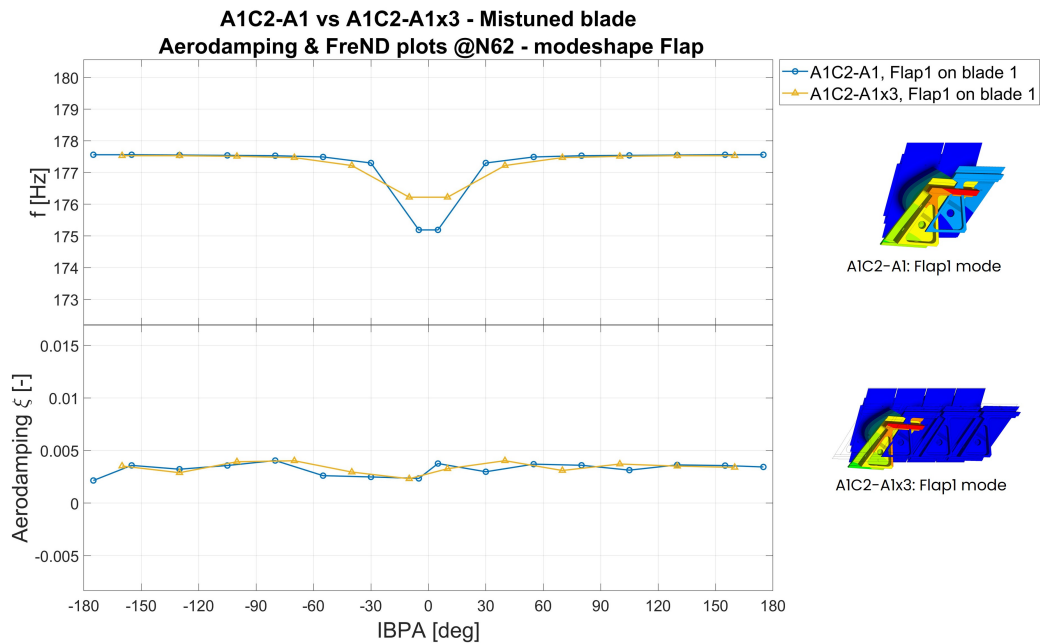

Figure 6.27: Comparison of the Flap1 and Flap2 mode on blade 1 for configurations A1C2-A1x3 and A1C2-A1 at N62.

Figure 6.28: Comparison of the Flap1 on blade 1 for configurations A1C2-A1x3 and A1C2-A1 at N62.

The complete graph is shown in figure 6.27.

Concentrating our attention to only Flap 1 on balde 1, in figure 6.28, we can see that in both cases the mistuing mass is effective in stabilizing the blade and this effect is present not only at N62 but also at N90 and N103 as shown in figure 6.29 and 6.30 respectively, despite having less margin in the N103 case for the A1C2-A1x3 configuration.

Meanwhile, at N62 with EW mode shape, the situation is actually the opposite, with the configuration A1C2 being more unstable, even though by a small amount as shown in figure 6.31.

The situation rapidly get back to normal with increasing rotational speeds, which show a stable curve for both the configurations even though, in both cases we are at the limit of stability, as shown in figure 6.32 and 6.33 for N90 and N103.

Also in this case, the other blades are stable in both cases as highlighted by figure 6.34, where all the combinations are shown for EW1 mode with both configurations at N62 as a reference.
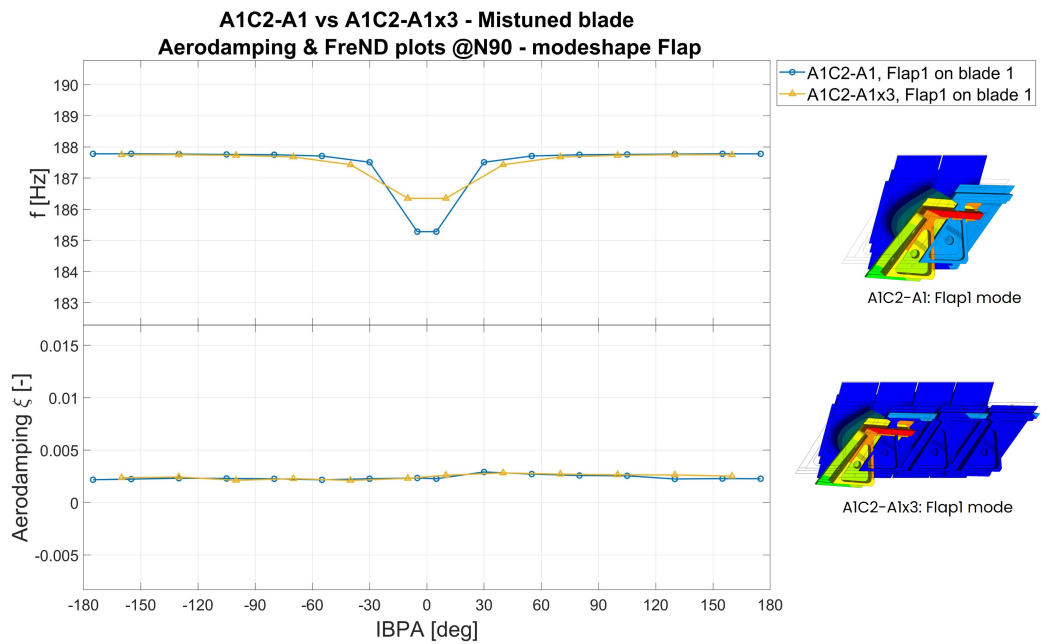
Figure 6.29: Comparison of the Flap1 on blade 1 for configurations A1C2-A1x3 and A1C2-A1 at N90.
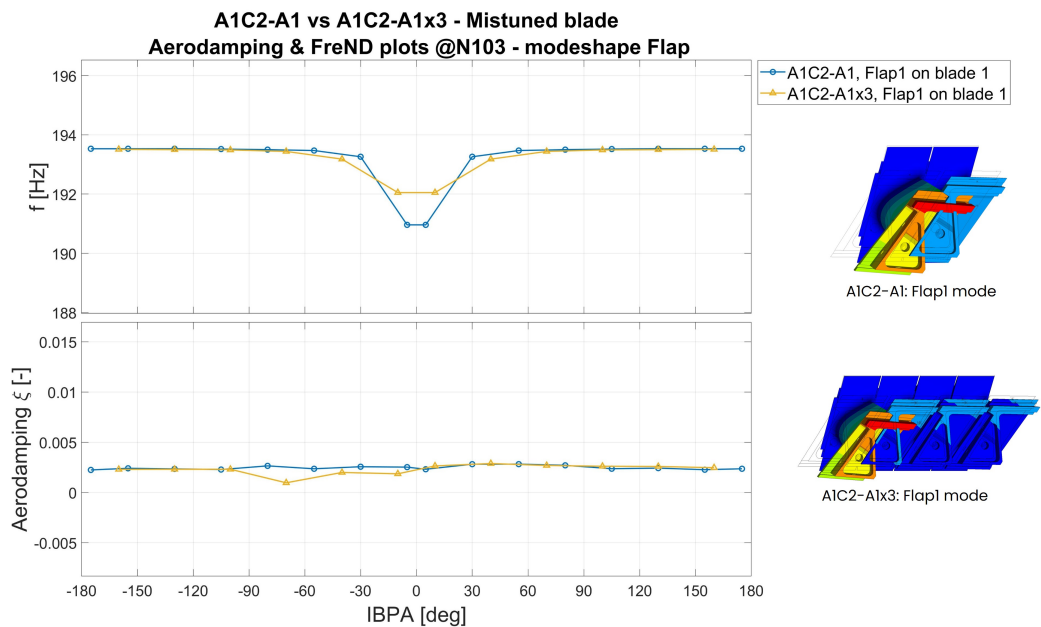
Figure 6.30: Comparison of the Flap1 on blade 1 for configurations A1C2-A1x3 and A1C2-A1 at N103.
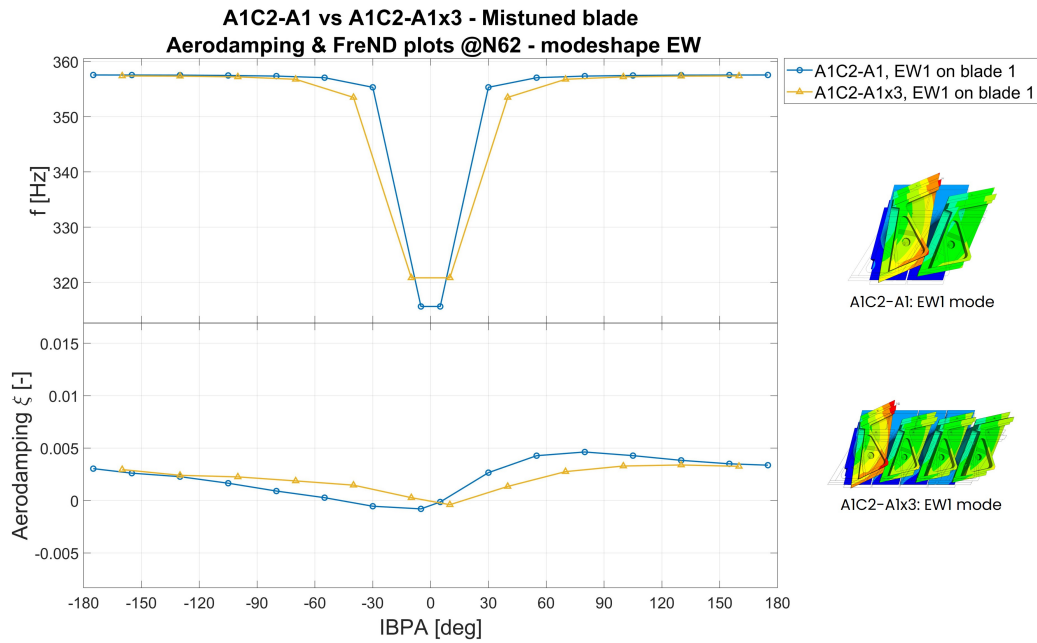
Figure 6.31: Comparison of the EW1 on blade 1 for configurations A1C2-A1x3 and A1C2-A1 at N62.

Figure 6.32: Comparison of the EW1 on blade 1 for configurations A1C2-A1x3 and A1C2-A1 at N90.

Figure 6.33: Comparison of the EW1 on blade 1 for configurations A1C2-A1x3 and A1C2-A1 at N103.

Figure 6.34: Comparison of the EW1 and EW2 mode on blade 1 for configurations A1C2-A1x3 and A1C2-A1 at N62.

In this case, apart from one scenario, both configurations are equally valid for stabilizing the blades.
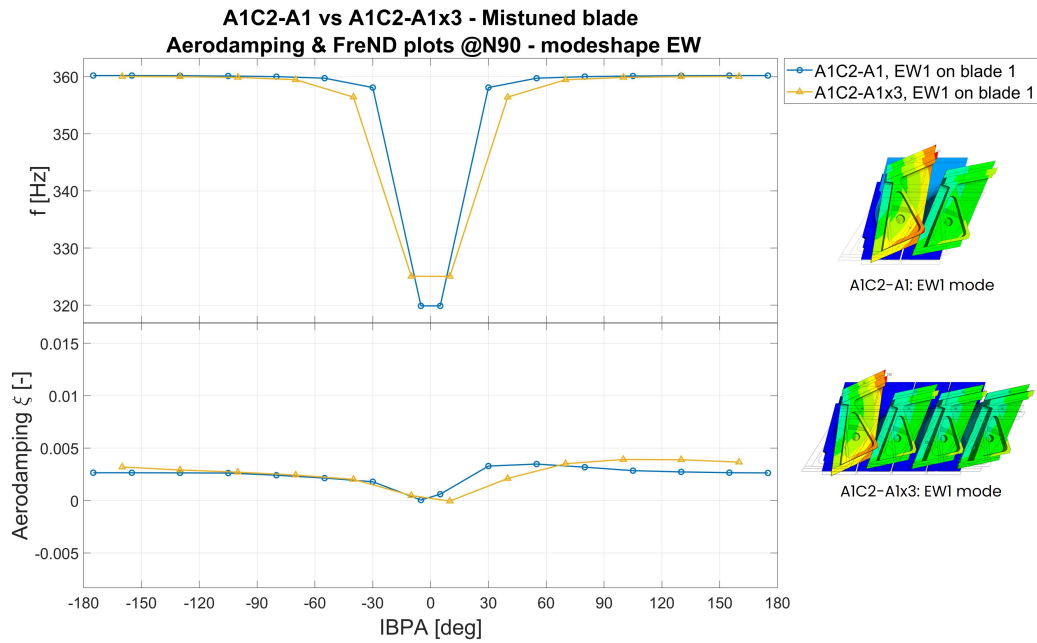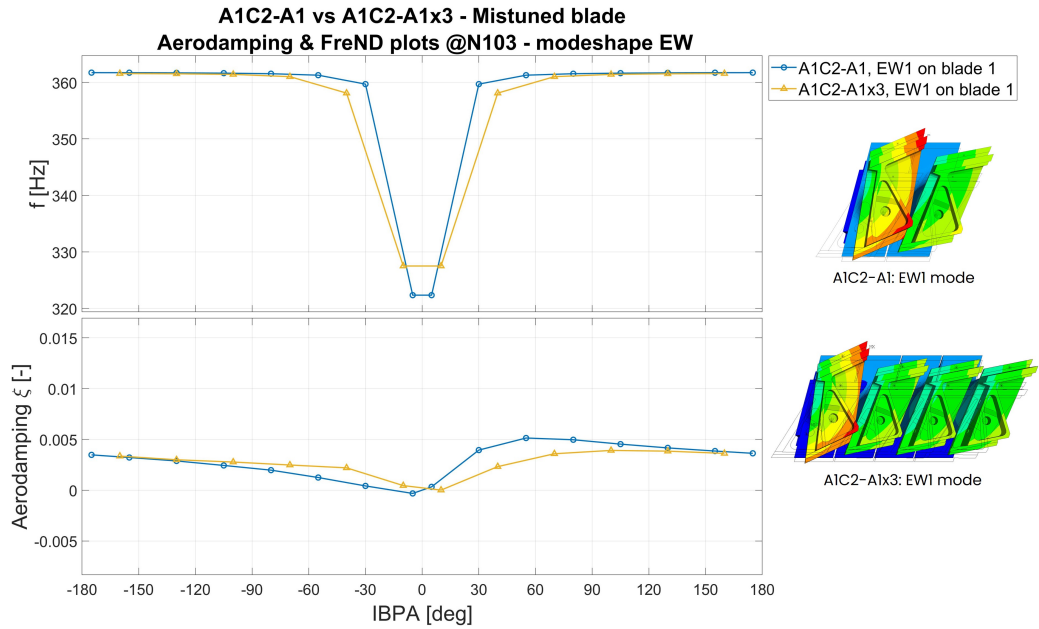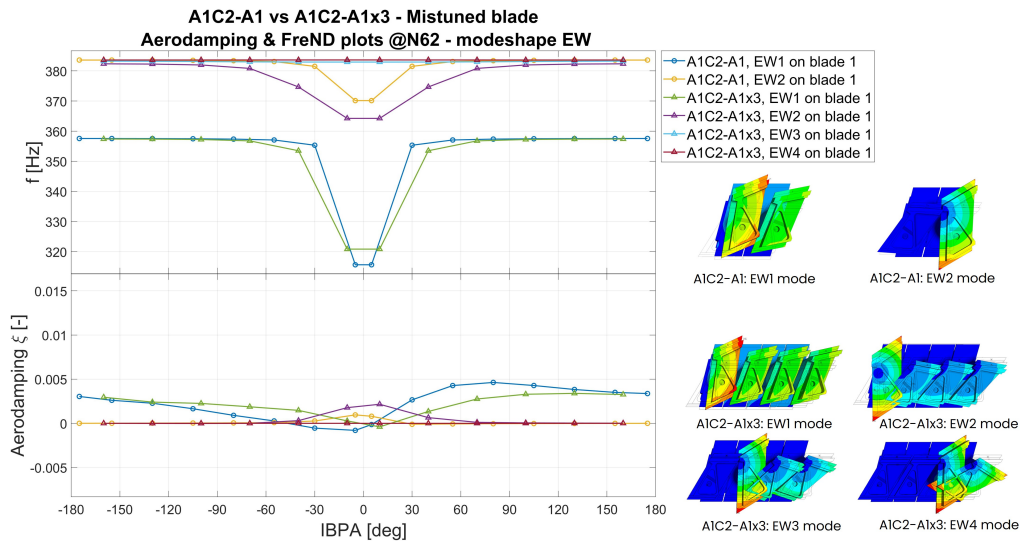
Chapter 7

Conclusions

We conclude this thesis work with some considerations regarding the results obtained by the tests carried.

Solver effect   From the analyses carried it is clear how the TRAF solver is definitely the most accurate solver compared to LARS solver, since it is able to highlight some critical behaviors which otherwise would not have been detected by the LARS solver.

in fact, there is a remarkable difference especially in the cases where acoustic resonance occurs but, it is also true, that the LARS solver still gives an idea of the blade behavior in almost every condition.

Moreover, it has to be considered the main drawback given by the TRAF solver which is represented by the much higher computational cost, with an astonishing 128% increase in computational time.
This increase in time is not to be underestimated since in the case of multiple test cases can become quite invasive and cause several problems.
In the end, the usage of the TRAF solver should be limited for small simulations numbers, where the LARS results seem to show a marginal stability or a resonance peak.

Rotational speed effect   The rotational speeds tested have shown that the effect actually depends on the mode shape.

In this test case, the rotational speed has shown that, for a Flap mode shape the blade becomes more stable with increasing rotational speed but on the other side, with an EW mode shape, the rotational speed could actually make the vibrations worse, also depending on the configuration used.

Mistuning effect   Regarding the usage of a mistuning mass on every blade, as could be expected, has almost no effect on the blade stability due to the fact that the blades configuration did not change and kept being a tuned configuration.

All in all, we can state that the tuned configuration with an additional mass is not the correct way to be pursued in order to achieve flutter stability.

Mistuning patter effect   Regarding the mistuning pattern, undoubtedly the mistuning pattern 1-0 effectively stabilized the blades compared to the case A1C2.
Despite that, some marginal instability has been found in some cases. To take into account some possible errors, would be beneficial to try using a heavier mistuning mass in order to increase the difference in natural frequencies.

On the other side, also the configuration A1C2-A1x3, with a mistuning patter 1-0-0-0 has shown good results but, in several occasions has failed to completely stabilize the blades and by some margin, meaning that it would not have been enough to stabilize them.

This difference is evident when compared to the effects of the mistuning pattern 1-0.

Ultimately, we can say that the mistuning pattern 1-0 is by far the most effective in achieving the flutter stability and that a tuned configuration poses, in the conditions tested, high concerns re-

garding flutter for low pressure turbines.

Obviously, some solutions already exist, such as the interlocking, but that solution increases the weight and goes against one of the industry objective, which is to reduce engine weight.

Bibliography

[1] Experimental research into aeroelastic phenomena in turbine rotor blades inside arias eu project. In *Proceedings of ISUAAAT16 Conference, paper ISUAAAT16- 30*, 2022.

[2] K. Aainsqatsi. Turbofan engine. `https://commons.wikimedia.org/wiki/File:Turbofan_operation.svg`, 2008.

[3] Ronnie Bladh. Efficient predictions of the vibratory response of mistuned bladed disks by reduced order modeling. 06 2023.

[4] Jiri Blazek. Chapter 11 - principles of grid generation. In Jiri Blazek, editor, *Computational Fluid Dynamics: Principles and Applications (Third Edition)*, pages 357–393. Butterworth-Heinemann, Oxford, third edition edition, 2015.

[5] Jeff Dahl. Jet engine. `https://en.wikipedia.org/wiki/Components_of_jet_engines#/media/File:Jet_engine_numbered.svg`, 2008.

[6] JetX Engineering. Turbine blade roots. `https://www.jet-x.org/a5.html`.

[7] Marco Gambini and Michela Vellini. *Preliminary Design of Axial Flow Turbines*, pages 109–153. Springer International Publishing, Cham, 2021.

[8] Matteo Giovannini, Filippo Rubechini, Michele Marconcini, Andrea Arnone, and Francesco Bertini. Reducing secondary flow losses in low-pressure turbines: The "snaked" blade. *International Journal of Turbomachinery, Propulsion and Power*, 4(3), 2019.

[9] J. Golley. *Jet: Frank Whittle and the Invention of the Jet Engine*. Datum Publishing Limited, 2009.

95

[10] P.G. Hill and C.R. Peterson. *Mechanics and Thermodynamics of Propulsion*. Addison-Wesley, 1992.

[11] Dario Pastrone. Lecture notes of "motori per aeromobili", 2022.

[12] L Pinelli, F Poli, A Arnone, and C Schipani. A time-accurate 3d method for turbomachinery blade flutter analysis. In *12th International Symposium on Unsteady Aerodynamics, Aeroacoustics and Aeroelasticity of Turbomachines (ISUAAAT). September*, pages 1–4, 2009.

[13] Lorenzo Pinelli. Lecture slides of "Aeromechanics", 2020.

[14] Rolls-Royce plc. *The Jet Engine*. Wiley, 2015.

[15] F Poli, E Gambini, A Arnone, and C Schipani. A 3d time-linearized method for turbomachinery blade flutter analysis. In *11th International Symposium on Unsteady Aerodynamics, Aeroacoustics and Aeroelasticity of Turbomachines*, 2006.

[16] ARiAS project partners. Arias project website. `https://www.arias-project.eu/news`, 2021.

[17] ARiAS project partners. Arias e-learnign repositories. `https://time.learnify.se/l/show.html#att/p0RX?startId=rwEB&lang=en`, 2023.

[18] Stefano Raimondo. Comparison between different 3d flutter solvers. Master's thesis, Politecnico di Torino, 2023.

[19] Prof. Z. S. Spakovszky. Thermodynamics and Propulsion. 11.5 Trends in thermal and propulsive efficiency, 2002.

[20] Unknown. Turboprop engine. `https://commons.wikimedia.org/wiki/File:Turboprop_operation-en.svg`, 2009.

[21] B. Daniele Zucca S. Lecture slides of "Dinamica dei rotori per applicazioni aerospaziali", 2021.